

VOLTAMMETRIC BEHAVIOR AND CAPACITANCE OF NANOSTRUCTURED CARBON
ELECTRODES IN ROOM TEMPERATURE IONIC LIQUIDS

By

Kirti Bhardwaj

A DISSERTATION

Submitted to
Michigan State University
in partial fulfillment of the requirements
for the degree of

Chemical Engineering – Doctor of Philosophy

2019

ABSTRACT

VOLTAMMETRIC BEHAVIOR AND CAPACITANCE OF NANOSTRUCTURED CARBON ELECTRODES IN ROOM TEMPERATURE IONIC LIQUIDS

By

Kirti Bhardwaj

Carbon is a unique element. Its uniqueness stems from its ability to bond with itself and form stable allotropes with incredibly diverse physical, chemical, electrical, and electrochemical properties. These allotropes include single- and poly-crystalline diamond (sp^3), diamond-like carbon (hybrid sp^2/sp^3) and graphitic carbon (sp^2). Of these, the diamond and diamond-like carbon electrodes are the least studied. Owing to their commercial availability, low cost, wide potential window, low background current, and chemical stability, these allotropes are used as electrode materials in electroanalysis, energy storage technologies, and electrochemical separations. For their optimal use, it is critical to understand and control the parameters that affect their electrochemical behavior. Over the last three decades, structure-property-function relationships for carbon electrodes have been established in traditional aqueous electrolytes. However, this knowledge is missing in the novel electrolytes called room temperature ionic liquids (RTILs).

RTILs are liquid salts solely made of charged cations and anions. They contain no solvent. They are finding ever-increasing use as electrolytes due to their excellent properties like wide thermal and electrochemical potential window, negligible vapor pressure, and good ionic conductivity. Since RTILs are highly charged media without any solvent, their organization at electrified interfaces (*i.e.*, charged electrodes) is different from the organization of aqueous and organic electrolyte solutions.

The research described in this dissertation focused on understanding the voltammetric properties and capacitance of nanostructured diamond and tetrahedral amorphous carbon thin film

electrodes in RTILs. Specific issues investigated included how the RTIL organization change with the applied potential, RTIL type, the carbon electrode type, and the electrode surface chemistry. The physical, chemical, and electronic properties of boron-doped diamond (BDD) and nitrogen-incorporated tetrahedral amorphous carbon (*ta*-C:N) thin-film electrodes are discussed, as are the properties of glassy carbon that was used for comparison studies.

Firstly, the effect of RTIL cation size and viscosity on the voltammetric behavior and capacitance of BDD was investigated. Next, the BDD surface was chemically modified to vary the type and coverage of surface groups (H- vs. O-termination). The surface wettability, as well as the voltammetric behavior and capacitance, were studied in two different RTILs and compared with the electrode behavior in an aqueous electrolyte solution. Finally, *ta*-C:N electrodes of varying nitrogen content were characterized to define their microstructure (sp^2/sp^3 content), and the voltammetric behavior and capacitance in the two RTILs were studied.

*To my parents, who taught me about love and life...
Thank you.*

*“It doesn’t stop being magic just because you know how it works.”
Sir Terry Pratchett*

ACKNOWLEDGEMENTS

First and foremost, I would like to thank my fiancé, Apoorv Shanker, for supporting me through this challenging process since its day 1 and reminding me to cherish the aesthetics of life. Your company made the difficult times (especially the third lap) bearable. Thanks for putting up with me on days when my sanity was hanging by a thread. Whether it was proofreading a document or waiting for me at some ridiculous hour at Michigan Flyer stops, you were always there for me. I am sure I would not have got through the graduate studies without you. Thank you for walking with me all the way here and loving me unconditionally. *Consider spending one more lifetime with me!*

As for the scientific journey, I would like to thank my advisor, Prof. Greg M. Swain for giving me the opportunity to work in his lab. The passion and enthusiasm you share for science have never failed to inspire me. Not only you were an incredible source of knowledge, you were always kind, supportive, and patient throughout my studies. You were never hesitant to tell me when things were not good enough, and although I did not always enjoy that part, the high standards you set made me a better researcher. Thank you for fostering a uniquely challenging graduate school experience. Thanks for motivating me on slow days and calming me down on the more emotional ones. Thank you for encouraging and inspiring me while showing humor, humility, and the best of humanity. I can only hope that I have picked up a very minuscule of your immense knowledge in the fields of diamond and electrochemistry. I hope your love for teaching, sharing knowledge, and asking questions will keep resonating with me. I am going to miss your jokes, 4 a.m. emails and the title ‘*Mrs. Doubtfire*’.

Gratitude is owed to my committee members, Profs. Scott C. Barton, James Galligan, Wen Li, and Erik M. Shapiro for agreeing to serve on my committee and providing feedback.

I want to thank Romana Jarošová and other Swain group members who were always there for a coffee and a chat. Sometimes it was science; sometimes it was the latest gossip...either way, it was always helpful.

Words cannot express my sincerest gratitude for my undergraduate advisor, Prof. Satishchandra B. Ogale, with whom my first experience with research started. Thank you for providing me the life-changing opportunity and ‘coercing’ me to apply to graduate school. If I am fortunate, your style and leadership will continue to influence my approach to science and outside it.

Thank you, Prof. Scott C. Barton, for your constructive feedback and all the challenges that you gave me. While you tested me on every turn, I am sure I would appreciate the learnings in the long term. I am thankful to you and the Department of Chemical Engineering and Materials Science for handling my funding situation many times throughout the course. Thank you for teaching me the modeling of electrochemical systems. Thank you, Prof. Robert Y. Ofoli, for choosing to be your teaching assistant. I learned a great deal from you.

I had the privilege of learning from the research community throughout my Ph.D. Thank you, Dr. Anthony J. Lucio, for being a supportive peer and sharing your research experiences with me. Thank you, Dr. Marcel Drüschler, for teaching me Cole-Cole analyses. I am incredibly appreciative of your time, advice, and knowledge. A massive thanks to Prof. S. Ramanathan, for enrolling me in your online course and teaching me the intricacies of impedance spectroscopy regarding data acquisition and interpretation. I would have never known the capabilities,

complexities, and versatility of the technique without your help. Indeed, it was one of the most challenging (and, fruitful) courses I took during my graduate studies.

To my suitemate, Eureka Pai, thank you for spoiling my taste buds with delicious food. The world does not have to know how good vegan food can taste! Thank you Dakshaini Ravinder, Preetam Giri, Sayli Bote, Eric Starley for your friendship. Suffice to say that you made my graduate experience so rich. Thank you for all the fun times, for enriching my life with new experiences and ideas, and for your refreshing company outside the confines of my laboratory. You all mean very much to me.

I extend a special thank you to Prof. Alexander Zevalkink for her amazing encouragement and belief in me. I remember how I had showed up uninvited at your lab when Rigaku Smartlabs (aka the 9 kV beast) was being unpacked. You were kind to let me play with the instrument and calmly listening to my ideas of optimizing the parameters before telling how ridiculous they were! I'll fondly remember our conversations and chit-chat.

Most of all, I am thankful to my friends and family for their unconditional love and support. I am truly blessed to have you in my life. Thank you, Aritra Chakraborty, for your friendship and for showing me the use of the Python algorithm to fit the impedance data. Thanks, Mom and Dad, for being my biggest fans. My brother, Aasheesh Bhardwaj, thanks for your sage advice and cool collectedness (and for saving my life in the Himalayas). My sister, Preeti, thanks for always bringing sunshine with your bubbly nature. It is always a good reminder to finish when your younger sister gets a real job before you do! To my Mom and Dad, thank you for every sacrifice- you are the strongest, most determined people I know, and I can confidently say that I am the person I am today because of you. Thank you for believing in me, pushing me to follow my heart

and dreams despite the unfamiliarity. You are truly inspirational, and I am so fortunate to have you as my parents.

TABLE OF CONTENTS

| | |
|--|-----------|
| LIST OF TABLES..... | xii |
| LIST OF FIGURES..... | xiii |
| Chapter 1 Introduction..... | 1 |
| 1.1 Carbon Electrodes | 1 |
| 1.1.1 Glassy Carbon (GC)..... | 2 |
| 1.1.1.1 GC as an Electrode..... | 3 |
| 1.1.2 Boron-doped Diamond (BDD)..... | 4 |
| 1.1.2.1 BDD as an Electrode..... | 6 |
| 1.1.3 Nitrogen-incorporated tetrahedral amorphous carbon (<i>ta</i> -C:N)..... | 10 |
| 1.2 Room Temperature Ionic Liquids (RTILs)..... | 11 |
| 1.3 Electrical Double Layer Models..... | 12 |
| 1.3.1 EDL in Room Temperature Ionic Liquids..... | 16 |
| 1.4 Dissertation Goals..... | 20 |
| REFERENCES..... | 23 |
| Chapter 2 Experimental and Methods..... | 31 |
| 2.1 Materials..... | 31 |
| 2.1.1 Room Temperature Ionic Liquids (RTILs)..... | 31 |
| 2.1.2 Aqueous Electrolytes..... | 32 |
| 2.2 Electrode Preparation..... | 33 |
| 2.2.1 Glassy Carbon Electrodes..... | 33 |
| 2.2.2 Boron-Doped Nanocrystalline Diamond (BDD) Thin Film Electrodes..... | 33 |
| 2.2.3 Nitrogen-Incorporated Tetrahedral Amorphous Carbon (<i>ta</i> -C:N) Thin Film Electrodes..... | 34 |
| 2.2.4 Polycrystalline Gold Thin Film Electrodes..... | 35 |
| 2.2.5 Surface Modification of BDD Electrodes..... | 36 |
| 2.3 Instrumentation..... | 37 |
| 2.3.1 Visible Raman Spectroscopy..... | 37 |
| 2.3.2 X-ray Diffraction (XRD) Spectroscopy..... | 37 |
| 2.3.3 X-ray Photoelectron Spectroscopy (XPS) | 37 |
| 2.3.4 Scanning Electron Microscopy (SEM)..... | 38 |
| 2.3.5 Contact Angle Measurements..... | 38 |
| 2.3.6 Thermogravimetric Analysis (TGA)..... | 39 |
| 2.3.7 Fourier Transform Infrared (FTIR) Spectroscopy..... | 39 |
| 2.3.8 High-Resolution Transmission Electron Microscopy (HR-TEM)..... | 40 |
| 2.3.9 Electron Energy Loss Spectroscopy (EELS)..... | 40 |
| 2.4 Electrochemical Techniques..... | 41 |
| 2.4.1 Cyclic Voltammetry..... | 42 |
| 2.4.2 Electrochemical Impedance Spectroscopy..... | 43 |
| 2.4.3 Single Frequency Impedance Measurements..... | 44 |
| REFERENCES..... | 46 |

Chapter 3 Potential-Dependent Capacitance of Boron-Doped Nanocrystalline Diamond Planar Electrodes in RTILs – Effect of Measurement Method and RTIL Type.....49

| | |
|--|----|
| 3.1 Introduction..... | 49 |
| 3.2 Materials and Methods..... | 52 |
| 3.2.1 Boron-Doped Diamond Electrodes..... | 52 |
| 3.2.2 Gold Electrodes..... | 53 |
| 3.2.3 Chemicals..... | 54 |
| 3.2.4 Electrochemical Measurements..... | 55 |
| 3.2.5 Characterization of the BDD Electrodes and Purified RTILs..... | 58 |
| 3.2.6 Statistical Data Analysis..... | 58 |
| 3.3 Results..... | 59 |
| 3.3.1 Physicochemical Characterization of the RTILs..... | 59 |
| 3.3.2 Electrochemical Potential Window..... | 62 |
| 3.3.3 Capacitance-Potential Trends in the RTILs..... | 64 |
| 3.3.4 Hysteresis in Capacitance-Potential Trends in the RTILs..... | 67 |
| 3.3.5 Single Frequency Capacitance Measurements..... | 68 |
| 3.3.6 Shapes of the Capacitance-Potential Curves..... | 70 |
| 3.4 Discussion | 71 |
| 3.5 Conclusions..... | 76 |
| 3.6 Acknowledgements..... | 77 |
| REFERENCES | 78 |

Chapter 4 The Effect of Surface Oxygen on the Wettability and Electrochemical Properties of Boron-Doped Nanocrystalline Diamond Electrodes in Room Temperature Ionic Liquids..... 87

| | |
|---|-----|
| 4.1 Introduction..... | 87 |
| 4.2 Materials and Methods..... | 91 |
| 4.2.1 Boron-Doped Diamond Electrodes..... | 91 |
| 4.2.2 Surface Termination of the BDD Films..... | 92 |
| 4.2.3 Chemicals..... | 92 |
| 4.2.4 X-ray Photoelectron Spectroscopy (XPS)..... | 93 |
| 4.2.5 Scanning Electron Microscopy (SEM)..... | 94 |
| 4.2.6 Static Contact Angle Measurements..... | 94 |
| 4.2.7 Electrochemical Measurements..... | 95 |
| 4.2.8 Statistical Data Analysis..... | 97 |
| 4.3 Results..... | 98 |
| 4.3.1 BDD Surface Termination..... | 98 |
| 4.3.2 Surface Film Morphology..... | 100 |
| 4.3.3 Surface Wettability..... | 102 |
| 4.3.4 Electrochemical Potential Windows..... | 103 |
| 4.3.5 Capacitance-Potential (C-E) Trends in RTILs..... | 104 |
| 4.3.6 Capacitance-Potential (C-E) Trends in an Aqueous Electrolyte..... | 111 |
| 4.4 Discussion | 113 |
| 4.5 Conclusions..... | 116 |
| 4.6 Acknowledgements..... | 117 |
| REFERENCES | 118 |

| | |
|--|------------|
| Chapter 5 Effect of Nitrogen Incorporation on Electrode Microstructure, Voltammetric Properties and Capacitance of Nitrogen-Incorporated Tetrahedral Amorphous Carbon Thin-Film Electrodes..... | 126 |
| 5.1 Introduction..... | 126 |
| 5.2 Materials and Method..... | 127 |
| 5.2.1 RTILs..... | 127 |
| 5.2.2 Electrodes..... | 128 |
| 5.2.2.1 Nitrogen-Incorporated Tetrahedral Amorphous Carbon Thin Film Electrodes..... | 128 |
| 5.2.2.2 Boron-Doped Diamond Electrodes..... | 129 |
| 5.2.2.3 Glassy Carbon Electrodes..... | 130 |
| 5.2.3 Characterization Techniques..... | 131 |
| 5.2.3.1 Visible Raman Spectroscopy..... | 131 |
| 5.2.3.2 X-ray Photoelectron Spectroscopy..... | 131 |
| 5.2.3.3 High-Resolution Transmission Electron Microscopy (HR-TEM)..... | 132 |
| 5.2.3.4 Electron Energy Loss Spectroscopy (EELS)..... | 132 |
| 5.2.4 Electrochemical Techniques..... | 133 |
| 5.2.4.1 Cyclic Voltammetry..... | 133 |
| 5.2.4.2 Electrochemical Impedance Spectroscopy..... | 134 |
| 5.3 Results..... | 136 |
| 5.3.1 X-ray Photoelectron Spectroscopy (XPS)..... | 136 |
| 5.3.2 Raman Spectroscopy..... | 142 |
| 5.3.3 Electron Energy Loss Spectroscopy (EELS)..... | 145 |
| 5.3.4 High-Resolution Transmission Electron Microscopy (HR-TEM)..... | 146 |
| 5.3.5 Cyclic Voltammetry..... | 148 |
| 5.3.6 Electrochemical Impedance Spectroscopy..... | 150 |
| 5.4 Discussion..... | 153 |
| 5.5 Conclusions..... | 157 |
| REFERENCES..... | 159 |
| Chapter 6 Conclusions and Future Outlook..... | 165 |

LIST OF TABLES

| | |
|--|-----|
| Table 3.1. Physical properties of [BMIM][PF ₆] and [HMIM][PF ₆] at 25°C..... | 60 |
| Table 4.1. Physical properties of [BMIM][PF ₆] and [HMIM][PF ₆] at 25°C..... | 90 |
| Table 4.2. Summary of the C1s Core Level XPS Data for H-BDD, Ar-BDD and O-BDD Electrodes..... | 100 |
| Table 4.3. Capacitance values calculated from the linear regression analysis of plots of the current density (μAcm^{-2}) vs. scan rate (Vs^{-1}) for H-, Ar- and O-BDD electrodes in [BMIM][PF ₆] shown in Fig. 4.7B. Values are reported as mean \pm std. dev. for n=3 electrodes..... | 106 |
| Table 4.4. Capacitance values calculated from current density vs. scan rate plots and linear regression analysis for O-BDD and H-BDD in 0.5 mol L ⁻¹ H ₂ SO ₄ . Data are presented as mean \pm std. dev. for n = 3 electrodes of each type..... | 112 |
| Table 5.1. Summary of the relative elemental composition of <i>ta</i> -C:N _x films calculated using XPS. The % ratios were calculated by integrating the peak area for the respective elements. Shirley background subtraction method was used to define the baseline..... | 137 |
| Table 5.2. Details of C1s peak components for <i>ta</i> -C:N _{x=0, 10, 30, 50} thin films..... | 139 |
| Table 5.3. Summary of XPS data showing sp ² /sp ³ carbon content calculated from deconvoluted spectra of C1s for <i>ta</i> -C:N _x thin-films electrodes. (n = 6)..... | 142 |
| Table 5.4. Summary of visible Raman data for <i>ta</i> -C:N _x thin-films electrodes deposited in the presence of 0, 10, 30 and 50 sccm nitrogen. The G band peak center, FWHM, and I _D /I _G ratios were compared..... | 145 |

LIST OF FIGURES

| | |
|---|----|
| Figure 1.1. Atomic arrangement in different allotrope of carbon (A) graphite, (B) Diamond, and (C) Diamond-like carbon (https://www.dynasil.com/coatings/protect-your-ir-optics-with-diamond-like-carbon-dlc-coatings/ ; retrieved on August 5, 2019)..... | 2 |
| Figure 1.2. Illustration of microstructure of glassy carbon (GC) [7]. Reprinted by permission from Springer Nature: Bioanalytical Reviews. Copyright 2012..... | 3 |
| Figure 1.3. Plot of resistivity (ohm cm) vs. boron concentration (cm^{-3}) of a series of diamond films, indicating the difference in the electrical conduction mechanism [41]. Reprinted with permission from Elsevier. Copyright 1998..... | 7 |
| Figure 1.4. Ternary phase diagram of carbon and hydrogen showing the relationship among sp^2 , sp^3 and hydrogen content for diamond-like carbon [86]. Reprinted with permission from Elsevier. Copyright 2017..... | 10 |
| Figure 1.5. Evolution of electrical double layer model in aqueous electrolytes over time. The bottom panel shows proposed organization of ions at the interface and the top panel shows corresponding capacitance-potential profile: (A) Helmholtz model, (B) Gouy-Chapman model, (C) Gouy-Chapman-Stern model, and (D) Kornyshev model..... | 17 |
| Figure 1.6. Schematic illustration of overall research presented in this dissertation. <i>Abbreviations</i> – SEM: Scanning Electron Microscopy, EELS: Electron-energy Loss Spectroscopy, XPS: X-ray Photoelectron Spectroscopy, HR-TEM: High-resolution Transmission Electron Microscopy, FTIR: Fourier-transform Infrared Spectroscopy, TGA: Thermogravimetric Analysis..... | 22 |
| Figure 2.1. Schematic representation of Formvar (carbon-coated Cu grid), Ted-Pella#01883-F.. | 40 |
| Figure 2.2. Illustration of waveform for cyclic voltammetry. The potential is scanned from E_1 to E_2 at a scan rate, v , that gives DC voltammetric current..... | 42 |
| Figure 2.3. The representative electrical equivalent circuit that was used to fit the full-frequency impedance data..... | 43 |
| Figure 3.1. The electrical equivalent circuit used to fit the impedance data in the Nyquist plane... | 56 |
| Figure 3.2. (A) Comparison of TGA weight loss (%) vs. temperature profiles for as received (blue line), purified (black), and purified [BMIM][PF ₆] and atmosphere exposed (red) [BMIM][PF ₆]. (B) FTIR absorbance spectra for purified [BMIM][PF ₆] (solid line) and [HMIM][PF ₆] (dashed line)..... | 61 |

| | |
|--|-----|
| Figure 3.3. Cyclic voltammetric (<i>j</i> - <i>E</i>) curves for a BDD planar electrode in purified [HMIM][PF ₆] (black) and [BMIM][PF ₆] (red). Scan rate = 0.1 V s ⁻¹ | 63 |
| Figure 3.4. Cyclic voltammetric <i>j</i> vs. <i>E</i> curves recorded as a function of scan rate (0.01 to 0.5 Vs ⁻¹) for a BDD planar electrode in (A) [HMIM][PF ₆] and (B) [BMIM][PF ₆]. (C) Plots of log <i>j</i> at 0.2 V vs. log <i>ν</i> for the same electrode in the two RTILs. (D) Comparison of the cyclic voltammetric <i>j</i> vs. <i>E</i> curves for the BDD electrode in the two RTILs at 0.1 Vs ⁻¹ | 64 |
| Figure 3.5. (A) Nyquist plot of the real (<i>Z'</i>) vs. imaginary (<i>Z''</i>) components of the total impedance for BDD in [HMIM][PF ₆] at 0.3 V. The inset show dependence of α on the potential. (B) Representative Bode plot for log <i>Z</i> and phase angle vs. log frequency for [HMIM][PF ₆] at 0.3 V. (C) Bulk resistance for [BMIM][PF ₆] (red circles) and [HMIM][PF ₆] (black squares) as a function of potential. (D) Capacitance vs. potential (<i>C</i> - <i>E</i>) profiles for BDD in contact with [HMIM][PF ₆] (black squares) and [BMIM][PF ₆] (red circles). The <i>C</i> - <i>E</i> profiles were generated from EIS data by fitting the full frequency spectrum at each potential. Values are presented as mean \pm std. dev. for $n \geq 3$ measurements with different BDD electrodes in each RTIL..... | 66 |
| Figure 3.6. Capacitance vs. potential (<i>C</i> - <i>E</i>) data for a BDD planar electrode recorded in [HMIM][PF ₆]. Capacitance values were determined from the full spectrum EIS data recorded from negative to positive potentials in the forward direction (black squares), and from positive to negative potentials in the reverse direction (red circles)..... | 68 |
| Figure 3.7. (A) Log capacitance-potential curves generated from the single frequency impedance technique for BDD in [HMIM][PF ₆] as a function of a fixed AC frequency. The arrow indicates increasing frequency from 0.1 to 600 Hz. (B) Capacitance at -0.5 V as a function of log frequency. ($R^2 = 0.75$). Values are reported as mean \pm std. dev. for $n \geq 3$ measurements with different BDD electrodes..... | 69 |
| Figure 3.8. A. Comparison of the cyclic voltammetric <i>j</i> vs. <i>E</i> curves recoded at 0.1 Vs ⁻¹ for BDD (black inner curve) and Au (red outer curve) in [HMIM][PF ₆]. (B) Capacitance-potential curves for Au film and BDD electrode in contact with [HMIM][PF ₆]. The capacitance values were determined from the full frequency spectrum EIS data. Values are reported as mean \pm std. dev. for $n \geq 3$ measurements with different BDD electrodes..... | 70 |
| Figure 4.1. The representative electrical equivalent circuit that was used to fit the full-frequency impedance data [52,54]..... | 96 |
| Figure 4.2. XPS survey scans for (A) H-BDD (black curve), (B) Ar-BDD (blue curve) and (C) O-BDD (red curve) thin-films after the different microwave or RF plasma treatments in H ₂ , Ar and O ₂ , respectively..... | 99 |
| Figure 4.3. Deconvoluted C1s spectra revealing the carbon-oxygen functional group types, C-OH, C=O and HO-C=O, present on (A) H-BDD, (B) Ar-BDD and (C) O-BDD electrodes..... | 100 |
| Figure 4.4. SEM micrographs of a nanocrystalline BDD thin-film (A) before and (B) after a 12-min O ₂ RF plasma treatment..... | 101 |

Figure 4.5. The upper panels illustrate the surface terminating oxygen functional groups on the H-, Ar- and O-BDD surfaces. Photographs of droplets and static contact angle data for water (A-C) and for [BMIM][PF₆] (D-F) on the three surfaces. Values are reported as mean \pm standard deviation (n = 5 measurements on different areas of each BDD electrode)..... 103

Figure 4.6. Cyclic voltammetric *j*-*E* curves for a H-BDD thin-film electrode in (A) [HMIM][PF₆] and (B) [BMIM][PF₆] over a wide potential window of 6 V (dash curves). The narrower potential region of ~ 2 V (solid curves) used for the capacitance measurements is also shown (solid curve). The insets show *j*-*E* curves for H-BDD over a more narrow 1.5 V potential range in (A) [HMIM][PF₆] and (B) [BMIM][PF₆]. Scan rate = 0.1 Vs⁻¹.....104

Figure 4.7. (A) Cyclic voltammetric (*j*-*E*) curves recorded as a function of scan rate (0.01 to 0.5 Vs⁻¹) for H-BDD thin-film electrode in [BMIM][PF₆]. (B) A plot of background current density, *j*, at 0.0 V vs. Ag QRE against scan rate for H-BDD (■), Ar-BDD (●) and O-BDD (▲). Current density values are the average of the positive and negative sweeps in the cyclic voltammogram. Values are plotted as mean \pm std. dev. (n=3 electrodes).....105

Figure 4.8. (A) Overlay of cyclic voltammetric *j*-*E* curves recorded at 0.1 Vs⁻¹ for H-BDD (black curve), Ar-BDD (blue curve) and O-BDD (red curve) in [BMIM][PF₆]. (B) Corresponding capacitance-potential (*C*-*E*) curves for H-BDD (●), Ar-BDD (●), and O-BDD (▲) in [BMIM][PF₆]. The capacitance values were calculated from the $j_{average}$ (μAcm^{-2})/ ν (Vs⁻¹) values according to equation 1. Capacitance values are presented for just one of each modified electrode.....107

Figure 4.9. (A) Overlay of cyclic voltammetric *j*-*E* curves recorded at 0.1 Vs⁻¹ for H-BDD (black curve), Ar-BDD (blue curve), and O-BDD (red curve) in [HMIM][PF₆]. (B) Corresponding capacitance-potential (*C*-*E*) curves for H-BDD (■), Ar-BDD (●), and O-BDD (▲) in [HMIM][PF₆]. The capacitance values were calculated from the $j_{average}$ (μAcm^{-2})/ ν (Vs⁻¹) values according to equation 1. Capacitance values are presented for just one of each modified electrode.....108

Figure 4.10. Stacked Nyquist plots of the real (*Z'*) vs. imaginary (*Z''*) components of the total impedance for an H-BDD thin-film electrode in (A) [HMIM][PF₆] and (B) [BMIM][PF₆] as a function of applied potential.....109

Figure 4.11. Comparison of capacitance-potential (*C*-*E*) trends recorded for H-BDD (■), Ar-BDD (●) and O-BDD (▲) in (A) [HMIM][PF₆] and (B) [BMIM][PF₆]. The capacitance values were calculated from EIS data. The data are plotted as mean \pm standard deviation for n=3 electrode... 110

Figure 4.12. (A) Cyclic voltammetric (*j*-*E*) curves for O-BDD (outer red curve) and H-BDD (inner black curve) in 0.5 M H₂SO₄. Scan rate = 0.1 Vs⁻¹. (B) A plot of corresponding current density at 0.0 V vs. Ag QRE against scan rate for O-BDD (○) and H-BDD (□) in 0.5 mol L⁻¹ H₂SO₄. Current density values are presented as mean \pm std. dev. for n=3 electrodes of each type.....112

Figure 4.13. Comparison of capacitance-potential (*C*-*E*) profiles for O-BDD (○) and H-BDD (□) in 0.5 mol L⁻¹ H₂SO₄. The capacitance values were calculated from EIS data. Capacitance values are presented as mean \pm std. dev. for n=3 electrodes of each type.....113

| | |
|--|-----|
| Figure 5.1. The representative electrical equivalent circuit that was used to fit the full-frequency impedance data..... | 135 |
| Figure 5.2. XPS survey spectra of <i>ta</i> -C:N ₀ (black curve), <i>ta</i> -C:N ₁₀ (red curve), <i>ta</i> -C:N ₃₀ (blue curve), and <i>ta</i> -C:N ₅₀ (pink curve) films over a wide energy range from 0 to 1100 eV. The highlighted areas represent C1s, N1s, and O1s region <i>ca.</i> 285, 400, and 530 eV, respectively.... | 136 |
| Figure 5.3. Plots of the N/C (●) and O/C (■) atomic ratios as a function of nitrogen flow rate during the growth of <i>ta</i> -C:N _x films. The ratios were calculated from C1s, N1s and O1s peak area integration. The error bar represents standard deviation. (n = 2)..... | 137 |
| Figure 5.4. Deconvoluted peak fits of core C1s energy region of the XPS spectra showing sp ² C, sp ³ C, C-N, C=N and C=O functional groups for <i>ta</i> -C:N _x films: (A) <i>ta</i> -C:N ₀ , (B) <i>ta</i> -C:N ₁₀ , (C) <i>ta</i> -C:N ₃₀ , and (D) <i>ta</i> -C:N ₅₀ | 138 |
| Figure 5.5. Deconvoluted peak fits of core N1s energy region of the XPS spectra showing nitrogen-oxygen and nitrogen-carbon functional groups for <i>ta</i> -C:N _x films: (A) <i>ta</i> -C:N ₀ , (B) <i>ta</i> -C:N ₁₀ , (C) <i>ta</i> -C:N ₃₀ , and (D) <i>ta</i> -C:N ₅₀ | 140 |
| Figure 5.6. Deconvoluted peak fits of core O1s energy region of the XPS spectra showing oxygen-sp ² C and oxygen-sp ³ C functional groups for <i>ta</i> -C:N _x films: (A) <i>ta</i> -C:N ₀ , (B) <i>ta</i> -C:N ₁₀ , (C) <i>ta</i> -C:N ₃₀ , and (D) <i>ta</i> -C:N ₅₀ | 141 |
| Figure 5.7. Visible Raman spectra of boron-doped diamond (blue curve), glassy carbon (black curve), and <i>ta</i> -C:N ₃₀ (red curve) thin-film electrode..... | 143 |
| Figure 5.8. Visible Raman spectra of <i>ta</i> -C:N _x thin-film electrodes grown in the presence of different levels of nitrogen flow rate, <i>ta</i> -C:N ₀ (black curve), <i>ta</i> -C:N ₁₀ (red curve), <i>ta</i> -C:N ₃₀ (blue curve), and <i>ta</i> -C:N ₅₀ (pink curve)..... | 144 |
| Figure 5.9. Plot of intensity of D band (I _D)/intensity of G band (I _G) calculated from visible Raman spectra of <i>ta</i> -C:N _x thin-film as a function of different levels of nitrogen flow rate during growth..... | 145 |
| Figure 5.10. Electron energy loss spectra (EELS) at the C-K edge for <i>ta</i> -C:N ₀ (black curve), <i>ta</i> -C:N ₁₀ (red curve), <i>ta</i> -C:N ₃₀ (blue curve), and <i>ta</i> -C:N ₅₀ (pink curve). (B) Corresponding sp ² /sp ³ ratio calculated from peak area under π* and σ* excitations as a function of <i>ta</i> -C:N _x films deposited with 0, 10, 30 and 50 sccm nitrogen. The error bars represent standard deviation for 12 measurements..... | 146 |
| Figure 5.11. Representative HR-TEM images of different regions of <i>ta</i> -C:N ₀ , <i>ta</i> -C:N ₁₀ , <i>ta</i> -C:N ₃₀ , and <i>ta</i> -C:N ₅₀ films. The red and blue colored rectangular frames represent domains with interlayer spacing close graphite and diamond, respectively. The arrows indicate rippled-like microstructure..... | 147 |

- Figure 5.12.** Cyclic voltammetric j - E curves for BDD (black curve), ta -C:N₀ (red curve), ta -C:N₁₀ (blue curve), ta -C:N₃₀ (pink curve), ta -C:N₅₀ (green curve), and glassy carbon (yellow curve) electrodes in [HMIM][PF₆]. The corresponding potential windows for BDD, ta -C:N₀, ta -C:N₁₀, ta -C:N₃₀, ta -C:N₅₀, and GC are 6, 4.5, 4.5, 4.0, 3.5, and 3.0 V vs. Ag QRE, respectively. Scan rate = 0.1 V s⁻¹.....148
- Figure 5.13.** Cyclic voltammetric j - E curves for (A) ta -C:N₀ (B) ta -C:N₁₀ (C) ta -C:N₃₀ and (D) ta -C:N₅₀ thin-film electrodes in [HMIM][PF₆] as a function of scan rate (0.01 to 0.5 V s⁻¹). The scale of y-axis (current density) is kept constant for comparison purposes.....149
- Figure 5.14.** Log-log plot of current density, j , at 0 V vs. scan rate, v , in [HMIM][PF₆].....150
- Figure 5.15.** Representative admittance plot of ta -C:N₃₀ in [HMIM][PF₆] at 0.1 V vs. Ag QRE. The black dash line represents fit to the equivalent circuit. The red circle demarks the impedance data in high frequency range (> 21 kHz) that corresponds to C_{hf} element.....151
- Figure 5.16.** Capacitance-potential (C- E) profiles for (A) ta -C:N₀ (B) ta -C:N₁₀ (C) ta -C:N₃₀ and (D) ta -C:N₅₀ thin-film electrodes in [HMIM][PF₆]. The C- E profiles were generated using the impedance data in the full frequency (0.1 to 10⁵ Hz) spectra. Mean values of capacitance taken from three independent sets of experiments were plotted. The error bars represent standard deviation for $n = 3$152
- Figure 5.17.** Capacitance vs. potential profile for ta -C:N₃₀ electrode in [HMIM][PF₆] at 0.1 V vs. Ag QRE. The total capacitance (▲) term was deconvoluted into two capacitive processes C_{EDL} (■) and C_{bulk} (●) using Cole terms in the complex plane impedance analyses.....153

Chapter 1

Introduction

1.1 Carbon Electrodes

Carbon atom's unprecedented ability to bond with itself and form different stable allotropes having an incredibly diverse range of physical, chemical, and electrical properties is central to its uniqueness. Broadly categorized based on hybridization, carbons are of two kinds: one, of graphitic (sp^2) nature that forms allotropes such as graphene, carbon nanotubes, glassy carbon (GC), and highly-ordered pyrolytic graphite (HOPG) with different atomic arrangements, and two, of exclusively sp^3 -hybridized diamond-form where the carbon atoms are arranged in a tetrahedral configuration. Figure 1.1A illustrates the atomic arrangement of the carbon atoms in graphite where one carbon atom forms three σ bonds in the x - y plane (bond length: 0.142 nm) with three neighboring carbon atoms creating a hexagonal arrangement of atoms in a 2D lamellar structure. The fourth valence electron in the $2p_z$ orbital does not participate in σ bonding and remains available to form a π bond. The individual sheets (later termed graphene) are separated by 0.35 nm in the z -direction and are held together by weak van der Waals forces. The carbon atoms on the edges have high activity for adsorption due to the exposed empty $2p_z$ orbitals and readily react with atmospheric oxygen to form functional groups such as hydroxyl, carbonyl, carboxylic acid, etc. and are termed as the “*edge*” plane sites. In contrast, the carbon atoms in the x - y plane form the “*basal*” plane and are known to be less active towards adsorption and electron transfer.

Diamond is a cubic allotrope of carbon, made of sp^3 -hybridized atoms, bound together by σ bonds. It exists in a tetrahedral configuration, packed in a face-centered cubic lattice (Figure

1.1B). The σ bonds are responsible for the fundamental properties of diamond. Intrinsically, diamond is an insulator with a wide bandgap of 5.47 eV at $T = 300$ K. However, for use as an electrode, diamond can be doped to create a n-type or a p-type diamond with intermediate energy levels that lowers the band gap. This modulation of the diamond's band gap has been discussed in detail later in the chapter. In between the purely sp^2 and purely sp^3 carbon materials, diamond-like carbon presents a class of amorphous carbon with tunable sp^2/sp^3 content (Figure 1.1C).

Among the various allotropes of carbons, research in this dissertation made use of glassy carbon (GC), boron-doped diamond and *ta*-C:N as a representative of pure sp^2 , pure sp^3 , and hybrid sp^2/sp^3 carbon, respectively.

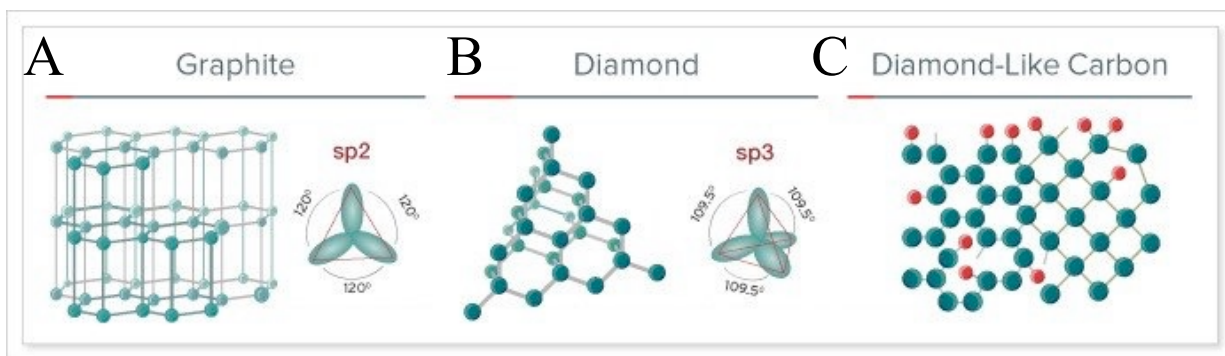


Figure 1.1. Atomic arrangement in different allotrope of carbon (A) graphite, (B) Diamond, and (C) Diamond-like carbon (<https://www.dynasil.com/coatings/protect-your-ir-optics-with-diamond-like-carbon-dlc-coatings/>; retrieved on August 5, 2019).

1.1.1 Glassy Carbon (GC)

GC, also known as vitreous carbon, is an amorphous allotrope of sp^2 carbon. It is synthesized by controlled pyrolysis of organic polymers usually at temperatures between 1500 to 2500 °C [1]. It consists of randomly-oriented, disordered, and intertwined ribbon-like structures that are 15-70 Å in the lateral dimension with an interplanar spacing of 3.5 nm [2–4], as shown in

Figure 1.2. These ribbon-like structures have pores that are 3.5-100 Å in size [5], [6]. Owing to microstructural disorder, GC usually has a high ratio of exposed “edge” plane sites and a relatively low density of 1.5 gcm⁻³.

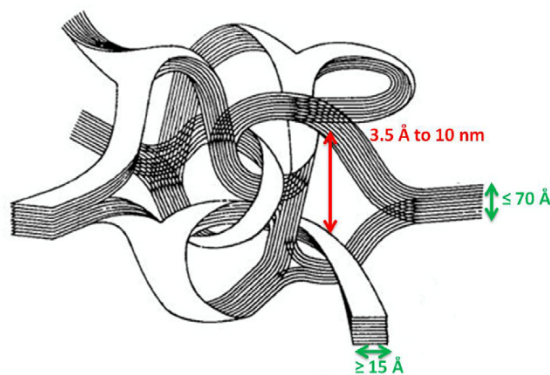


Figure 1.2. Illustration of microstructure of glassy carbon (GC) [7]. Reprinted by permission from Springer Nature: Bioanalytical Reviews. Copyright 2012.

1.1.1.1 GC as an Electrode

In the field of electrochemistry, GC has been extensively used as an electrode since it was first produced in the mid-1960s. Its high conductivity, high-temperature resistance, wide availability, and low cost made it to be widely employed for electrochemical applications [8–10]. Compared to metals, GC has relatively low background current and a wide potential window [11].

Although GC is chemically inert, the sp² carbon content and the oxygen-containing surface functional groups make it vulnerable towards molecular adsorption through empty 2p_z π-orbitals of the carbon and oxygen atoms. High susceptibility to surface deactivation/fouling due to adventitious adsorption necessitates rigorous electrode pre-treatment before any electrochemical use. Pre-treatment includes conditioning the electrode surface, microstructure, and chemistry to lower the background current and expose the active sites on the surface. One of the easiest methods to reveal the new, clean, and active surface sites on a GC surface is to mechanically polish it with

alumina powder [2]. However, as each polishing procedure reveals a new underlying surface with potentially different properties, pre-treatment can change the electrochemical activity of the GC electrodes [2,5,12–17]. Furthermore, the electrochemical area, which depends on the roughness of the electrode surface, can vary with each polishing procedure. Furthermore, the electrical conductivity in GC also varies with the temperature of pyrolysis during manufacturing, structural disorder, and the density of surface functional groups [11,18]. Thus, GC's high sensitivity towards surface treatment and history leads to variation in its electrochemical activity. Moreover, the π orbitals are susceptible to adsorption, microstructural changes at high potentials and relatively higher background current among carbon electrodes.

1.1.2 Boron-doped Diamond (BDD)

Intrinsically, diamonds are insulators with a wide bandgap of 5.47 eV at $T = 300$ K. However, for use as an electrode, diamond can be doped to create a n-type or a p-type diamond with intermediate energy levels that lowers the band gap. For n-type diamond, a group V element, *e.g.*, nitrogen, can act as a donor thereby creating a donor energy level 1.6 eV below the conduction band; and, for p-type doping, a group III element, *e.g.*, boron (from B_2H_6), acts as an acceptor creating an acceptor level 0.36 eV above the valence band [19,20]. Boron atoms with their atomic size closer to that of carbon get readily incorporated into the dense crystal lattice of diamond and form a stable bond. It is the substitutionally-inserted boron that provides charge carriers to the material and electrical conductivity. As such, boron is the choice of dopant for diamond, and boron-doped diamond (BDD) the most common diamond-based material for electrochemical applications, particularly the highly boron-doped ($\sim 10^{21} \text{ cm}^{-3}$), semi-metallic forms of the material.

Chemical vapor deposition (CVD) is the most-commonly used method to produce high-quality diamonds with tunable and relatively consistent properties. CVD produces diamond under metastable conditions, where carbon atoms are added one-by-one to a template to form a tetrahedrally-bonded network [21]. The process mainly involves a carbon-containing gas phase, typically 0.1 to 5% (v/v), mixed with the background hydrogen gas at temperatures over 2000 K giving rise to microwave plasma. A dopant source, for example, diborane (B_2H_6) for boron doping in the case of BDD, is added as required. The gas molecules fragment into highly reactive radicals, ions, and electrons which react and diffuse until they hit the substrate surface where they get nucleate on the surface and proceed to grow in all dimensions simultaneously. The growth rate is non-uniform as certain grains with preferential facets, and orientation grow at a faster rate than others. Eventually, the growing crystals coalesce to form a continuous film and start growing upwards. The grain size increases with the film thickness, resulting in fewer grain boundaries at the surface. Using this technique, polycrystalline BDD can be grown in a wide range of grain sizes from ultrananocrystalline and nanocrystalline to microcrystalline.

In CVD, the atomic hydrogen formed from the breakdown of hydrogen plays several critical roles in the growth mechanism: (i) it reacts with the source hydrocarbon species to make methyl (CH_3) radicals that get adsorbed on the substrate surface, (ii) it terminates the ‘surface dangling bonds’ of sp^3 hybridized carbon to avoid cross-linking and reconstruction to sp^2 form, and (iii) it etches sp - and sp^2 -phase at a faster rate than sp^3 carbon, thereby removing any graphitic carbon clusters, while leaving behind the diamond phase. The substrate used for growing diamond strongly influences the quality of diamond grown: its melting point, coefficient of thermal expansion, ability to form carbide, as well as the crystal orientation, affect the growth rate and quality [22]. Most commonly used substrates include Si, Mo, W, Ti, and diamond itself. Substrate

pre-treatment is another important factor that influences the quality of diamond. The work presented in this dissertation uses a nanocrystalline BDD thin-film electrode grown on a Si substrate.

1.1.2.1 BDD as an Electrode

With its low background current due to the lower density of states (DOS) present at the Fermi level [23] and wide potential window, BDD makes for an excellent electrode material [24–29]. These superior properties of BDD stem from the chemical inertness of sp^3 bonds on the BDD surface that do not support surface redox processes that would otherwise contribute to the background current [30–38]. However, these remarkable chemical, physical, and electrochemical properties depend significantly on the quality of the grown diamond film. For example, the presence of non-diamond sp^2 carbon impurities can make the electrode more reactive towards oxygen and water, and allow adventitious adsorption of some molecular species resulting in surface fouling, thereby reducing the potential window [39].

Various factors such as doping level, surface termination, crystal size play a significant role in electrochemical behavior of diamond. Controlling the doping level in diamonds allows for precise modulation of the density of states (DOS). A boron doping density of at least $\sim 10^{17} \text{ cm}^{-3}$ is required for the minimum number of charge carriers to make the doped diamond conductive [40]. While a boron doping density of $\sim 10^{18} \text{ cm}^{-3}$ produces an extrinsic semiconductor with ohmic resistance of $\sim 10^4 \Omega$, a doping level of $\sim 10^{20} \text{ cm}^{-3}$ produces a semi-metal with an ohmic resistance of $\sim 10^{-2} \Omega$ [19,40]. The mechanism of conduction varies with the dopant atomic concentration: from valence band conduction observed for low-doped (*ca.* $< 10^{18} \text{ cm}^{-3}$) diamond to metallic

conduction for the heavily-doped ($ca. > 10^{20} \text{ cm}^{-3}$) one, as shown in Figure 1.3. Between these two limits, hopping conduction is observed [41,42].

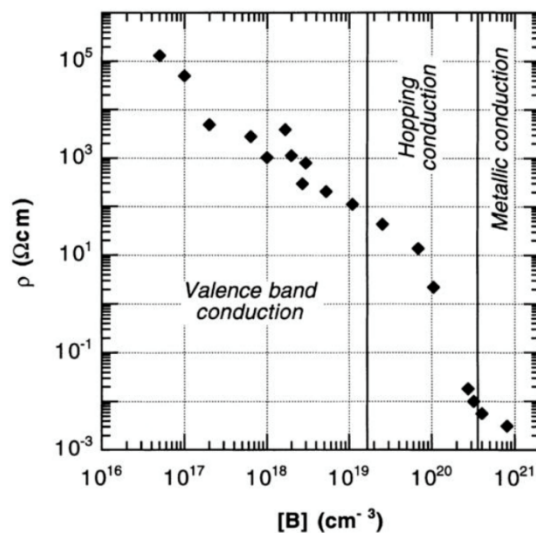


Figure 1.3. Plot of resistivity (ohm cm) vs. boron concentration (cm^{-3}) of a series of diamond films, indicating the difference in the electrical conduction mechanism [41]. Reprinted with permission from Elsevier. Copyright 1998.

In addition to the boron doping level, surface termination of the BDD electrode is another crucial factor which influences its electrochemical properties. When grown *via* CVD, the diamond has a non-polar hydrogen-terminated surface. While the hydrogen-terminated surface is relatively stable over months, gradual oxidation of the surface can occur. When it is anodically polarized, oxidation occurs at a much faster rate. Oxygen-terminated BDD surface is known to be more stable in air and under potential control. Additionally, the hydrophilic nature of the oxygen-terminated BDD surface shows higher activity for some electron transfer reactions that require adsorption of intermediate chemical species. Several methods, including boiling in acid [43], exposure to oxygen plasma [33], photochemical oxidation [44], anodic polarization [45] have been used to make the BDD surface oxygen-terminated. Oxygen-termination is reported to add functional groups like C-OH, C-O-C, and $>\text{C}=\text{O}$ to the BDD surface [46, 47]. The nature of the surface-termination can be ascertained by measuring water contact angles on the BDD surface. While hydrogen-termination

usually results in a hydrophobic surface with a contact angle exceeding 90° , oxygen-termination provides a hydrophilic surface with a contact angle ranging from 0 to 65° [48].

Surface termination is also known to influence the conductivity of the thin-film electrode. Since 1989, it has been known that the intrinsic hydrogen-terminated diamond possesses additional surface conductivity due to p-type charge carriers present in the accumulation layer [49,50]. Initially, it was attributed to doping *via* the sub-surface hydrogen [48]. Later in 2000, it was found that atmospheric adsorbates are also required for the observed surface conductivity through a process called surface transfer doping [51]. Due to dissociation of atmospheric CO_2 to H_3O^+ and HCO_3^- , a wetted layer of solvated hydronium ions and corresponding anions is expected to form on the electrode surface exposed to air. It is proposed that the chemisorbed hydrogen species lower the ionization potential of the diamond surface, while the hydronium/hydrogen adsorbate couple provides the potential driving force for the electron transfer from the diamond, thus leaving an accumulation of holes at the surface [52]. Also, the differences in the electronegativities of carbon, hydrogen, and oxygen atoms result in the formation of localized dipoles on the surface, which can change the affinity of the BDD surface [52]. For example, hydrogen-termination lowers the electron affinity of the BDD surface, whereas oxygen-termination results in an increase in the electron affinity [53,54]. Furthermore, the surface band structure is also impacted by the surface termination. Charge carrier transfer can occur between the bulk BDD and the surface states causing surface band bending and a space charge layer that extends hundreds of nanometers into the bulk. The method employed for inducing different surface termination most often changes the surface states, and, hence, the band structure. The flat band potential (E_{fb}) of hydrogen-terminated semiconducting BDD has been reported to fall between 0 to 0.75 V *vs.* SCE [47, 55], while that it lies between 1 to 4 V *vs.* SCE [47,56] for oxygen-terminated diamond.

The electrical and electrochemical heterogeneity of polycrystalline BDD is another important consideration for electrode applications. A polycrystalline surface has different crystal orientations, which uptake boron at different rates during the growth, producing grains of varying conductivity [20,40,57]. Apart from the conductivity, it is also known that the crystal orientations itself have different electrochemical properties [58]. For example, [111] crystal face uptakes boron 10 times readily than [100] faces [57,58]. Various spatial mapping techniques like conducting atomic force microscopy (C-AFM) and scanning electrochemical microscopy (SECM) have been used to probe the local resistivity and electrochemical activity of BDD surface [59] [60]. Thus, a detailed characterization of the BDD electrode is required to establish the structure-electrochemical property relationship.

Though BDD exhibits excellent properties for its use as an electrode material, there are a few complexities associated with it [61]. Firstly, to grow a good quality diamond, the substrate must be pretreated to achieve high nucleation density. Mechanical polishing or sonication with small diamond nanoparticles is a commonly employed method. However, this process is time-consuming, and the quality of pretreatment directly influences the quality of diamond. Consequently, this step is often not reproducible. Secondly, diamond needs temperatures in excess of 800 °C for growth which severely limits the choice of substrates that can be used to grow diamond. The substrate needs to withstand such high temperature with no phase change and should be able to form a stable carbide interfacial layer to initiate the growth [62]. Thirdly, the substrate needs to have a coefficient of thermal expansion that matches closely with that of diamond to avoid build-up of intrinsic stress. Furthermore, the growth time to obtain continuous diamond film is often 5-7 hours.

1.1.3 Nitrogen-incorporated tetrahedral amorphous carbon (*ta*-C:N)

Nitrogen-incorporated tetrahedral carbon (*ta*-C:N) is an amorphous diamond-like allotrope of carbon with a random arrangement of sp^2 - and sp^3 -bonded carbon with no long-range order. A wide range of this amorphous material can be grown by varying the sp^2/sp^3 ratio and incorporating impurities like hydrogen and nitrogen. Figure 1.4 shows the ternary phase diagram of carbon and hydrogen showing the relationship among sp^2 - and sp^3 -bonded carbon and hydrogen content for diamond-like carbon. As a hybrid material, *ta*-C:N boasts of some of the diamond's superlative properties like excellent mechanical strength, high thermal conductivity, low background current and anti-fouling nature. The origin of these properties is most likely linked to the high sp^3 content in the films. One of the main reasons for the growing popularity of *ta*-C:N electrodes is the ease of growing them. Compared to BDD, growing *ta*-C:N electrodes offers several advantages – it doesn't require any seeding and can be grown at much lower temperatures of 25-100 °C. This lower growth temperature opens up the possibility to grow these electrodes on a wide range of substrates including non-traditional ones like plastics.

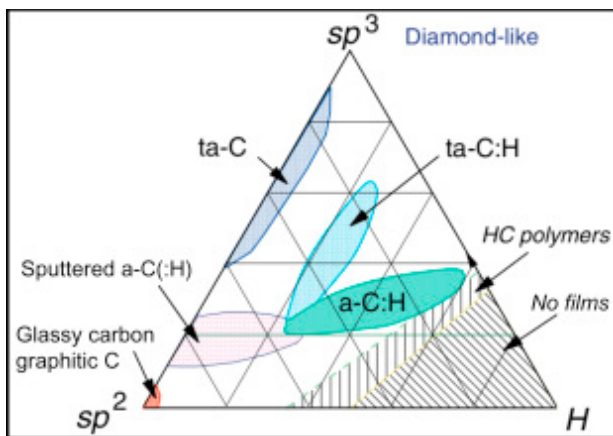


Figure 1.4. Ternary phase diagram of carbon and hydrogen showing the relationship among sp^2 , sp^3 and hydrogen content for diamond-like carbon [86]. Reprinted with permission from Elsevier. Copyright 2017.

1.2 Room Temperature Ionic Liquids (RTILs)

Room temperature ionic liquids (RTILs) are highly concentrated (3-7 M) molecular solvents that have a melting point below 100 °C. They are stand-alone electrolytes, *i.e.*, they contain *no* dielectric solvent (and therefore, have no solvation sphere) [63–65]. Typically, the RTIL consists of a large, asymmetrical organic cation containing a cyclic carbon structure and a long alkyl chain, and a weakly coordinated anion that can be a small inorganic halide ion or a larger-sized organic ion. The polarizability and asymmetry in the shape and size of cation and anion hinder the formation of a stable ionic lattice. These molecular differences give rise to a range of interesting properties of RTILs that are not displayed by traditional aqueous or non-aqueous electrolytes. RTILs, in general, have large electrochemical potential windows (3 to 6 V), low volatility (zero to negligible vapor pressure), moderate conductivity (0.01 to 1.8 Sm⁻¹) and high viscosity (100 to 1000 mPs). Availability of many constituent cations and anions that can be mixed and matched provides a wide functional space to tune the physicochemical properties such as viscosity, conductivity, and polarity [66–68]. Thus, a rationally chosen task-specific RTIL can be used to drastically improve the functionality and properties of an electrochemical system. These properties make RTILs an advantageous solvent for catalysis, sensing, carbon dioxide capture/conversion technologies, and electrolytes for energy storage [64, 69–72]. Most of these applications require an in-depth understanding of the organization of the RTIL ions at the solid electrode, which dictates the structural and dynamic aspects of the electrochemical system. However, these features are poorly understood, and this is the main bottleneck in the development and engineering of RTIL-based technologies. This can be gauged by the fact that there is no model to describe the molecular organization of ions at carbon electrodes. Therefore, developing a better understanding of the interfaces of RTILs make with different carbon-based electrodes is of utmost importance.

1.3 Electrical Double Layer Models

In an electrochemical system, the electric double layer theory describes the structure of the electric interface (electrode-electrolyte solution) [73,74]. The electrical double layer is comprised of counter ions and solvent dipoles organized at the electrode surface in response to a change in the excess surface charge on the electrode, which is potential-dependent. EDL in aqueous electrolytes has been extensively studied for over a century and the descriptive theory is well-accepted in the electrochemistry community. An overview of the history as well as the current understanding of the EDL theory that forms the basis to understand the EDL in RTILs is given here.

The earliest model that describes the EDL near electrodes was given by Helmholtz, who introduced the concept of “*electrical double layer*” in 1853 [75]. The model predicts that there is one layer of counter ions next to the charged electrode (as shown in Figure 1.5A), arising due to the electrostatic attraction from the charges on the electrode surface [75]. This layer strongly interacts with the electrode surface electrostatically and is called the compact/Helmholtz layer. The Helmholtz double layer model is essentially two oppositely charged layers ($\pm q$) separated by a distance $\delta = x$, analogous to parallel plates separated by a certain distance, otherwise termed as a capacitor with capacitance:

$$C = \frac{q}{\Phi} \quad (i)$$

where Φ is the potential across the two charged layers. From parallel plate capacitor theory, $C \propto \frac{1}{\delta}$. As the double layer theory becomes more sophisticated, the charge is not necessarily linear with potential. A more useful measurement includes ‘excess charge’ or ‘differential capacitance’, the derivative of surface charge, q with respect to Φ :

$$C_H = \frac{dq}{d\phi} = \frac{\epsilon\epsilon_0}{x} \quad (\text{ii})$$

where ϵ and ϵ_0 is the dielectric constant of the electrolyte and free space. This model implies that the potential drops linearly within the compact layer of counter ions. Although this simple model was a pioneering contribution at the time, it did not explain variations in capacitance with applied potential and electrolyte ion concentration.

In 1910, Louis Georges Gouy suggested that the thermal motion of ions would prevent them from making a rigid charged layer. Rather ions form a diffuse layer governed by electrostatic potential and the thermal motion of ions. He calculated the three-dimensional diffused distribution of ions using the Poisson-Boltzmann equation [73]. The diffuse layer of counter ions had a net charge equal and opposite to the electrode charge, and the potential dropped exponentially over this extended layer (Figure 1.5B). However, the model was not valid at high potentials due to modeling ions as point charges. The model overestimated the capacitance or charge at high potentials. Neglecting the finite size of ions resulted in an overestimation of the capacitance as there was no physical limit on the number density of ions that can get accommodated at the interface. David Leonard Chapman in 1913 provided a mathematical interpretation of the model [76]. According to Gouy-Chapman theory, the differential capacitance is given by:

$$C_d = \left(\frac{2z^2e^2\epsilon\epsilon_0n^0}{kT} \right)^{1/2} \cosh \left(\frac{ze\phi_0}{2kT} \right) \quad (\text{iii})$$

where e is the electron charge, z is the ion valency, k is the Boltzmann constant, T is the absolute temperature, and ϕ_0 is the potential drop over the diffuse layer.

Later in the 1920s, Otto Stern combined Helmholtz's model and the Gouy-Chapman diffuse layer model [74]. He divided the EDL into two regions: (i) the innermost layer of oriented

solvent molecules and counter balancing electrolyte ions known as the Helmholtz layer, and (ii) an outer loosely bound extended diffuse layer of counter-ions as shown in Figure 1.5C. Considering the ions' size, he proposed a physical limit on the density of ions at the interface. Thus, a more accurate, rigorous concept could be established mathematically by adding two capacitors in series, the Helmholtz layer capacitance (C_H) and the diffuse layer capacitance (C_{diff}), to obtain the double layer capacitance (C_{DL}). This relationship is given as:

$$\frac{1}{C_{DL}} = \frac{1}{C_H} + \frac{1}{C_{diff}} \quad (iv)$$

$$\frac{1}{C_{DL}} = \frac{x}{\epsilon\epsilon_0} + \frac{1}{(2\epsilon\epsilon_0 z^2 e^2 c_0 / kT)^{1/2} \cosh(ze\phi_2 / 2kT)} \quad (v)$$

where x is the plane of closest approach (the distance between electrode surface and closed adsorbed ions) and ϕ_2 is the local potential at the outer Helmholtz plane.

While the Gouy-Chapman-Stern (GCS) model successfully explained the EDL in general, it failed to explain certain experimental observations concerning local interactions among ions, surface, or solvent molecules. It assumed a monolayer of solvent molecules adsorbed at the electrode. Later, David C. Grahame recognized the possibility of specific adsorption, and proposed a more sophisticated model in 1947 to account for the size of electrolyte ions, solvation effects, and specific adsorption of ions at the electrode surface [77]. He further divided the Helmholtz layer into two sub-layers: (i) an inner layer consisting of counter-ions with their partially or fully stripped solvation shell, and solvent molecules adsorbed at the electrode surface with their dipoles oriented towards the electrode charge. A hypothetical plane that goes through the center of the solvent molecules and partially stripped counter-ions is known as Inner Helmholtz plane (IHP), (ii) an outer Helmholtz plane (OHP) that goes through the center of counter-ions with full solvation shell. Outside OHP lies the Gouy-Chapman diffuse layer that extends further into the bulk region. To

consider the presence of solvent molecules at the electrode interface instead of treating them as a backdrop for the ions presented a significant refinement over the previous model. Also, the exact distance of ions away from the electrode surface could be calculated. Later, in 1954, Parsons introduced the concept of the plane of closest approach, which tells how close the ions can get to the electrode surface with or without the solvation sphere [78]. This concept of the plane of closest approach has been the basis for elucidating the mechanism of inner and outer sphere electron-transfer reactions and has been widely accepted in the electrochemistry community. These EDL models discussed so far set the stage for the discussion of EDL in RTILs which comes later in the dissertation.

However, these theories account only for the electrolyte side of the interface. It was assumed that the electrode side is not a governing factor in determining the EDL capacitance. This assumption is valid for metal electrodes which have infinite charge carriers at the electrode to hold the charge, when external potential is applied. As a result, the electronic phase (*i.e.*, density of charge carriers) is not a limiting factor. However, this is not the case with carbon electrodes. Unlike metals, the charge carrier density carriers in carbon electrodes is limited and determined by the doping levels and the conductivity type (*i.e.*, semi-conductor, metal-like or metallic). This implies that the charge carriers can be distributed within the solid phase of carbon, instead of being at the surface, giving rise to “space charge” layer capacitance which being the smallest one can dominate the overall double layer capacitance. Therefore, equation (vi) is usually modified to include the space charge layer capacitance (C_{sc}) for non-metal electrodes, as given below:

$$\frac{1}{C_{DL}} = \frac{1}{C_H} + \frac{1}{C_{diff}} + \frac{1}{C_{sc}} \quad (vi)$$

Please note that the term “double layer” might or might not be an accurate description of two layers of charges (electrical charge on the electrode surface and ionic charge adsorbed on its surface), especially in RTILs. The term “double layer” has been frequently used to describe the EDL phenomena for historical and conventional reasons. The reader should keep an open mind regarding the complexity of EDL in RTILs while encountering the phrase “double layer”.

1.3.1 EDL in Room Temperature Ionic Liquids

The EDL models discussed so far were developed for dilute aqueous solutions, those in which the solvent concentration (pure water = 55.5 M) is much higher than the ion concentration ($\ll 0.1$ M). The interactions between ions are negligible due to their screening by the dielectric medium/solvent. However, for solvent-free concentrated (3-7 M) electrolytes like RTILs, the strong interionic interactions among the cations and anions begin to dominate as there is no solvent molecule to act as a dielectric separator among them. Mathematical expressions regarding the EDL structure have been proposed. However, they are too complex to be generalizable over a range of electrolytes [79,80]. While these theories pertaining to RTILs draw inspiration from the previous theories developed for high-temperature molten salts [81], some questions have been raised on their inadequacy to ably capture the complex nature of RTILs and the various inter-ionic interactions involved. The high concentration in RTILs indicate that the steric effects of finite ion size is significant.

In 2007, an article titled “Double-layer in ionic liquids: paradigm change?” by Alexei Kornyshev strongly influenced the research directions in RTILs [82]. The article concluded that the EDL in RTILs cannot be described by mean-field theories as it has been done for the aqueous

electrolytes. Secondly, it showed that how understanding the structure-property relationships in RTILS can contribute toward realization of practical RTIL-based applications. In general, these conclusions are still valid. However, the model proposed by Kornyshev has been refined four times, the latest efforts were in mid-2019.

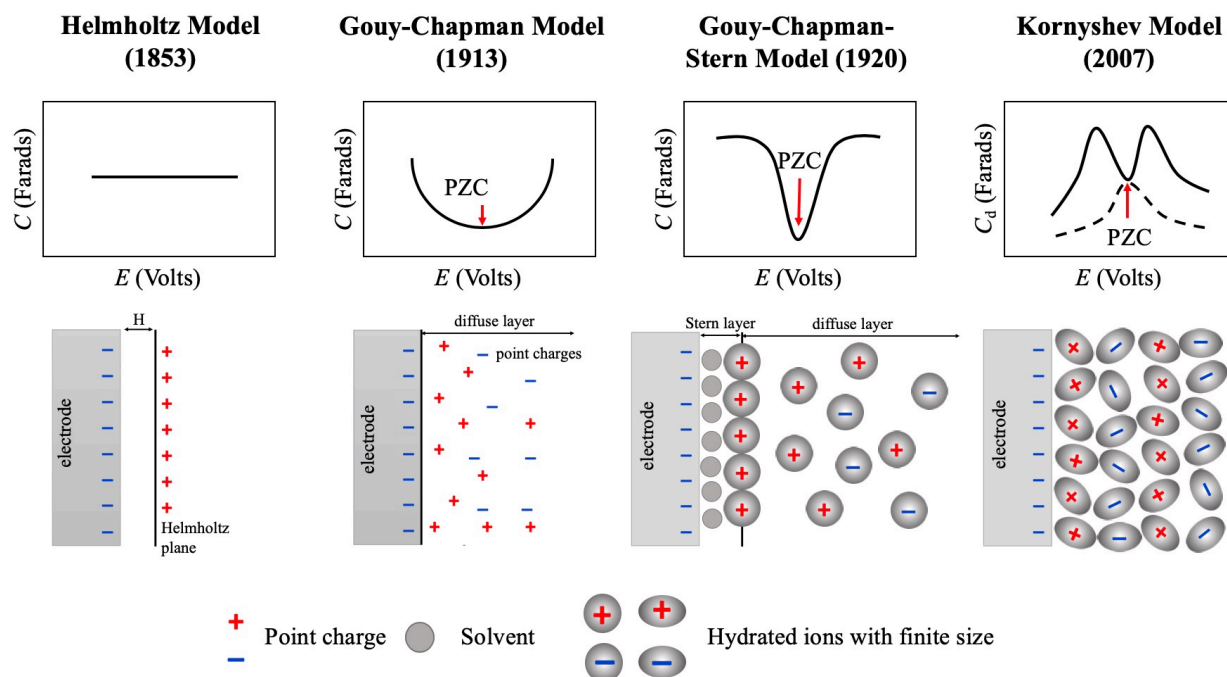


Figure 1.5. Evolution of electrical double layer model in aqueous electrolytes over time. The bottom panel shows proposed organization of ions at the interface and the top panel shows corresponding capacitance-potential profile: (A) Helmholtz model, (B) Gouy-Chapman model, (C) Gouy-Chapman-Stern model, and (D) Kornyshev model.

To experimentally measure the C-E profiles, the compact layer needs to be accurately accounted. It must be stressed that in most theories, this is an empirical parameter, which describes the closest approach of the adsorbed ions, which ultimately determines the electron-transfer kinetics [82–84]. However, the exact ratio of contribution of compact and diffuse layer is still unknown. Thus, experimental interpretations are incomplete due to inherent limitations of the theoretical models involved. There have been wide range of theories. For example, Baldelli and coworkers postulated that the EDL is one-ion thick and their model showed that the orientation of

cations adsorbed at the electrode is potential-dependent [85]. This implies that the contribution of compact layer is heightened. On the contrary, Kornyshev argued that the EDL is more than one-layer thick, and the differential capacitance is sum of the compact and diffuse layers. Shaw and Blanchard groups have shown that RTILs exhibit order on the range of 100 μm . To sum up, there is a need for new insights to understand the role of compact and diffuse layers, and the experimental results should be analyzed independently.

In 2007, Kornyshev used lattice gas model and proposed an analytical expression consisting of terms for local potential and ion distribution. A simple case of symmetric ion size was solved. A lattice saturation parameter, $\gamma = \# \text{ of occupied sites} / \# \text{ of total sites}$, was introduced. The lack of solvent was accounted by leaving empty sites in the lattice. The capacitance-potential profile given by this theory predicted a bell shape with a maximum capacitance at the point of zero charge. However, the model did not consider the short-range interactions among ions. Bazant, Storey, and Kornyshev improved this model in 2011 and developed a continuum model with crude approximations for inter-ionic interactions [84]. This model considered the volumetric effects of ions and explains simple systems well on metal electrodes. The most recent works have started considering ion asymmetry as well. Recently, in 2019, Kornyshev and coworkers revisited their model and treated the concentrated electrolyte as a dielectric medium using a non-local function approach. The model is yet to be validated with experimental data.

The models discussed so far are largely static *i.e.*, they explain the structure and magnitude of capacitance. However, the model to explain the EDL dynamics in RTILs is yet to be developed. RTILs are being used for transient electroanalytical techniques as well as the response time of sensors and charging-discharging of energy storage device can only be explained by dynamics aspects of EDL.

It is to be noted that most of these models discussed above considered metal electrodes. The electronic properties of the electrodes were not considered. However, in the last decade, the literature on the capacitance of carbon electrodes in RTILs has exploded with various C-E profiles obtained using various theoretical developments, experimental, and computational investigations. Regardless of what the C-E profile is, most of them are not symmetric because the EDL formed at the positive potentials relative to the point of zero charge is very different from that at negative potentials relative to this value. This is essentially because of the asymmetry in the size and shape of the RTIL ions. Since there is no solvent separating the ions, movement of one ion necessarily means the movement of many others in the vicinity. Due to innumerable possible combinations of component ions of RTILs and electrodes, not one model can be generalized. New continuum formulation models obscure non-specific interactions in these complex media to reduce the computational costs while maintaining the minimum fidelity. Moreover, theories are only as good as the experimental trends they can explain and therein lies the problem. The experimental data exist for so many systems and the results are far from consistent. It has been exciting and turbulent to work in this field as it is rapidly evolving with new models and their validation on a consistent basis. How well we can utilize these excellent materials is predicated on how well we understand them at the molecular level. The limited understanding and having no theoretical model to predict their electrochemical behavior is currently the major bottleneck for their implementation. Basic science to improve our understanding of such technologically-relevant electrolytes to realize RTIL-based devices is in order. This dissertation seeks to address these issues in a way that will contribute broadly to the RTILs-carbon electrode interfaces with BDD and *ta*-C:N as particular focus.

1.4 Dissertation Goals

The knowledge about the electrical double layer in aqueous electrolytes is well-established. However, there is a limited understanding of the electrical double layer capacitance of nanostructured carbons in RTILs. This dissertation is focused on addressing this knowledge gap:

- (i) How do the potential-dependent capacitances of structurally-different RTILs in contact boron-doped nanocrystalline diamond (BDD) compare? How does the capacitance in RTILs compare to the capacitance in aqueous electrolyte solutions? Do the capacitance-potential profiles for the carbon electrodes match the profiles measured for metal electrodes, like Au? Do the experimentally-determined capacitance-potential profiles agree with any models that have been put forward?
- (ii) How does the surface chemistry (hydrogen- vs. oxygen- surface termination) of boron-doped nanocrystalline diamond (BDD) affect the surface wettability and potential-dependent capacitance in different RTILs? Does surface chemistry affect capacitance in a manner similar to that observed in aqueous electrolyte solution?
- (iii) How does the potential-dependent capacitance of a new type of carbon electrode, nitrogen-incorporated tetrahedral amorphous carbon (*ta*-C:N) thin films, in RTILs compare with what is observed for conducting diamond and glassy carbon electrodes?

The overarching goal of this research is to advance the understanding of the material properties of sp^3 (BDD) and hybrid sp^3/sp^2 (nitrogen-incorporated tetrahedral amorphous carbon, *ta*-C:N) nanostructured carbon electrodes and how these properties influence their electrochemical behavior (Figure 1.6). Much of the work is focused on the microstructure, surface chemistry and electronic properties of carbon electrodes in an effort to learn how these properties affect the

voltammetric behavior and capacitance in RTILs. The research was conducted around four specific aims:

Specific Aim 1: To fully characterize the physical, chemical and electronic properties of different nanostructured carbon electrodes: boron-doped diamond (BDD) and nitrogen-incorporated tetrahedral amorphous carbon ($ta\text{-C:N}$).

Specific Aim 2: To establish common electrochemical methods to probe the EDL so as to remove the variability in data due to the method employed, data acquisition and work up, and correlate the voltammetric behavior and electrode capacitance of the nanostructured electrodes with the type and properties of RTILs

Specific Aim 3: To understand how the surface termination of BDD electrodes affects the surface wettability, voltammetric behavior and capacitance in RTILs.

Specific Aim 4: To determine how the level of nitrogen incorporation $ta\text{-C:N}$ thin films affects their physical and chemical properties and electrochemical behavior in different RTILs.

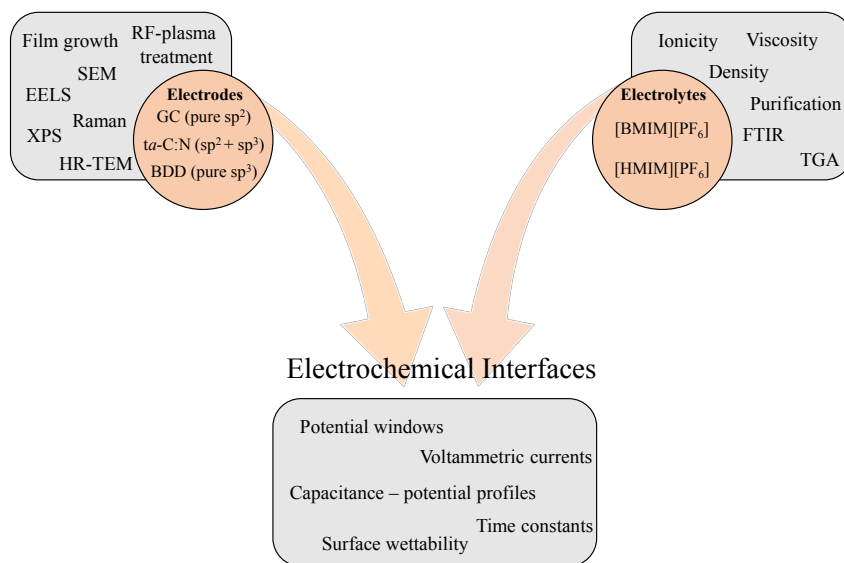


Figure 1.6. Schematic illustration of overall research presented in this dissertation. *Abbreviations* – *SEM*: Scanning Electron Microscopy, *EELS*: Electron-energy Loss Spectroscopy, *XPS*: X-ray Photoelectron Spectroscopy, *HR-TEM*: High-resolution Transmission Electron Microscopy, *FTIR*: Fourier-transform Infrared Spectroscopy, *TGA*: Thermogravimetric Analysis.

REFERENCES

REFERENCES

- [1] K. Jurkiewicz, M. Pawlyta, D. Zygałło, D. Chrobak, S. Duber, R. Wrzałik, A. Ratuszna, A. Burian, Evolution of glassy carbon under heat treatment: Correlation structure–mechanical properties, *J. Mater. Sci.* 53 (2018) 3509–3523. doi:10.1007/s10853-017-1753-7.
- [2] R.L. McCreery, Advanced carbon electrode materials for molecular electrochemistry, *Chem. Rev.* 108 (2008) 2646–2687.
- [3] Structure of Glassy Carbon, *Nature*. 231 (1971) 176–178. doi:10.1038/231176a0.
- [4] W.M. Douglas, Carbon and Graphite Science, *Annu. Rev. Mater. Sci.* 3 (1973) 195–231. doi:10.1146/annurev.ms.03.080173.001211.
- [5] W.E. Van der Linden, J.W. Dieker, Glassy carbon as electrode material in electro- analytical chemistry, *Anal. Chim. Acta.* 119 (1980) 1–24. doi:10.1016/S0003-2670(00)00025-8.
- [6] C.L. Burket, R. Rajagopalan, A.P. Marencic, K. Dronvajjala, H.C. Foley, Genesis of porosity in polyfurfuryl alcohol derived nanoporous carbon, *Carbon N. Y.* 44 (2006) 2957–2963. doi:10.1016/j.carbon.2006.05.029.
- [7] É.T.G. Cavaleiro, C.M.A. Brett, A.M. Oliveira-Brett, O. Fatibello-Filho, Bioelectroanalysis of pharmaceutical compounds, *Bioanal. Rev.* 4 (2012) 31–53. doi:10.1007/s12566-012-0027-8.
- [8] P.J.F. Harris, New perspectives on the structure of graphitic carbons, *Crit. Rev. Solid State Mater. Sci.* 30 (2005) 235–253. doi:10.1080/10408430500406265.
- [9] F.J. Zittel, H. E., Miller, A Glassy-Carbon Electrode for Voltammetry, *Anal. Chem.* 37 (1965) 200–203. doi:10.1021/ac60221a006.
- [10] H.S. Yamada, S., Some Physical Properties of Glassy Carbon, *Nature*. 139 (1962) 261–262. doi:10.1179/mtlr.1963.8.1.277.
- [11] O.E.P. Robertson, J., Electronic and atomic structure of amorphous carbon, *Phys. Rev. B - Condens. Matter Mater. Phys.* 35 (1987) 2946–2957. doi:https://doi.org/10.1103/PhysRevB.35.2946.
- [12] M.W. Haenni, Control of Electron Transfer Kinetics at Boron-doped Diamond Electrodes by Specific Surface Modification, *2732 (2003)* 3958–3965.

- [13] C.J. Hoogvliet, J. C., Van Den Beld, C.M.B., Van Den Beld, Influence of Polishing and of Electrochemical Pretreatment on the Performance of Glassy-Carbon Electrodes in Electrochemical Detection, *J. Electro. 201* (1986) 11–21.
- [14] R.C. Engstrom, V.A. Strasser, Characterization of Electrochemically Pretreated Glassy Carbon Electrodes, *Anal. Chem.* 56 (1984) 136–141. doi:10.1021/ac00266a005.
- [15] D.T. Fagan, I.F. Hu, T. Kuwana, Vacuum Heat Treatment for Activation of Glassy Carbon Electrodes, *Anal. Chem.* 57 (1985) 2759–2763. doi:10.1021/ac00291a006.
- [16] S. Ranganathan, T.C. Kuo, R.L. McCreery, Facile preparation of active glassy carbon electrodes with activated carbon and organic solvents, *Anal. Chem.* 71 (1999) 3574–3580. doi:10.1021/ac981386n.
- [17] M. Poon, R.L. McCreery, In Situ Laser Activation of Glassy Carbon Electrodes, *Anal. Chem.* 58 (1986) 2745–2750. doi:10.1021/ac00126a036.
- [18] R.H. Baker, Dennis F., Bragg, The Electrical Conductivity And Hall Effect of Glassy Carbon, *J. Non-Crystalline.* 58 (1983) 57–69.
- [19] J.H.T. Luong, B. Male, J.D. Glennon, K.B. Male, J.D. Glennon, Boron-doped diamond electrode: synthesis, characterization, functionalization and analytical applications., *Analyst.* 134 (2009) 1965–79. doi:10.1039/b910206j.
- [20] H. Kawai, Hydrogen-terminated diamond surfaces and interfaces, *Surf. Sci. Rep.* 26 (1996) 205–259. doi:10.1016/S0167-5729(97)80002-7.
- [21] J.C. ANGUS, C.C. HAYMAN, Low-Pressure, Metastable Growth of Diamond and “Diamondlike” Phases, *Science* (80-.). 241 (1988) 913 LP – 921. doi:10.1126/science.241.4868.913.
- [22] B. Pau, U.K. Diamond, *Diamond thin Films : a 21st-century material*, (2000).
- [23] G.M. Swain, R. Ramesham, The Electrochemical Activity of Boron-Doped polycrystalline Diamond Thin Film Electrodes, *Anal. Chem.* 65 (1993) 345–351. doi:10.1021/ac00052a007.
- [24] C.J. Power A.C., Gorey B., Chandra S., Carbon nanomaterials and their application to electrochemical sensors : A review, *Nanotechnol. Rev.* 7 (2018) 19–41. doi:10.1515/ntrev-2017-0160.
- [25] R.J. Bowling, R.T. Packard, R.L. McCreery, Activation of Highly Ordered Pyrolytic Graphite for Heterogeneous Electron Transfer: Relationship between Electrochemical Performance and Carbon Microstructure, *J. Am. Chem. Soc.* 111 (1989) 1217–1223. doi:10.1021/ja00186a008.

- [26] R.J. Rice, R.L. McCreery, Quantitative Relationship between Electron Transfer Rate and Surface Microstructure of Laser-Modified Graphite Electrodes, *Anal. Chem.* 61 (1989) 1637–1641. doi:10.1021/ac00190a010.
- [27] R.J. Rice, N.M. Pontikos, R.L. McCreery, Quantitative Correlations of Heterogeneous Electron-Transfer Kinetics with Surface Properties of Glassy Carbon Electrodes, *J. Am. Chem. Soc.* 112 (1990) 4617–4622. doi:10.1021/ja00168a001.
- [28] K.R. Kneten, R.L. McCreery, Effects of Redox System Structure on Electron-Transfer Kinetics at Ordered Graphite and Glassy Carbon Electrodes, *Anal. Chem.* 64 (1992) 2518–2524. doi:10.1021/ac00045a011.
- [29] P. Chen, M.A. Fryling, R.L. McCreery, Electron Transfer Kinetics at Modified Carbon Electrode Surfaces: The Role of Specific Surface Site, *Anal. Chem.* 67 (1995) 3115–3122. doi:10.1021/ac00114a004.
- [30] A. Kraft, Doped Diamond: A Compact Review on a New, Versatile Electrode Material - Open Access Library, *Int. J. Electrochem. Sci.* 2 (2007) 355–385. doi:10.1021/jo026183k.
- [31] J. V Macpherson, A practical guide to using boron doped diamond in electrochemical research., *Phys. Chem. Chem. Phys.* 17 (2015) 2935–49. doi:10.1039/c4cp04022h.
- [32] Y. Einaga, J.S. Foord, G.M. Swain, Diamond electrodes: Diversity and maturity, *MRS Bull.* 39 (2014) 525–532. doi:10.1557/mrs.2014.94.
- [33] S. Wang, V.M. Swope, J.E. Butler, T. Feygelson, G.M. Swain, The structural and electrochemical properties of boron-doped nanocrystalline diamond thin-film electrodes grown from Ar-rich and H₂-rich source gases, *Diam. Relat. Mater.* 18 (2009) 669–677. doi:10.1016/j.diamond.2008.11.033.
- [34] M.C. Granger, J. Xu, J.W. Strojek, G.M. Swain, Polycrystalline diamond electrodes: basic properties and applications as amperometric detectors in flow injections analysis and liquid chromatography, *Anal. Chim. Acta.* 397 (1999) 145–161.
- [35] J. Xu, M.C. Granger, Q. Chen, J.W. Strojek, T.E. Lister, G.M. Swain, Boron-Doped Diamond Thin-Film Electrodes, *Anal. Chem.* 69 (2011) 591A-597A. doi:10.1021/ac971791z.
- [36] S.J. Cobb, Z.J. Ayres, J. V. Macpherson, Boron Doped Diamond: A Designer Electrode Material for the Twenty-First Century, *Annu. Rev. Anal. Chem.* 11 (2018) 463–484. doi:10.1146/annurev-anchem-061417-010107.
- [37] M.C. Granger, The Influence of Surface Interactions on the Reversibility of Ferri/Ferrocyanide at Boron-Doped Diamond Thin-Film Electrodes, *J. Electrochem. Soc.* 146 (1999) 4551. doi:10.1149/1.1392673.

- [38] Y. V. Pleskov, M.D. Krotova, V. V. Elkin, E.A. Ekimov, Electrochemical Behaviour of Boron-doped Diamond Compacts - A New Electrode Material, *Electrochim. Acta.* 201 (2016) 268–273. doi:10.1016/j.electacta.2015.09.075.
- [39] J. Foord, J.P. Hu, Electrochemical oxidation and reduction processes at diamond electrodes of varying phase purity, *Phys. Status Solidi Appl. Mater. Sci.* 203 (2006) 3121–3127. doi:10.1002/pssa.200671117.
- [40] J. Ristein, Structural and electronic properties of diamond surfaces, Elsevier, 2004. doi:10.1016/S0080-8784(04)80014-0.
- [41] J.P. Lagrange, A. Deneuve, E. Gheeraert, Activation energy in low compensated homoepitaxial boron-doped diamond films, *Diam. Relat. Mater.* 7 (1998) 1390–1393. doi:10.1016/S0925-9635(98)00225-8.
- [42] H. Ye, N. Tumilty, M. Bevilacqua, S. Curat, M. Nesladek, B. Bazin, P. Bergonzo, R.B. Jackman, Electronic properties of homoepitaxial (111) highly boron-doped diamond films, *J. Appl. Phys.* 103 (2008). doi:10.1063/1.2837114.
- [43] F.B. Liu, B. Jing, Y. Cui, J.J. Di, M. Qu, Voltammetric and impedance behaviours of surface-treated nano-crystalline diamond film electrodes, *AIP Adv.* 5 (2015). doi:10.1063/1.4903731.
- [44] R. Boukherroub, X. Wallart, S. Szunerits, B. Marcus, P. Bouvier, M. Mermoux, Photochemical oxidation of hydrogenated boron-doped diamond surfaces, *Electrochem. Commun.* 7 (2005) 937–940. doi:10.1016/j.elecom.2005.05.010.
- [45] P.E. Pehrsson, J.P. Long, M.J. Marchywka, J.E. Butler, Electrochemically induced surface chemistry and negative electron affinity on diamond (100), *Appl. Phys. Lett.* 67 (1995) 3414. doi:10.1063/1.115264.
- [46] J. Shirafuji, T. Sugino, Electrical properties of diamond surfaces, *Diam. Relat. Mater.* 5 (1996) 706–713. doi:10.1016/0925-9635(95)00415-7.
- [47] T.N. Rao, Band-Edge Movements of Semiconducting Diamond in Aqueous Electrolyte Induced by Anodic Surface Treatment, *J. Electrochem. Soc.* 146 (1999) 680. doi:10.1149/1.1391662.
- [48] V. Seshan, D. Ullien, A. Castellanos-Gomez, S. Sachdeva, D.H.K. Murthy, T.J. Savenije, H.A. Ahmad, T.S. Nunney, S.D. Janssens, K. Haenen, M. Nesládek, H.S.J. Van Der Zant, E.J.R. Sudhölter, L.C.P.M. De Smet, Hydrogen termination of CVD diamond films by high-temperature annealing at atmospheric pressure, *J. Chem. Phys.* 138 (2013). doi:10.1063/1.4810866.
- [49] R.K. V. Landstrass M. I., Resistivity of chemical vapor deposited diamond films, *Appl. Phys. Lett.* 55 (1989) 975–977. doi:10.1063/1.101694.

- [50] R.K. V. Landstrass, M. I., Hydrogen passivation of electrically active defects in diamond, *Appl. Phys. Lett.* 55 (1989) 1391–1393. doi:10.1063/1.101604.
- [51] F. Maier, M. Riedel, B. Mantel, J. Ristein, L. Ley, Origin of surface conductivity in diamond, *Phys. Rev. Lett.* 85 (2000) 3472–5. <http://www.ncbi.nlm.nih.gov/pubmed/11690524>.
- [52] J. Ristein, Diamond surfaces: Familiar and amazing, *Appl. Phys. A Mater. Sci. Process.* 82 (2006) 377–384. doi:10.1007/s00339-005-3363-5.
- [53] D.E. Himpfel, F. J., Knapp, J. A., VanVechten, J. A., Eastman, Quantum Photoyield of Diamond (111)- A Stable Negative-affinity Emitter, *Phys. Rev. B - Condens. Matter Mater. Phys.* 20 (1979) 624–627. doi:<https://doi.org/10.1103/PhysRevB.20.624>.
- [54] F. Maier, J. Ristein, L. Ley, Electron affinity of plasma-hydrogenated and chemically oxidized diamond (100) surfaces, *Phys. Rev. B - Condens. Matter Mater. Phys.* 64 (2001) 1–7. doi:10.1103/PhysRevB.64.165411.
- [55] S. Alehashem, F. Chambers, J.W. Strojek, G.M. Swain, R. Ramesham, Cyclic Voltammetric Studies of Charge Transfer Reactions at Highly Boron-Doped Polycrystalline Diamond Thin-Film Electrodes, *Anal. Chem.* 67 (1995) 2812–2821. doi:10.1021/ac00113a014.
- [56] P. Actis, A. Denoyelle, R. Boukherroub, S. Szunerits, Influence of the surface termination on the electrochemical properties of boron-doped diamond (BDD) interfaces, *Electrochem. Commun.* 10 (2008) 402–406. doi:10.1016/j.elecom.2007.12.032.
- [57] L.J. Janssen, G., Enkevort, W. J. P. van, Vollenberg, W., Giling, Characterization of single-crystal diamond grown by chemical vapour deposition processes, *Diam. Relat. Mater.* 1 (1992) 789–800. doi:10.1016/0925-9635(92)90102-T.
- [58] B. V. Spitsyn, L.L. Bouilov, B. V. Derjaguin, Vapor growth of diamond on diamond and other surfaces, *J. Cryst. Growth.* 52 (1981) 219–226. doi:10.1016/0022-0248(81)90197-4.
- [59] S.L. Clewes, M.E. Newton, P.R. Unwin, J. V. Macpherson, N.R. Wilson, Impact of grain-dependent boron uptake on the electrochemical and electrical properties of polycrystalline boron doped diamond electrodes, *J. Phys. Chem. B.* 110 (2006) 5639–5646. doi:10.1021/jp0547616.
- [60] S. Wang, G.M. Swain, Spatially heterogeneous electrical and electrochemical properties of hydrogen-terminated boron-doped nanocrystalline diamond thin film deposited from an argon-rich CH₄/H₂/Ar/B₂H₆ source gas mixture, *J. Phys. Chem. C.* 111 (2007) 3986–3995. doi:10.1021/jp0669557.
- [61] A.E. Fischer, G.M. Swain, Preparation and Characterization of Boron-Doped Diamond Powder, *J. Electrochem. Soc.* 152 (2005) B369. doi:10.1149/1.1984367.

- [62] D.Y. Kim, B. Merzougui, G.M. Swain, Preparation and characterization of glassy carbon powder modified with a thin layer of boron-doped ultrananocrystalline diamond (B-UNCD), *Chem. Mater.* 21 (2009) 2705–2713. doi:10.1021/cm803310k.
- [63] T. Torimoto, T. Tsuda, K. Okazaki, S. Kuwabata, New Frontiers in Materials Science Opened by Ionic Liquids, *Adv. Mater.* 22 (2010) 1196–1221. doi:10.1002/adma.200902184.
- [64] M. Armand, F. Endres, D.R. MacFarlane, H. Ohno, B. Scrosati, Ionic-liquid materials for the electrochemical challenges of the future, *Nat. Mater.* 8 (2009) 621–629. doi:10.1038/nmat2448.
- [65] R. Patel, M. Kumari, A.B. Khan, Recent advances in the applications of ionic liquids in protein stability and activity: A review, *Appl. Biochem. Biotechnol.* 172 (2014) 3701–3720. doi:10.1007/s12010-014-0813-6.
- [66] D. Xiao, L.G. Hines Jr., R.A. Bartsch, E.L. Quitevis, O. Russina, A. Triolo, Effect of symmetry of the cation and alkyl chain length on the structure and intermolecular dynamics of 1,3-dialkylimidazolium bis(trifluoromethanesulfonyl)imide ionic liquids, *Abstr. Pap. Am. Chem. Soc.* 237 (2009) 6426–6433.
- [67] H. Tokuda, K. Hayamizu, K. Ishii, M.A.B.H. Susan, M. Watanabe, Physicochemical properties and structures of room temperature ionic liquids. 2. variation of alkyl chain length in imidazolium cation, *J. Phys. Chem. B.* 109 (2005) 6103–6110. doi:10.1021/jp044626d.
- [68] K.R. Seddon, A. Stark, M.-J. Torres, Viscosity and Density of 1-Alkyl-3-methylimidazolium Ionic Liquids, (2009) 34–49. doi:10.1021/bk-2002-0819.ch004.
- [69] M. Galiński, A. Lewandowski, I. Stepniak, Ionic liquids as electrolytes, *Electrochim. Acta.* 51 (2006) 5567–5580. doi:10.1016/j.electacta.2006.03.016.
- [70] P. Hapiot, C. Lagrost, Electrochemical reactivity in room-temperature ionic liquids, *Chem. Rev.* 108 (2008) 2238–2264. doi:10.1021/cr0680686.
- [71] Z. Wang, M. Guo, X. Mu, S. Sen, T. Insley, A.J. Mason, P. Král, X. Zeng, Highly Sensitive Capacitive Gas Sensing at Ionic Liquid-Electrode Interfaces, *Anal. Chem.* 88 (2016) 1959–1964. doi:10.1021/acs.analchem.5b04677.
- [72] X. Mu, Z. Wang, X. Zeng, A.J. Mason, A robust flexible electrochemical gas sensor using room temperature ionic liquid, *IEEE Sens. J.* 13 (2013) 3976–3981. doi:10.1109/JSEN.2013.2262932.
- [73] M. Gouy, Sur la constitution de la charge électrique à la surface d'un électrolyte, *J. Phys. Théorique Appliquée.* 9 (1910) 457–468. doi:10.1051/jphysap:019100090045700.

- [74] O. Stern, Zur Theorie Der Elektrolytischen Doppelschicht, Zeitschrift Für Elektrochemie Und Angew. Phys. Chemie. 30 (1924) 508–516. doi:10.1002/bbpc.192400182.
- [75] H. von Helmholtz, Ueber einige Gesetze der Vertheilung elektrischer Ströme in körperlichen Leitern mit Anwendung auf thierisch-elektrischen Versuche, Ann. Phys. 165 (1853) 211–233.
- [76] D.L. Chapman, LI. A contribution to the theory of electrocapillarity , London, Edinburgh, Dublin Philos. Mag. J. Sci. 25 (2009) 475–481. doi:10.1080/14786440408634187.
- [77] D.C. Grahame, The electrical double layer and the theory of electrocapillarity, Chem. Rev. 41 (1947) 441–501. doi:10.1021/cr60130a002.
- [78] H. Krienke, Modern Aspects of Electrochemistry, No. 31, 2011. doi:10.1524/zpch.1999.213.part_2.216.
- [79] L. Onsager, Theories of concentrated electrolytes, Chem. Rev. 13 (1933) 73–89. doi:10.1021/cr60044a006.
- [80] M. V. Fedorov, A.A. Kornyshev, Ionic liquids at electrified interfaces, Chem. Rev. 114 (2014) 2978–3036. doi:10.1021/cr400374x.
- [81] M. V Fedorov, A.A. Kornyshev, Towards understanding the structure and capacitance of electrical double layer in ionic liquids, Electrochim. Acta. 53 (2008) 6740–6835.
- [82] A.A. Kornyshev, Double-Layer in Ionic Liquids: Paradigm Change?, J. Phys. Chem. B. 111 (2007) 5545–5557. doi:10.1021/jp067857o.
- [83] D. Henderson, S. Lamperski, Z. Jin, J. Wu, Density Functional Study of the Electric Double Layer Formed by a High Density Electrolyte, J. Phys. Chem. B. 115 (2011) 12911–12914. doi:10.1021/jp2078105.
- [84] M.Z. Bazant, B.D. Storey, A.A. Kornyshev, Double layer in ionic liquids: Overscreening versus crowding, Phys. Rev. Lett. 106 (2011) 6–9. doi:10.1103/PhysRevLett.106.046102.
- [85] S. Baldelli, Surface structure at the ionic liquid-electrified metal interface, Acc. Chem. Res. 41 (2008) 421–431. doi:10.1021/ar700185h.
- [86] D. Debajyoti, Nanocrystalline Diamond: A high-Impact Carbon Nanomaterial for Multifunctional Applications Including as Nanofiller in Biopolymeric Matrices, Elsevier Inc., 2017. doi:10.1201/9781315371795.

Chapter 2

Experimental and Methods

The materials and methods described in this chapter gives a general overview of the sample and electrode preparation, and operation of and data acquisition on different instruments employed throughout the study presented in this dissertation. For the specific details, please refer to the description provided in Chapters 3 through 5.

2.1 Materials

2.1.1 Room Temperature Ionic Liquids (RTILs)

The ultrapure grade RTILs, 1-butyl-3-methylimidazolium hexafluorophosphate [BMIM][PF₆] (IL-0011-UP) and 1-hexyl-3-methylimidazolium hexafluorophosphate [HMIM][PF₆] (IL-0018-UP), were procured from a commercial source, IoLiTec (Ionic Liquids Technologies GmbH), Tuscaloosa, AL, $\geq 99.5\%$ purity, water content below 100 ppm). Unless otherwise stated, all RTIL samples were mixed with activated charcoal (Sigma-Aldrich) and stirred vigorously using a magnetic plate for two days. The samples were then left undisturbed for two weeks to allow the charcoal powder to settle at the bottom of a 20-mL glass vial. The RTIL was filtered using a 0.2 μm Teflon syringe filter (Whatman) directly into the electrochemical cell to avoid any possible contamination during the transfer. Approximately 0.5 mL of RTIL was used for each experiment. Prior to any electrochemical test, the RTIL sample in the electrochemical cell was heated at 70 °C for 60 minutes while purging with ultrahigh purity Ar (99.999%) at a high

flow rate. The Ar gas was passed through drierite desiccants twice before introducing into the dry-N₂ filled glove box (Coy Laboratories). The water content in the RTIL was assessed qualitatively by cyclic voltammetry (background current and potential window) and FTIR, and quantitatively by thermogravimetric analysis (TGA). To remove any dissolved oxygen or carbon dioxide, the RTIL was sparged with ultrapure Ar at least 15 minutes before the experiment, and a blanket of Ar was maintained over the RTIL during the experiments. All glassware used was washed using Alconox/ultrapure water solution and then triply rinsed sequentially with deionized water, isopropanol, acetone, and ultrapure water, and finally dried in an oven at 150 °C for at least 12 h before use. All preparation and the electrochemical measurements were done in a dry N₂ purged glove box (Coy Laboratories, Grass Lake, MI). The relative humidity in the glove box was maintained at 0.0 % or below the detection limit (0.1%) of a digital hygrometer.

2.1.2 Aqueous Electrolytes

Ultrapure grade sulfuric acid (99.999%), CAS- 339741, was obtained from Sigma-Aldrich and diluted to 0.5 M using deionized water. The ultrapure water was obtained from a Barnstead E-pure System (Thermo Scientific, USA) filtered through a Milli-Q deionized water purification system with a resistivity of >17 MΩ-cm.

2.2 Electrode Preparation

2.2.1 Glassy Carbon Electrodes

The glassy carbon (GC-20, Tokai Ltd.) electrode was sequentially polished with 1.0, 0.3 and 0.05 μm diameter Micropolish II alumina powder (Buehler) on a micro-cloth PSA (Buehler) pad for approximately ten minutes at each step. The alumina powder was mixed with deionized water to form a slurry. The polishing was performed manually in an 8-digit shape while applying slight pressure on the electrode [1]. The electrode was rinsed with deionized water to remove the alumina powder debris and sonicated in isopropanol for ten minutes after each polishing step. Finally, the electrode was rinsed with copious amounts of deionized water and ultrasonically cleaned for 20 minutes to remove any polishing debris. The electrodes were used immediately for the electrochemical measurements.

2.2.2 Boron-Doped Nanocrystalline Diamond (BDD) Thin Film Electrodes

The boron-doped nanocrystalline diamond (BDD) thin-films were grown on a p-Si (111) substrate (Virginia Semiconductor, Inc. Fredricksburg, VA, $\sim 0.001 \Omega\text{-cm}$) by microwave-assisted chemical vapor deposition (CVD) using a commercial 1.5 kW reactor (Seki Technotron) [2]. The silicon substrate was seeded ultrasonically using nanodiamond particles as Opal seeds suspension (Adamas Nanotechnologies Inc., Raleigh, NC) for 30 minutes in a glass beaker. This suspension contains aggregates ($\sim 30 \text{ nm}$ in size) of detonation diamond particles in dimethyl sulfoxide (DMSO). The seeded substrate was then rinsed 3x with ultrapure water followed by wick-drying with a Kimwipe and drying with a stream of N_2 before being placed in the CVD reactor for overnight pump-down. The BDD film was grown using methane diluted in hydrogen ($\text{C/H} = 1\%$,

v/v) at a total gas flow rate of 200 sccm (standard cubic centimeter per minute), a system pressure of 35 Torr, an estimated substrate temperature of 825 °C, and a growth time of 5-6 h. Boron doping was accomplished by adding 0.1% (v/v) diborane in hydrogen to the source gas, producing a gas-phase concentration of 10 ppm. After deposition, the methane and diborane flows were stopped, and the coated substrate was cooled under a hydrogen plasma for 30 min by slowly reducing the power and pressure down to 150 W and 10 Torr. This post-growth cooling step was critical to minimize the formation of sp²-bonded carbon at the surface that would result from the desorption of surface hydrogen ($T > \sim 450$ °C) and reconstruction of the surface carbon atoms if the plasma were extinguished at the growth temperature. The cooling step in atomic hydrogen is also critical for maintaining a hydrogen-terminated surface [3]. The doping level was estimated to be in the low 10^{21} cm⁻³ range based on Raman spectroscopic and Hall effect measurement data of other films deposited under similar conditions [4]. The film thickness was estimated to be 2 to 4 μm (growth time 6 h) by the change in weight of the substrate after film deposition and cross-sectional SEM micrographs. The electrical resistivity was generally ≤ 0.01 Ω-cm.

2.2.3 Nitrogen-Incorporated Tetrahedral Amorphous Carbon (ta-C:N) Thin Film Electrodes

ta-C:N films were grown on a boron-doped Si (111) (Virginia Semiconductor, Fredericksburg, VA; 10^{-3} Ω-cm) using a laser-arc physical vapor deposition system at the Fraunhofer Center for Coatings and Diamond Technologies, MSU. The deposition method is based on laser-controlled, high-current cathodic vacuum arc deposition [2,5–8]. A pulsed-laser beam was rostered across a rotating high-purity graphite target that serves as the cathode. Each laser pulse generates small localized plasma that delivers free charge carriers for the arc discharge. The arc

discharge lasts only 125 μs before the laser triggers a new, staggered plasma across the graphite cathode. The arc evaporation is associated with the emission of microparticles of carbon originating from the graphite drum (*i.e.*, cathode surface) [8], and consists of highly ionized C atoms and small ionized carbon atom clusters that are accelerated toward the substrate (grounded mode). This process produces hard (30-60 GPa) and dense *ta*-C films. The substrate-target distance was approximately 30 cm. The substrates were rotated during the growth to obtain uniform film deposition. The nitrogen-incorporated films were deposited in the presence of N_2 gas at a flow rate of 10, 30 and 50 sccm, a pulse rate of 350 Hz and a peak arc current of > 100 A. Increased levels of nitrogen in the chamber lead to increased nitrogen incorporation into the film and increased electrical conductivity [9–11]. The substrate temperature during the deposition was below 100°C . The film growth rate was 2-3 $\mu\text{m/h}$.

2.2.4 Polycrystalline Gold Thin Film Electrodes

The planar gold thin-film electrode (1000 \AA thick film, E-gun evaporation) was deposited on heavily doped p-type Si (100) (LGA Thin Films, Inc., Santa Clara, CA). Any as-grown Au-film was pretreated prior to use to oxidatively remove organic surface contaminants by a 5-min immersion in a mild piranha solution of $0.5\text{ mol L}^{-1}\text{ H}_2\text{SO}_4$ and 25 wt. % hydrogen peroxide. *This cleaning solution is a strong oxidant and corrosive. It is dangerous and potentially unstable. It should be used with proper safety precautions.* The film was then thoroughly rinsed with deionized water. This was followed by mounting the film at the bottom of an electrochemical cell with the solution contained by a VitonTM. In the cell, the Au surface was pretreated by potential cycling in $0.5\text{ mol L}^{-1}\text{ H}_2\text{SO}_4$ between -0.3 to 1.2 V (vs. Ag/AgCl) at 0.05 Vs^{-1} [12]. The cycling was carried out until an unchanging voltammogram was observed (~ 40 cycles). A second pretreatment then

followed involving potential cycling in 0.5 mol L⁻¹ KOH from -0.2 to 1.2 V (vs. Ag/AgCl) at a scan rate of 0.05 V s⁻¹ (~10 cycles). These electrochemical pretreatments were followed by copious rinsing of the electrochemical cell and the mounted electrode with deionized water. The electrode surface was then immersed in ultrapure (distilled and stored over activated carbon) isopropanol for 20 min as a final cleaning step.

As a final cleaning step, all electrodes (GC, BDD, *ta*-C:N, Au) were soaked in ultrapure isopropanol for 20 minutes. This step was usually done with the working electrode mounted onto the electrochemical cell. Isopropanol was first triply distilled and stored over activated carbon. This step removes any organic contaminant present on the surface of electrode. Post IPA wash, the electrodes were fully dried under a stream of N₂ gas.

2.2.5 Surface Modification of BDD Electrodes

Hydrogen microwave plasma treatment was used to produce a low-oxygen BDD surface. This was accomplished by microwave plasma treatment using a 200 sccm flow of hydrogen for a total of 30 min at 800 W. The films were cooled to below 400 °C by slowly reducing the pressure and power over the last 10 min of the treatment. These films are referred to as “H-BDD” in the text. A radio frequency (RF) plasma generator (PDC-32G, Harrick Scientific) operating at 18 W was used to produce moderate- and high-oxygen BDD surfaces by exposing them to Ar and O₂ plasmas, respectively. The films were placed in the center of the pyrex reaction chamber that was connected to an ultrapure gas feed (Ar or O₂). The samples were plasma treated under static conditions using a pressure of 300 mTorr for 12 minutes. This was achieved by evacuating the

chamber and then filling the closed chamber 3x to pressure with the desired gas. These films with moderate and low surface oxygen coverage are referred to as “Ar-BDD” and “O-BDD” in the text.

2.3 Instrumentation

2.3.1 Visible Raman Spectroscopy

Visible Raman spectroscopy was performed using a Renishaw *in Via Reflex* Confocal Raman microscope equipped with a Nd:YAG laser source. The excitation wavelength was 532 nm. Spectra were acquired with *Wire* Interface software using a laser power of 0.4 W at the sample and an 1800 lines mm⁻¹ grating. Spectra were acquired at single spots. The typical integration time per spectrum was 10 s. The Raman spectrometer was calibrated with a Type IIa single-crystal diamond standard (phonon line at 1332⁻¹). The Raman spectra of *ta*-C:N_x films were fitted using Voigt (Gaussian/Lorentzian, 0.8) function peak.

2.3.2 X-ray Diffraction (XRD) Spectroscopy

The crystallinity of the BDD films was probed using Rigaku Smartlabs diffractometer. X-rays at 1.540 Å were generated from a rotating 9kV Cu anode source. The spectra were recorded at a grazing incidence angle of 0.5° in thin-film parallel beam geometry.

2.3.3 X-ray Photoelectron Spectroscopy (XPS)

The chemical composition of the BDD films in the near-surface region was determined using X-ray photoelectron spectroscopy (XPS). XPS spectra were recorded using a Perkin-Elmer

PHI 5400 ESCA system with a high-intensity monochromatic X-ray source (Al K α). Samples were analyzed at a base pressure of 10^{-9} Torr with a take-off angle of 45 ° using a pass energy of 29.35 eV. The X-ray power was 350 W, and scans were acquired over a 250 μm^2 area. The instrument was calibrated using the C1s peak for HOPG (highly ordered pyrolytic graphite) at 284.5 eV as an internal reference. The atomic percentage of each element was calculated from the peak areas divided by relative sensitivity factors for the PHI 5400 system. Deconvolution of core level spectra was accomplished using MultiPAK v.8.2.0. software with the instrument. The spectra were fit to a Gaussian-Lorentzian (G/L = 0.8) peak shape after Shirley background correction to calculate the atomic ratios of carbon and oxygen.

2.3.4 Scanning Electron Microscopy (SEM)

The morphology of the BDD films before and after the different plasma treatments was studied using scanning electron microscopy (JEOL 7500F, JEOL Ltd. Tokyo, Japan, Center for Advanced Microscopy, MSU). The SEM micrographs (secondary electrons) were collected at 10,000x using a 5.0 kV as accelerating voltage at a working distance of 4.5 mm.

2.3.5 Contact Angle Measurements

The wettability of the chemically-modified BDD electrodes was investigated by static contact angle measurements using a KRÜSS GmbH DSA 100 Drop Shape Analyzer. The contact angles were recorded with ultrapure water and the purified RTILs. A 1 μL droplet of purified RTIL or water was placed on the BDD film that was positioned atop the glass pedestal using a 15 G Hamilton syringe. A photograph of the droplet-electrode surface was captured using a digital

camera at about ~12 s after drop placement. The photographs were analyzed using the instrument software. The reported contact angle represents an average of five measurements across each diamond film – at the center and the four corners of each film. The reported angle is also an average of angles at the right- and left-hand side of the photograph. All measurements were made with the instrument in a dry room with a relative humidity ≤ 0.1 %.

2.3.6 Thermogravimetric Analysis (TGA)

Thermogravimetric analysis (TGA Q500, TA Instruments) was performed under a dry N₂ atmosphere to estimate the water content. The analysis involved placing a purified drop of the RTIL into the instrument's Pt sample boat that was first dried and cleaned by heating in an acetylene gas flame. The RTIL sample was then heated from room temperature to 300 °C at 10 °C min⁻¹. A dry N₂ gas blanket was maintained over the RTIL during the entire temperature ramp to minimize water uptake from the atmosphere. To consider buoyancy effects caused by the change in the density of dry N₂ as the temperature increased, a blank was run with the empty Pt sample boat. The weight-change vs. temperature data for the RTILs were all corrected using this blank.

2.3.7 Fourier Transform Infrared (FTIR) Spectroscopy

The impurity and water content of the RTILs were assessed using Fourier transform infrared spectroscopy (FTIR) in the transmission mode (Mattson Galaxy, Series 3000). A 500 μ L drop of the purified RTIL was placed between two potassium bromide salt plates in the N₂-filled vinyl glove box. The assembly was then quickly transferred through the laboratory atmosphere to the N₂-purged sample compartment of the FTIR. One hundred scans were co-added at a spectral

resolution of 4 cm^{-1} and background-subtracted. The potassium bromide disks (International Crystal Laboratories, Garfield, NJ) were used to collect the background spectra.

2.3.8 High-Resolution Transmission Electron Microscopy (HR-TEM)

HRTEM images were collected using a field-emission microscope (JEOL-2200FS, Tokyo, Japan) operating at 200 kV. A Gatan 1024 x 1024 UltraScan 4000 CCD camera was used to capture digital HR-TEM images.

2.3.9 Electron Energy Loss Spectroscopy (EELS)

Small-spot EELS measurements were made in scanning transmission electron microscopy mode (STEM). A Cu grid was used as a substrate. The *ta*-C:N_x films were grown directly on the Formavar (carbon-coated Cu grid), Ted-Pella#01883-F. The grid had holes of $\sim 1\mu\text{m}$ with of $\sim 4\mu\text{m}$ spacing in between the holes (Figure 2.1). The thin sections of *ta*-C:N film hanging freely in between the voids were used to collect the HR-TEM images.

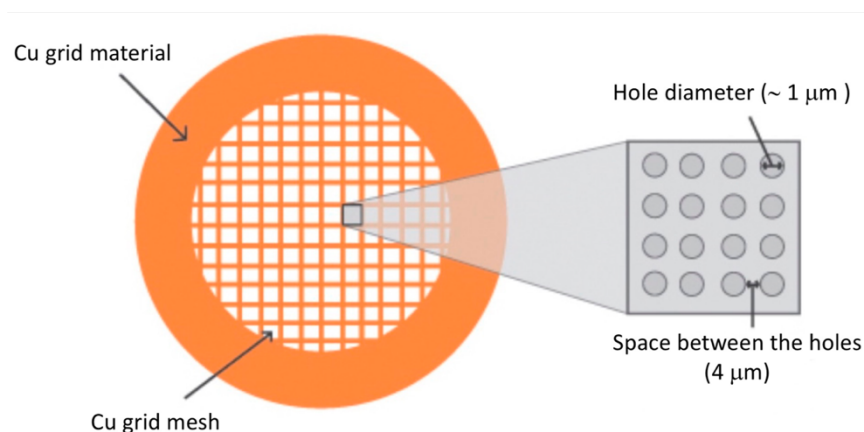


Figure 2.1. Schematic representation of Formvar (carbon-coated Cu grid), Ted-Pella#01883-F

Multiwalled carbon nanotubes (CNTs) were used as a standard for sp^2 carbon. To minimize contamination, the measurements were performed at liquid nitrogen temperature. The sp^2 content was calculated from peak area under π^* and σ^* excitations with peak center at 285 and 291.1 eV, respectively.

$$sp^2 = \frac{area(\pi^*)}{area(\pi^* + \sigma^*)} \quad (i)$$

2.4 Electrochemical Techniques

A single-compartment glass cell was used in a three-electrode measurement configuration [13]. The working electrode (BDD) was clamped to the bottom of the cell. The backside electrical contact was made to the BDD electrode by scratching the conducting p-Si substrate with SiC 800 grit paper, and then cleaning and coating the area with a layer of carbon from a pencil. This procedure produces a good ohmic contact between the working electrode and a copper current collector plate. A Viton™ O-ring between the cell and the working electrode defined the exposed geometric area of 0.2 cm². The counter electrode was a high purity platinum wire (0.5 mm diam.) sealed in glass, and a large area, spiral silver wire served as the quasi-reference electrode (Ag QRE). The potential of the Ag QRE in 0.5 mol L⁻¹ H₂SO₄ was 130 ± 4 mV vs. Ag/AgCl (3M KCl). Approximately 0.5-1 mL of ionic liquid was used for an experiment. Ar gas (99.9999% Praxair Inc.) blanketed the RTIL during an experiment with all the electrochemical experiments being performed at room temperature in a dry N₂-purged vinyl glove box. The relative humidity in the glove box was maintained below the detection limit of a hygrometer (0.1 % or 1000 ppm). All glassware were washed with detergent and then rinsed sequentially with deionized water, isopropanol, acetone, and ultrapure water, and finally, dried in an oven at 150 °C for at least 12 h

prior to use. The ultrapure water was obtained by passing house deionized water through a Barnstead E-Pure System (ion exchange and activated carbon columns, Thermo Scientific, USA). The ultrapure water had an electrical resistivity of $> 17 \text{ M}\Omega\text{-cm}$.

2.4.1 Cyclic Voltammetry

Cyclic voltammetry is the most widely used technique for acquiring qualitative information about the preliminary experiments and to probe an electrochemical system for the flow of current in response to perturbation by external applied potential. Potential is applied to the working electrode (with respect to the reference electrode), while the resulting current due to charge transfer (Faradaic) or flow of electrolyte ions (non-Faradaic) is monitored as current, i . A typical waveform for such potential sweep measurement is shown in Figure 2.2. The potential is swept between E_1 and E_2 at a known scan rate (v), while the current, i , is monitored as a function of potential (or time). Upon reaching E_2 , the potential is swept in the reverse direction (*i.e.*, E_2 to E_1), often at the same scan rate. The current, i , is governed by several factors, including applied potential, surface states, and area of working electrode, scan rate, electrolyte media, the roughness of electrode, and the type of redox species, if present.

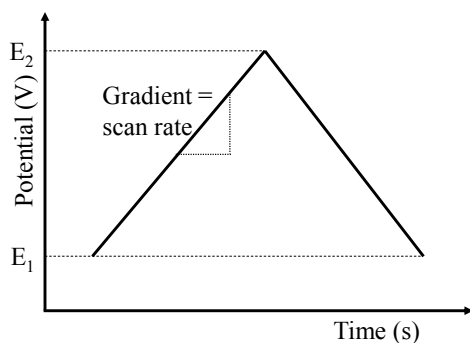


Figure 2.2. Illustration of waveform for cyclic voltammetry. The potential is scanned from E_1 to E_2 at a scan rate, v , that gives DC voltammetric current.

2.4.2 Electrochemical Impedance Spectroscopy

Electrochemical impedance spectroscopy (EIS) was performed at different applied DC potentials using a single frequency, and the entire frequency spectrum from 0.1 to 10^5 Hz with 20 data points collected per decade. A sinusoidal perturbation voltage of 10 mV (rms) was added to each negative-to positive-going DC applied potential in 200 mV increments. An equilibration time of 200 s was allowed before the acquisition of the impedance data at each potential. The full frequency EIS data were analyzed in the Nyquist plane using the CPE-based electrical equivalent circuit shown in Figure 2.3. R_s represents bulk electrolyte resistance and any electrode ohmic resistance in series with a parallel-connected constant phase element (CPE), C_{hf} is the high-frequency capacitance associated with the external electrical leads. As mentioned, the origin of C_{hf} is the capacitance that arises from the connecting electrical leads [14]. C_{hf} is usually in the range of nF and is potential-independent at the higher frequencies.

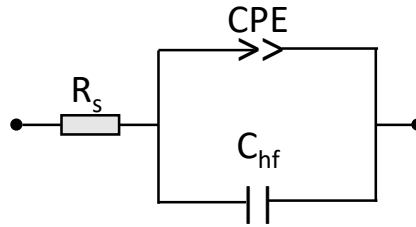


Figure 2.3. The representative electrical equivalent circuit that was used to fit the full-frequency impedance data.

In the Nyquist plot format, a pure capacitor exhibits frequency-independent impedance and produces a straight vertical line along the Z'' (imaginary) – Z' (real) plane in this plot. Polycrystalline electrodes are well known to exhibit a capacitance dispersion with frequency due to the atomic scale defects (steps, kinks, dislocations) and surface roughness (corrugations,

grooves) that lead to inhomogeneities in the current density and a local distribution of response time constants [38, 39]. The simplest way to compensate for this inhomogeneity is to use a CPE element that accounts for the frequency-dependent capacitance according to:

$$\check{Z}_{CPE} = \frac{1}{Q(j.2\pi f)^\alpha} \quad (\text{ii})$$

where Q and α are the CPE pre-factor and the exponent, respectively, with α being 1 for an ideal capacitor having a phase angle of -90° and less than 1 for a phase angle less than $-90^\circ * \alpha$, and f is the AC frequency (s^{-1}). EIS measures the total impedance response of the system. To separate impedance of individual component, one must interpret the impedance data based on behavior of appropriate equivalent electrical circuit. At lower frequencies, the capacitor will get charged and the current will increase at a decreasing rate, as predicted by the circuit's time constant. At higher frequencies, the capacitor acts as a short and the resistance dominates the system. This inflection point is known as “knee frequency”.

2.4.3 Single Frequency Impedance Measurements

Single-frequency impedance measurements were performed using an AC voltage amplitude of 10 mV (rms) added to each negative-to-positive going applied DC potential. Data were collected at DC potentials in 50 mV increments. The frequencies used were 600, 200, 100, 40, 10, 1 and 0.1 Hz. An equilibration time of 5 min was used after each applied DC potential before acquiring the impedance data. The imaginary impedance (Z'' , ohms) at a fixed AC frequency (f , s^{-1}) was converted to capacitance (C) in Farads using the equation (iii):

$$C = \left| \frac{1}{-2\pi f Z''} \right| \quad (\text{iii})$$

Capacitance values were then divided by the geometric area of the electrode (cm^2). Three sets of independent measurements were performed with different batches of purified RTILs and different diamond electrodes to assess the trend reproducibility. The stability of the electrode surface and interfacial organization were confirmed by recording background cyclic voltammograms before and after the potential-dependent EIS measurements.

REFERENCES

REFERENCES

- [1] N. Elgrishi, K.J. Rountree, B.D. McCarthy, E.S. Rountree, T.T. Eisenhart, J.L. Dempsey, A Practical Beginner's Guide to Cyclic Voltammetry, *J. Chem. Educ.* 95 (2018) 197–206. doi:10.1021/acs.jchemed.7b00361.
- [2] R. Jarošová, P.M. De Sousa Bezerra, C. Munson, G.M. Swain, Assessment of heterogeneous electron-transfer rate constants for soluble redox analytes at tetrahedral amorphous carbon, boron-doped diamond, and glassy carbon electrodes, *Phys. Status Solidi Appl. Mater. Sci.* 213 (2016) 2087–2098. doi:10.1002/pssa.201600339.
- [3] A. Tafel, M. Wu, E. Spiecker, P. Hommelhoff, J. Ristein, Fabrication and structural characterization of diamond-coated tungsten tips, (2019). <http://arxiv.org/abs/1902.01369>.
- [4] N. Wächter, C. Munson, R. Jarošová, I. Berkun, T. Hogan, R.C. Rocha-Filho, G.M. Swain, Structure, Electronic Properties, and Electrochemical Behavior of a Boron-Doped Diamond/Quartz Optically Transparent Electrode, *ACS Appl. Mater. Interfaces.* (2016) A-M. doi:10.1021/acsami.6b02467.
- [5] X. Yang, L. Haubold, G. Devivo, G.M. Swain, Electroanalytical performance of nitrogen-containing tetrahedral amorphous carbon thin-film electrodes, *Anal. Chem.* 84 (2012) 6240–6248. doi:10.1021/ac301124r.
- [6] H.J. Scheibe, B. Schultrich, D. Drescher, Laser-induced vacuum arc (Laser Arc) and its application for deposition of hard amorphous carbon films, *Surf. Coatings Technol.* 74–75 (1995) 813–818. doi:10.1016/0257-8972(95)08280-8.
- [7] H.J. Scheibe, B. Schultrich, DLC film deposition by Laser-Arc and study of properties, *Thin Solid Films.* 246 (1994) 92–102. doi:10.1016/0040-6090(94)90737-4.
- [8] D. Drescher, J. Koskinen, H.J. Scheibe, A. Mensch, A model for particle growth in arc deposited amorphous carbon films, *Diam. Relat. Mater.* 7 (1998) 1375–1380. doi:10.1016/S0925-9635(98)00211-8.
- [9] B.L.M. Veerasamy, V. S., Yuan J., Amaratunga A. A. J., Milne W. I., Gilkes K. W. R., Weiler M., Nitrogen Doping of Highly Tetrahedral Amorphous Carbon, *Phys. Rev. B.* 48 (1993) 954–959.
- [10] L. Valentini, J.M. Kenny, R.M. Montemali, L. Lozzi, S. Santucci, Influence of nitrogen and temperature on the plasma deposition of fluorinated amorphous carbon films, *J. Vac. Sci. Technol. A Vacuum, Surfaces, Film.* 20 (2002) 1210–1215. doi:10.1116/1.1479359.
- [11] W.I. Rodil, S.E., Morrison, N. A., Robertson, J., Milne, Nitrogen incorporation into

- tetrahedral hydrogenated amorphous carbon, *Phys. Status Solidi Appl. Res.* 174 (1999) 25–37. doi:10.1002/(SICI)1521-396X(199907)174:1<25::AID-PSSA25>3.0.CO;2-3.
- [12] L.M. Fischer, M. Tenje, A.R. Heiskanen, N. Masuda, J. Castillo, A. Bentien, J. Émneus, M.H. Jakobsen, A. Boisen, Gold cleaning methods for electrochemical detection applications, *Microelectron. Eng.* 86 (2009) 1282–1285. doi:10.1016/j.mee.2008.11.045.
- [13] M.C. Granger, M. Witek, J. Xu, J. Wang, M. Hupert, A. Hanks, M.D. Koppang, J.E. Butler, G. Lucazeau, M. Mermoux, J.W. Strojek, G.M. Swain, Standard electrochemical behavior of high-quality, boron-doped polycrystalline diamond thin-film electrodes, *Anal. Chem.* 72 (2000) 3793–3804. doi:10.1021/ac0000675.
- [14] J. Wallauer, M. Balabajew, B. Roling, Impedance Spectroscopy on Electrode | Ionic Liquid Interfaces, 2017. doi:10.1002/9783527682706.ch11.

Chapter 3

Potential-Dependent Capacitance of Boron-Doped Nanocrystalline Diamond Planar Electrodes in RTILs – Effect of Measurement Method and RTIL Type

3.1 Introduction

RTILs are highly concentrated (3-7 M) electrolytes composed of a relatively large organic cation and a smaller inorganic anion with a melting point at or below room temperature. Importantly, they contain *no* solvent. In other words, there is no dielectric solvent separating the ions from one another or from a charged electrode surface. They possess several practical attributes including environmental friendliness (non-volatile, non-toxic), a wide electrochemical window (> 4 V), moderate to high ionic conductivity (0.01 to 1.8 Sm^{-1}), and excellent electrochemical and thermal stability. These properties render RTILs potential replacements for traditional aqueous and organic electrolytes in electrosynthesis, energy storage, electrochemical sensing, and catalysis applications [1-5].

RTILs are more viscous than aqueous or organic electrolyte solutions. This reduces diffusional mass transport rates of soluble redox species and slows the reorganization of ions at the electrode interface in response to a potential perturbation. In other words, a central issue with using these materials is understanding how the RTIL environment affects capacitance, molecular adsorption, and heterogeneous electron-transfer kinetics. The organization of RTIL ions in the interfacial region of carbon electrodes as a function of potential is under study, but knowledge is not as well-developed as it is for aqueous and organic electrolytes at the same electrodes. The potential-dependent organization of RTIL ions at an electrified interface (so-called electric double layer) controls the potential drop in the liquid, hence the electric field driving the electron transfer,

and the mass transport of analytes. Understanding the structure-property relationship of these liquids at solid electrodes is necessary if these liquids are to be optimally used.

A common and central aspect of their usage is the structural and dynamic response (*i.e.*, capacitance-potential relationships) of electrified interfaces in these media. Since there is no dielectric solvent and the ions do not exist as discrete charges, the traditional Gouy-Chapman-Stern model for the electric double layer might not be appropriate for RTILs. Furthermore, due to the high ionic concentration, RTILs are expected to have high charge density at the interface. RTIL ions are often highly polarizable, asymmetric in shape, and chemically complex which results in several interionic forces, in addition to Coulombic ones, that affect the organization of ionic liquid ions: dispersion forces, dipole-dipole interactions, hydrogen bonding, and π stacking forces [3].

Borukhov et al. used the mean-field theories to find the distribution of ions and potential near a charged surface in a concentrated electrolyte [6]. The model incorporates steric limitations on ion packing calculating the maximum possible number density of ions by construction. It accounts for Coulombic interactions between the ions and the charged surface but does not consider ion-ion correlations arising from short-range Coulombic interactions. Recently, Kornyshev extended this model and applied it to understand C-E trends in RTILs [7]. Kornyshev model was later supported by Oldham [8] using computer simulations. It considers ion-ion correlations and proposes two possibilities: (i) at low electrode charge, interionic interactions are strong and cannot be ignored. In this case, the magnitude of the counter charge exceeds that of the charge at the electrode surface. To balance this excess charge, another layer of counter ions forms in proximity to the first layer. Thus, multiple layers of charge and counter-charge emerge, decreasing in charge magnitude as the distance from the electrode surface increases. This is called the over-screened regime, and (ii) at high electrode charge, ion-ion correlations become less

critical, and the excess charge gets localized in proximity to the electrode surface rather than successive layers of ions. The concentrations of ions at the interface reaches maximum allowed by steric limitations and the system is said to be in the region of lattice saturation. These behaviors of RTILs give either a bell- or a camel- or double-peaked shape for C-E trends. These complex trends are in stark contrast to the U-shaped curve predicted by GCS model for dilute electrolytes.

Most of the experimental work in this field have probed C-E trends by systematically modulating the molecular parameters of RTILs and electrode materials and correlating them with the C-E trends deduced using DC voltammetry, electrochemical impedance spectroscopy (EIS) [9–13], and electrocapillary curves [14–16]. Different spectroscopic and surface analysis techniques like sum frequency generation vibrational spectroscopy [17–19], surface enhanced Raman spectroscopy [20,21], in-situ Fourier transform infrared absorption spectroscopy [22], in-situ surface-enhanced infrared adsorption spectroscopy (SEIRAS) [23], etc. have also been used to probe the organization of RTIL ions near a charged electrode.

Metal electrodes like Au and Pt [24–30] exhibit the bell- or camel-shaped C-E curves with a defined capacitance maximum at the potential of zero charge. However, carbon electrodes like glassy carbon (GC), highly oriented pyrolytic graphite (HOPG), etc. do not follow the Kornyshev model. In an extensive work, Ohsaka and coworkers compared platinum, HOPG and GC electrodes and pointed out the differences in C-E trends. GC shows U-shape trends [16,24,25,30,31] in most systems with some complex trends [28] observed as well. These disparate C-E trends (camel-, bell- or U-shaped) for different electrode/electrolyte systems couldn't be convincingly rationalized. Rigorous justification of these seemingly contradictory experimental observations remains a challenge due to difficulties in reconciling theoretical studies and

experimental data [32]. Even after a decade of research, the structure and dynamics of these interfaces are not clear.

Of interest to our group is understanding the factors that influence the interfacial structure and heterogeneous electron-transfer kinetics at nanostructured carbon electrodes in RTILs. Long term, the goal is to correlate capacitance, molecular adsorption, and electron-transfer kinetics for soluble redox probes in RTILs with the nanostructured carbon electrode microstructure and surface chemistry. In this study, the potential-dependent capacitance of boron-doped nanocrystalline diamond thin-film electrodes was investigated in two different RTILs: 1-butyl-3-methylimidazolium hexafluorophosphate, [BMIM][PF₆], and 1-hexyl-3-methylimidazolium hexafluorophosphate, [HMIM][PF₆]. Imidazolium-based RTILs were chosen because of their wide use as an electrolyte and the relative stability of ions towards electrochemical decomposition.

3.2 Materials and Methods

3.2.1. Boron-Doped Diamond Electrodes

The boron-doped nanocrystalline diamond (BDD) thin-film electrodes were deposited on *p*-Si (111) substrates (Virginia Semiconductor, Inc., Fredricksburg, VA, ~ 0.001 Ω-cm). Deposition was performed by microwave-assisted chemical vapor deposition (CVD) using a commercial 1.5 kW reactor (Seki Technotron) [33]. Prior to diamond film growth, the polished silicon substrate was first abraded with 100 nm diamond powder suspended in water on a pad. The substrate was then rinsed copiously with ultrapure water. The substrate was then ultrasonically seeded with nanodiamond particles using an Opal Seed suspension (Adamas Nanotechnologies Inc., Raleigh, NC) for 30 min in a glass beaker. This suspension (5 % (wt./v)) consisted of 30 nm aggregates of detonation diamond particles dispersed in dimethyl sulfoxide (DMSO). The seeded

substrate was then rinsed 3x with ultrapure water in the glass beaker, wicked dry with a Kimwipe and fully dried with a stream of N₂ before being placed in the CVD reactor for overnight pump down. The BDD film was grown using methane diluted in hydrogen (C/H = 1% (v/v)) at a total gas flow rate of 200 sccm (standard cubic centimeter per minute), a system pressure of 35 torr, a substrate temperature estimated to be 825 °C (disappearing-filament optical pyrometer), and a growth time of 5-6 h. Boron doping was accomplished by adding 0.1 % (v/v) diborane in hydrogen to the source gas, producing a gas phase boron concentration of 10 ppm. After deposition, the methane and diborane flows were stopped, and the sample was cooled under a hydrogen plasma for 30 min by slowly reducing the power and pressure down to 150 W and 10 Torr. This post-growth cooling step is essential for minimizing the formation of sp²-bonded carbon at the surface that would result from the desorption of surface hydrogen (T >~ 450°C) and reconstruction of the surface carbon atoms if the plasma were extinguished at the growth temperature. The cool-down in atomic hydrogen is also critical for maintaining a hydrogen-terminated surface [34]. The doping level was estimated to be in the low 10²¹ cm⁻³ range based on Raman spectroscopic and Hall effect measurement data, as described previously [35]. The film thickness was 3-4 μm as estimated by the change in weight of the substrate after film deposition and cross-sectional SEM micrographs.

3.2.2 Gold Electrodes

The planar gold thin-film electrodes (1000 Å thick film, E-gun evaporation) were deposited on heavily doped p-type Si (100) (LGA Thin Films, Inc., Santa Clara, CA). The film was pretreated prior to use to oxidatively remove organic surface contaminants by a 5-min immersion in a mild piranha solution of 0.5 mol L⁻¹ H₂SO₄ and 25 wt. % hydrogen peroxide. *This cleaning solution is a strong oxidant and corrosive. It is dangerous and potentially unstable. It should be used with*

proper safety precautions. The film was then thoroughly rinsed with deionized water. This was followed by mounting the film at the bottom of an electrochemical cell with the solution contained by a Viton™. In the cell, the Au surface was pretreated by potential cycling in 0.5 mol L⁻¹ H₂SO₄ between -0.3 to 1.2 V (vs. Ag/AgCl) at 0.05 Vs⁻¹ [36]. The cycling was carried out until an unchanging voltammogram was observed (~40 cycles). A second pretreatment then followed that involved potential cycling in 0.5 mol L⁻¹ KOH from -0.2 to 1.2 V (vs. Ag/AgCl) at a scan rate of 0.05 V s⁻¹ (~10 cycles). These electrochemical pretreatments were followed by copious rinsing of the electrochemical cell and the mounted electrode with deionized water. The electrode surface was then immersed in ultrapure (triply distilled and stored over activated carbon) isopropanol for 20 min as a final cleaning step.

3.2.3 Chemicals

The RTILs, 1-butyl-3-methylimidazolium hexafluorophosphate [BMIM][PF₆] (IL-0011-UP) and [HMIM][PF₆] (IL-0018-UP), were procured from a commercial source (IoLiTec, Tuscaloosa, AL, ≥ 99.5 % purity). The RTILs were purified using a protocol described previously [37]. Briefly, the *as-received* RTIL was initially stored over activated carbon (Sigma-Aldrich) for 5 days with occasional mixing. The RTIL was then filtered using a 0.22 µm Teflon syringe filter (Whatman) directly into the electrochemical cell at the time of use and heated to 70 °C for 1 h while continuously purging with ultrapure Ar gas (99.9999 %). All processes were performed in a dry N₂-purged vinyl glove box (Coy Laboratories, Grass Lake, MI). The water content in the RTIL was measured before and after this so-called ‘sweeping’ treatment using thermogravimetric analysis (Model Q500, TA Instruments) under a dry N₂ blanket. The physical properties of the RTILs used are given in Table 3.1.

3.2.4 Electrochemical Measurements

A single-compartment glass cell was used in a three-electrode measurement configuration [38]. The working electrode (BDD) was clamped to the bottom of the cell. The backside electrical contact was made to the BDD electrode by scratching the conducting p-Si substrate with SiC 800 grit paper, and then cleaning and coating the area with a layer of carbon from a pencil. This procedure produces a good ohmic contact between the working electrode and a copper current collector plate. A Viton™ O-ring between the cell and the working electrode defined the exposed geometric area of 0.2 cm². The counter electrode was a platinum wire (0.5 mm diam.), and a large area, spiral silver wire served as the quasi-reference electrode (Ag QRE). The potential of the Ag QRE in 0.5 mol L⁻¹ H₂SO₄ was 130 ± 4 mV vs. Ag/AgCl (3M KCl). Approximately 1 mL of ionic liquid was used for an experiment. Ar gas (99.9999% Praxair Inc.) blanketed the RTIL during an experiment with all the electrochemical experiments being performed at room temperature in a dry N₂-purged vinyl glove box. The relative humidity in the glove box was maintained below the detection limit of a hygrometer (0.1 % or 1000 ppm). All glassware were washed with detergent and then rinsed sequentially with deionized water, isopropanol, acetone, and ultrapure water, and finally, dried in an oven at 150 °C for at least 12 h prior to use. The ultrapure water was obtained by passing house deionized water through a Barnstead E-Pure System (ion exchange and activated carbon columns, Thermo Scientific, USA). The ultrapure water had an electrical resistivity of > 17 MΩ-cm.

Cyclic voltammetry (CV) and electrochemical impedance spectroscopy (EIS) measurements were performed using a computer-controlled electrochemical workstation (Model 650A, CH Instruments Inc., Austin, TX). Cyclic voltammograms were recorded as a function of

the scan rate (0.01-0.5 V s⁻¹) and the capacitance was calculated from the slope of background current vs. scan rate plots according to:

$$j = C_{dl} \nu \quad (i)$$

where j (A cm⁻²) is background current density at a specific potential, C_{dl} (F cm⁻²) is interfacial capacitance and ν (V s⁻¹) is the scan rate. CV was also used to define the potential window to be investigated by EIS. A large potential window (~4-6) served as a measure of RTIL purity.

Electrochemical impedance spectroscopy (EIS) was performed at different applied DC potentials using a single frequency, and the entire frequency spectrum from 0.1 to 10⁵ Hz with 20 data points collected per decade. A sinusoidal perturbation voltage of 10 mV (rms) was added to each negative-to positive-going DC applied potential in 200 mV increments. An equilibration time of 200 s was allowed before the acquisition of the impedance data at each potential. The full frequency EIS data were analyzed in the Nyquist plane using the CPE-based electrical equivalent circuit shown in Figure 3.1. R_s represents bulk electrolyte resistance and any electrode ohmic resistance in series with a parallel-connected constant phase element (CPE), C_{hf} is the high-frequency capacitance associated with the external electrical leads and R_{ad} is the charge-transfer resistance associated with electron exchange between a specifically adsorbed ion and the charged electrode. As mentioned, the origin of C_{hf} is the capacitance that arises from the connecting electrical leads [39]. C_{hf} is usually in the range of nF and is potential-independent.

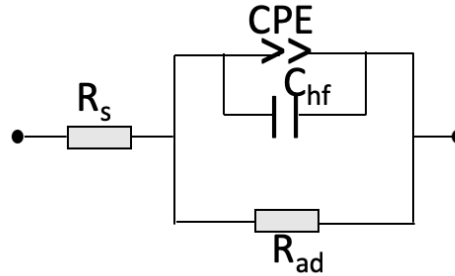


Figure 3.1. The electrical equivalent circuit used to fit the impedance data in the Nyquist plane.

In the Nyquist plot format, a pure capacitor exhibits frequency-independent impedance and produces a straight vertical line along the Z'' (imaginary) – Z' (real) plane in this plot. Polycrystalline electrodes are well known to exhibit a capacitance dispersion with frequency due to the atomic scale defects (steps, kinks, dislocations) and surface roughness (corrugations, grooves) that lead to inhomogeneities in the current density and a local distribution of response time constants [38, 39]. The simplest way to compensate for this inhomogeneity is to use a CPE element that accounts for the frequency-dependent capacitance according to:

$$\check{Z}_{CPE} = \frac{1}{Q(j.2\pi f)^\alpha} \quad (\text{ii})$$

where Q and α are the CPE pre-factor and the exponent, respectively, with α being 1 for an ideal capacitor having a phase angle of -90° and less than 1 for a phase angle less than $-90^\circ * \alpha$, and f is the AC frequency (s^{-1}).

Single-frequency impedance measurements were also performed using an AC voltage amplitude of 10 mV (rms) added to each negative-to-positive going applied DC potential. Data were collected at DC potentials in 50 mV increments. The frequencies used were 600, 200, 100, 40, 10, 1 and 0.1 Hz. An equilibration time of 5 min was used after each applied DC potential before acquiring the impedance data. The imaginary impedance (Z'' , ohms) at a fixed AC frequency (f , s^{-1}) was converted to capacitance (C) in Farads using the equation (3):

$$C = \left| \frac{1}{-2\pi f Z''} \right| \quad (\text{iii})$$

Capacitance values were then divided by the geometric area of the electrode (cm^2). Three sets of independent measurements were performed with different batches of purified RTILs and different diamond electrodes to assess the trend reproducibility. The stability of the electrode surface and interfacial organization were confirmed by recording background cyclic voltammograms before and after the potential-dependent EIS measurements.

3.2.5 Characterization of the BDD Electrodes and Purified RTILs

The impurity and water content of the RTILs were assessed using Fourier transform infrared spectroscopy (FTIR) in the transmission mode (Mattson Galaxy, Series 3000). A 500 μL drop of the purified RTIL was placed between two potassium bromide salt plates in the N_2 -filled vinyl glove box. The assembly was then quickly transferred through the laboratory atmosphere to the N_2 -purged sample compartment of the FTIR. One hundred scans were co-added at a spectral resolution of 4 cm^{-1} . Thermogravimetric analysis (TGA Q500, TA Instruments) was also performed under a dry N_2 atmosphere to estimate the water content. The analysis involved placing a purified drop of the RTIL into the instrument's Pt sample boat that was first dried and cleaned by heating in a gas flame. The RTIL sample was then heated from room temperature to 300 $^{\circ}\text{C}$ at 10 $^{\circ}\text{C min}^{-1}$. A dry N_2 gas blanket was maintained over the RTIL during the entire temperature ramp to minimize water uptake from the atmosphere. To consider buoyancy effects caused by the change in the density of dry N_2 as the temperature increased, a blank was run with the empty Pt sample boat. The weight-change vs. temperature data for the RTILs were all corrected using this blank.

3.2.6 Statistical Data Analysis

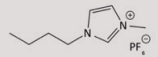
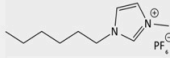
At least three sets of independent electrochemical measurements were performed with each of the purified RTILs using at least three different BDD electrodes, all deposited under identical conditions, to assess trend reproducibility. Data are presented as mean \pm standard deviation ($n \geq 3$).

3.3 Results

3.3.1 Physicochemical Characterization of the RTILs

A comparison of the chemical structure and physical properties (viscosity, ionic conductivity at 25 °C, dielectric constant, density and molar ionic concentration) of the two RTILs, [BMIM][PF₆] and [HMIM][PF₆], are provided in Table 1. [HMIM][PF₆] is 2x more viscous than [BMIM][PF₆] and both are 200-400x more viscous than water. The reported dielectric constant of [HMIM][PF₆], 8.9, is slightly lower than the value for [BMIM][PF₆], 11.4, and 8x lower than the dielectric constant for water. The reported ionic conductivity of [BMIM][PF₆], 1.92 mS cm⁻¹, is 2.5x higher than that of [HMIM][PF₆], 0.80 mS cm⁻¹, due to the higher mobility of smaller [BMIM]⁺ cation and associated ion pairs. Both RTILs are denser than water. The ionic concentrations were calculated from the molar mass and density of the respective RTIL, hence, these values only provide approximate ionicity [40]. The presumption in this calculation is that there is no ion pairing that would reduce the true ionic concentration. Tokuda et al. however, found the true ionicity of several classes of RTILs to be between 50 and 80% of the total ionic concentration due to ion pairing effects [40].

Table 3.1. Physical properties of [BMIM][PF₆] and [HMIM][PF₆] at 25°C.

| RTIL | Molecular Structure | Mol. Wt. (g mol ⁻¹) | Viscosity (η , cP) | Ionic Conductivity (σ , mS cm ⁻¹) | Dielectric Constant (ϵ) | Density (ρ , g cm ⁻³) | Ionic Concentration (mol L ⁻¹) |
|--------------------------|---|---------------------------------|--------------------------|---|------------------------------------|---|--|
| [BMIM][PF ₆] |  | 219.12 | 267 | 1.92 | 11.4 | 1.37 | 6 |
| [HMIM][PF ₆] |  | 312.24 | 465 | 0.80 | 8.9 | 1.30 | 4 |

Data were provided by the chemical supplier.

Electrode capacitance measurements in RTILs can be influenced by impurities present, such as organic contaminants, halide ion residues from the synthesis and water impurity [32]. TGA weight loss vs. temperature profiles for *as received*, purified/dry, and purified + atmosphere-exposed [BMIM][PF₆] are shown in Figure 3.2A. Similar weight loss profiles were observed for [HMIM][PF₆] (data not shown). The weight loss is presumed to be due to the volatilization of water impurity. There was no weight loss detected for the purified RTIL until a temperature in excess of 200 °C. The maximum weight loss measured between 25 and 200 °C, 0.02 wt.% or 200 ppm, is near the minimum weight change detectable with the instrument. In contrast, significant weight loss was recorded for the *as received* RTIL starting at 50 °C with a maximum loss of 1.23 wt.% or 12,300 ppm. Significant weight loss was also observed for the purified RTIL exposed to the laboratory air for just ~10 min. The weight change starts at 75 °C and reaches a maximum loss of 0.9 wt.% or 9000 ppm. This demonstrates that this particular RTIL incorporates water quite quickly. This concentration is slightly lower than the 12,300 ppm concentration seen for *as received* RTIL. The water content measured using the same method for *as received* [HMIM][PF₆] decreases from 6000 to 65 ppm after purification. In summary, the water content after purification of [BMIM][PF₆] and [HMIM][PF₆] was 100-200 ppm, as measured by this technique.

FTIR absorbance spectra for purified [BMIM][PF₆] and [HMIM][PF₆] are shown in Figure 3.2B. As expected, the vibrational modes for the two RTIL cations and anions are similar. The peaks between 2800 and 3000 cm⁻¹ are attributed to sp³ aliphatic C-H stretching modes (hexyl, butyl and methyl groups). The peaks between 3000 and 3200 cm⁻¹ arise from sp²-bonded aromatic C-H stretches in the imidazolium ring. A sharp peak at 1575 cm⁻¹ is due to the C=C stretch of the imidazolium ring. Another intense peak at 1169 cm⁻¹ is due to the C-N stretch of the ring nitrogen. Finally, the peak at 750 cm⁻¹ is attributed to the anti-symmetric [PF₆]⁻ stretching modes of the anion [41]. While not the most sensitive method, importantly, the spectra are devoid of a peak centered around 3400 cm⁻¹ reflective of the O-H stretch for water impurity.

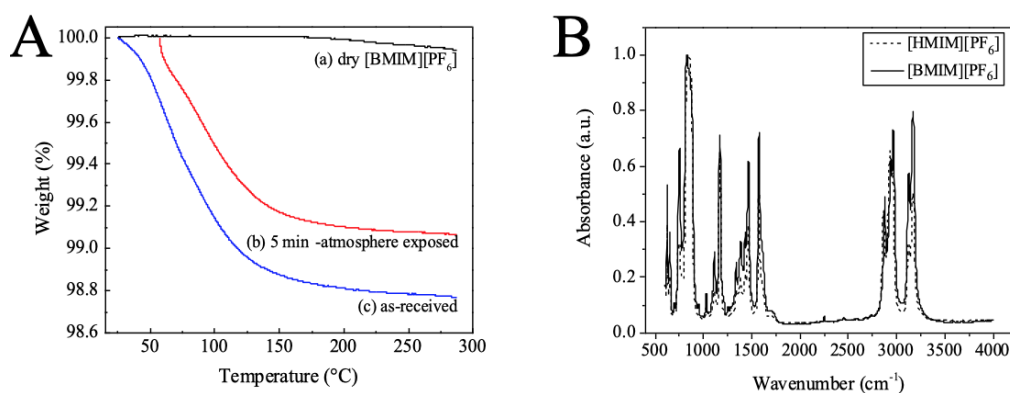


Figure 3.2. (A) Comparison of TGA weight loss (%) vs. temperature profiles for as received (blue line), purified (black), and purified [BMIM][PF₆] and atmosphere exposed (red) [BMIM][PF₆]. (B) FTIR absorbance spectra for purified [BMIM][PF₆] (solid line) and [HMIM][PF₆] (dashed line).

Not shown is the spectrum for a purified RTIL, [BMIM][PF₆], exposed to the laboratory atmosphere for *ca.* 10 min. For such a sample, the absorbance spectrum shows the same peaks as well as measurable intensity in the 3300-3500 cm⁻¹ region due to the O-H stretch from water contamination.

3.3.2 Electrochemical Potential Window

Figure 3.3 shows cyclic voltammetric current density vs. potential (j - E) curves for BDD in [BMIM][PF₆] and [HMIM][PF₆]. The curves were recorded at 0.1 V s⁻¹. In this work, a current density of 50 μ Acm⁻² was selected to define the potential window limits for the electrical double layer region. A potential window of *ca.* 6 V is observed for [HMIM][PF₆]. Some unknown peak anodic current can be observed between 2 and 2.5 V, which may possibly be due to hydrolysis of [PF₆]⁻ ions [42]. The peak at *ca.* 1.8 V is attributed to the oxidation of trace water impurities [43]. Typically in RTILs, the cathodic limit is set by the reduction of the cation and the anodic limit is set by the oxidation of the anions [44]. At potentials positive of 3 V in [HMIM][PF₆] electrolyte ions start decomposing and give rise to high current densities on the order of mA cm⁻². The voltammogram for [BMIM][PF₆] was recorded over a narrower potential range but a window of \sim 4 V is evident. Kroon et al. proposed that the electrochemical breakdown of ionic liquid is more complex than an electron-transfer reaction and involves radical-radical coupling and disproportion reactions [44]. No peaks for oxygen reduction were detected between 0 to -2 V as the electrolytes were purged with pure Ar before the start of an experiment. The shapes of the curves were unchanged with repeated cycling. These voltammetric data are consistent with the BDD electrode being of good quality and the RTIL being relatively pure and devoid of water. The potential range of -1 to 1 V vs. Ag QRE was chosen to probe the EDL or electric-double layer region using capacitance measurements.

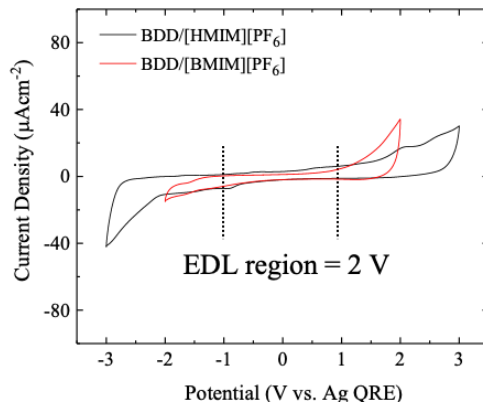


Figure 3.3 Cyclic voltammetric (j - E) curves for a BDD planar electrode in purified [HMIM][PF₆] (black) and [BMIM][PF₆] (red). Scan rate = 0.1 V s⁻¹.

Figure 3.4A and B show cyclic voltammetric j - E curves recorded over a narrower potential window from -0.5 to 1.0 V as a function of scan rate (0.01 to 0.5 V s⁻¹) in (A) [HMIM][PF₆] and (B) [BMIM][PF₆], respectively. The curves have the characteristic rectangular shape about the zero current line expected for capacitive current. The current density measured at 0.2 V increases with scan rate in both [BMIM][PF₆] and [HMIM][PF₆] from 0.3 to 5.5 μA cm⁻² and 0.1 to 3 μA cm⁻², respectively. Figure 3.4C shows the plots of the current density at 0.2 V versus the scan rate for [BMIM][PF₆] and [HMIM][PF₆] on a log-log scale. The plots are linear ($R^2 > 0.999$) with a slope of 0.93 and 0.89 for [BMIM][PF₆] and [HMIM][PF₆], respectively, which is consistent with the current being capacitive at this potential (expected value 1.0). At these scan rates, the RTIL ions are able to adjust their counter-balancing excesses in the interfacial region as fast as the excess surface charge on the electrode changes with the potential scan rate. The lower slope for [HMIM][PF₆] results from the increased viscosity. The 0.5 Vs⁻¹ scan rate is probably approaching the upper limit of the ions in the more viscous RTIL to adjust in response to the potential change. The electrode capacitance at 0.2 V, calculated from the slope of the plots using equation (i), is 10.8 and 6.0 μF cm⁻² for [BMIM][PF₆] and [HMIM][PF₆], respectively. Figure 3.4D compares the j - E curves recorded at 0.1 Vs⁻¹ for [BMIM][PF₆] (black) and [HMIM][PF₆] (red). Clearly, the

background current is lower in the more viscous [HMIM][PF₆]. This is due to the slightly lower dielectric constant and total ionic concentration of [HMIM][PF₆].

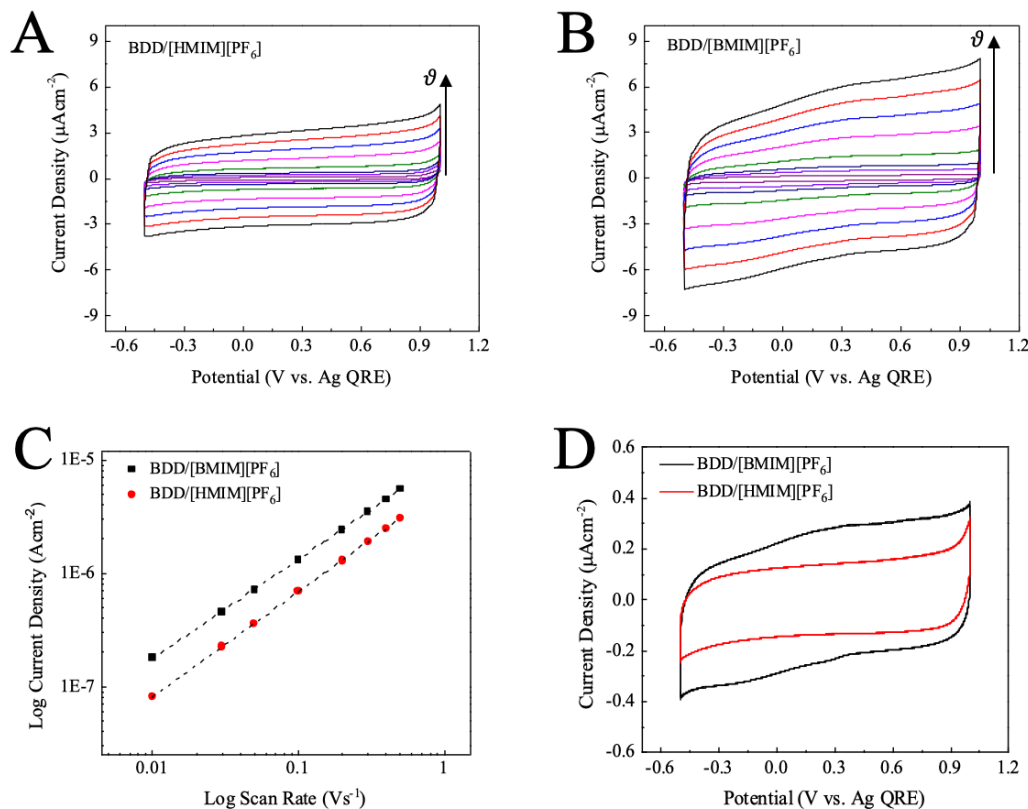


Figure 3.4. Cyclic voltammetric j vs. E curves recorded as a function of scan rate (0.01 to 0.5 V s⁻¹) for a BDD planar electrode in (A) [HMIM][PF₆] and (B) [BMIM][PF₆]. (C) Plots of log j at 0.2 V vs. log v for the same electrode in the two RTILs. (D) Comparison of the cyclic voltammetric j vs. E curves for the BDD electrode in the two RTILs at 0.1 V s⁻¹.

3.3.3 Capacitance-Potential Trends in the RTILs

Figure 3.5A shows an example Nyquist plots of the real (Z') vs. imaginary (Z'') components of the total impedance (black solid squares) for a BDD electrode in [HMIM][PF₆] at 0.3 V. Experimental data are presented in the frequency range from 0.1 to 10⁵ Hz as is the corresponding fit (red solid line) of the experimental data to the equivalent circuit shown in Figure 3.1. The circuit, representing the working electrode-RTIL interface, consists of a bulk electrolyte

solution ohmic resistance and any electrode resistance (R_s) in series with a parallel-connected double-layer capacitance modeled as a constant phase element (CPE) plus a high-frequency capacitance (C_{hf}) and a charge-transfer resistance for contact adsorbed ions on the electrode surface. The curve in Figure 3.5A shows a slight tilt from an ideal vertical line (expected for a pure capacitor), consistent with the capacitive processes controlling the current flow. This trend is commonly seen with a CPE-containing electrical circuit [26,45–47]. The inset in Figure 3.5A shows the dispersion of the CPE exponent (α) as a function of applied potential. The value of α indicates the ‘ideality’ of the capacitor where α is equal to 1 for a pure capacitor. For the BDD electrodes used in this study, a variation in α from 0.93 to 0.97 with a mean of (0.95 ± 0.01) was observed. In other words, the BDD electrodes behave in an ideally polarizable manner at these potentials in the RTILs.

Figure 3.5B shows the Bode plots of the total impedance $\log(|Z|)$ and \log phase angle vs. frequency for a BDD planar electrode in [HMIM][PF₆]. The data were recorded at 0.3 V. The impedance at high frequency (>20 kHz) is dominated by the ohmic resistance of the RTIL, R_s . The high frequency element C_{hf} mainly dominates in the frequency region (20-100 kHz frequency region). It does not have any significant influence on the CPE values. This capacitance is on the order of 1 nFcm^{-2} and does not correlate with the applied potential. The C_{hf} element arises from the electrical connecting cable capacitance [48]. To verify that C_{hf} does not arise from the ohmic contact between the electrode and Cu current collector plate, a control experiment was performed by making ohmic contact in two different ways: i) scratching the back (silicon side) of the electrode with SiC (silicon carbide paper 800 grit) followed by cleaning with isopropanol and covering with graphite, and ii) scratching the back side with the tip of a diamond pen, followed by applying a drop of liquid gallium to make ohmic contact. No difference in C_{hf} value was found. For more

details on reducing the artifact in impedance measurements, we refer the readers to a study performed by Roling and coworkers [49].

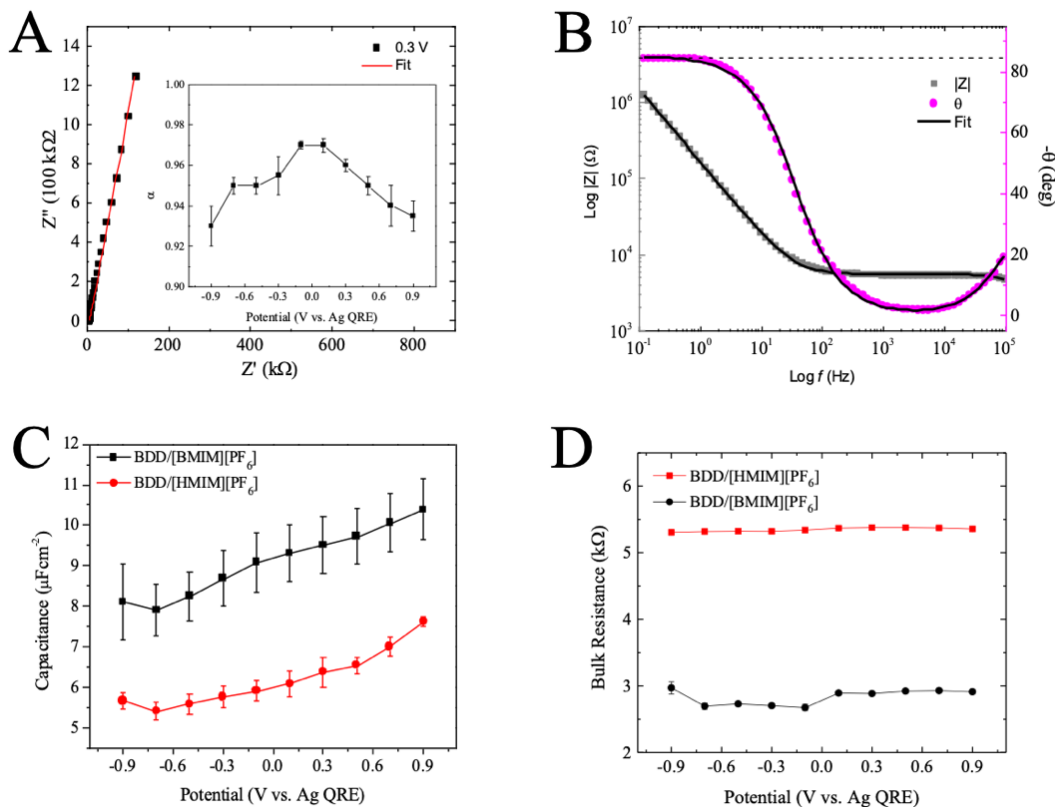


Figure 3.5. (A) Nyquist plot of the real (Z') vs. imaginary (Z'') components of the total impedance for BDD in [HMIM][PF₆] at 0.3 V. The inset show dependence of α on the potential. (B) Representative Bode plot for $\log |Z|$ and phase angle vs. \log frequency for [HMIM][PF₆] at 0.3 V. (C) Bulk resistance for [BMIM][PF₆] (red circles) and [HMIM][PF₆] (black squares) as a function of potential. (D) Capacitance vs. potential ($C-E$) profiles for BDD in contact with [HMIM][PF₆] (black squares) and [BMIM][PF₆] (red circles). The $C-E$ profiles were generated from EIS data by fitting the full frequency spectrum at each potential. Values are presented as mean \pm std. dev. for $n \geq 3$ measurements with different BDD electrodes in each RTIL.

The lower frequency impedance (100 to 0.1 Hz) is dominated by the CPE element. At these frequencies, the modulus slope of is near -0.9, which is also reflected in the α value being close to 1. At low frequencies, the phase angle is -84.5°, close to -90° characteristics of an ideal capacitor. The electrolyte ohmic resistance values for [BMIM][PF₆] and [HMIM][PF₆] are 2830 ± 94 and

5345 \pm 27 Ω (Fig 3.5C). The R_s values are independent of applied potential as expected. Figure 3.5D shows C-E curves for a BDD thin-film electrode in [BMIM][PF₆] and [HMIM][PF₆] generated using the full frequency spectrum EIS data. Capacitance values are plotted as mean \pm standard deviation calculated from three independent sets of measurements with three different BDD electrodes. The capacitance for [HMIM][PF₆] and [BMIM][PF₆] varies minimally over the potential range from 5.5 to 7.5 and 8.0 to 10.5 μFcm^{-2} , respectively. These capacitance values are consistent with other limited data reported in the literature for boron-doped diamond electrodes: 5 – 10 $\mu\text{F cm}^{-2}$ [50]. There is a capacitance minimum in both RTILs (Fig. 3.5C) at -0.750 V with a progressive trend of increasing capacitance with increasing positive potential. These values are similar to the 6.0 and 10.8 $\mu\text{F cm}^{-2}$ values determined from the cyclic voltammetric data (Fig. 3.4).

3.3.4 Hysteresis in Capacitance-Potential Trends in the RTILs

Hysteresis is often observed in capacitance vs. potential data recorded for electrodes in ionic liquids. This means that the capacitance values measured as a function of potential in one direction are different from the values measured at the same potentials in the reverse direction [23,51–53]. Capacitance hysteresis effects in RTILs are often observed when AC methods are used and could originate from (i) potential-dependent changes in the electrode surface chemistry or microstructure and (ii) slow relaxation processes in the viscous RTIL dominating below 10 Hz [54]. On the other hand, minimal capacitance hysteresis has been reported by Lucio *et al.* for [BMIM][BF₄] in contact with polycrystalline Au [55] and [BMIM][PF₆] in contact with polycrystalline BDD electrodes [56]. Given the excellent microstructural and surface chemical stability of BDD electrodes, we anticipated minimal hysteresis in the C-E curves. Example C-E data for BDD in [HMIM][PF₆] with two directions of changed applied potential are shown in

Figure 3.6A. The capacitance ranges from 4-7 $\mu\text{F cm}^{-2}$ over the potential range with little hysteresis. This is typical of most measurements made with the BDD planar electrodes in this work that were deposited in the high 10^{20} to low 10^{21} cm^{-3} dopant range. For these measurements, a well-defined minimum at *ca.* -0.75 V was not observed (see Fig. 3.5C). Figure 3.6B shows cyclic voltammetric (*j* vs. *E*) curves recorded at the BDD electrode before and after the impedance data collection. The overlapping curves reflect the stability of the diamond electrode microstructure and surface chemistry at these potentials and over this measurement time scale which was 5 – 8 h.

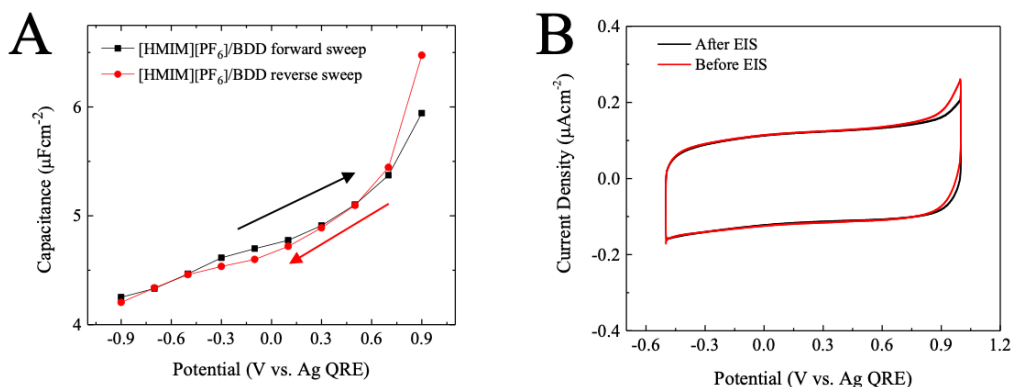


Figure 3.6. Capacitance vs. potential (*C-E*) data for a BDD planar electrode recorded in [HMIM][PF₆]. Capacitance values were determined from the full spectrum EIS data recorded from negative to positive potentials in the forward direction (black squares), and from positive to negative potentials in the reverse direction (red circles).

3.3.5 Single Frequency Capacitance Measurements

The time scale of RTIL ion reorganization at the electrode-solution interface in response to a potential perturbation is important to know when making capacitance measurements at a single frequency. The slow response time of ions in the viscous RTILs can affect (underestimate) the true capacitance [57]. A series of *C-E* measurements were made at different single AC frequencies to learn more about the response time. Figure 3.7A shows that the measured capacitance at all potentials strongly depends on the AC frequency. The measured capacitance increases with

decreasing AC frequency, as expected (see Equation (iii)). At low frequencies (<10 Hz), the capacitance takes on a U-shape and shows some variation at different potentials. At the highest frequencies (200 and 600 Hz), the measured capacitance is quite low, $1\text{--}2 \mu\text{Fcm}^{-2}$. At intermediate frequencies (10 and 100 Hz), the capacitance is $3\text{--}4 \mu\text{Fcm}^{-2}$ and largely independent of the potential. Only at the lowest frequencies (0.1 and 1 Hz), does the capacitance show some variation with electrode potential. The maximum capacitance observed at 0.9 and 1 V vs. Ag QRE using 0.1 Hz is 34 and $50 \mu\text{F cm}^{-2}$, respectively. The capacitance minimum (-0.5 V vs. Ag QRE) is close to the minimum observed in the C - E plots generated from EIS data (Fig. 3.5C). Figure 3.7B shows the capacitance measured at -0.5 V vs. Ag QRE as a function of log frequency. A pseudo-linear trend ($R^2 = 0.75$) is seen with the capacitance decreasing with increasing frequency. The capacitance decreases from 6.0 to $1.2 \mu\text{Fcm}^{-2}$ as the measurement frequency is increased from 0.1 to 600 Hz.

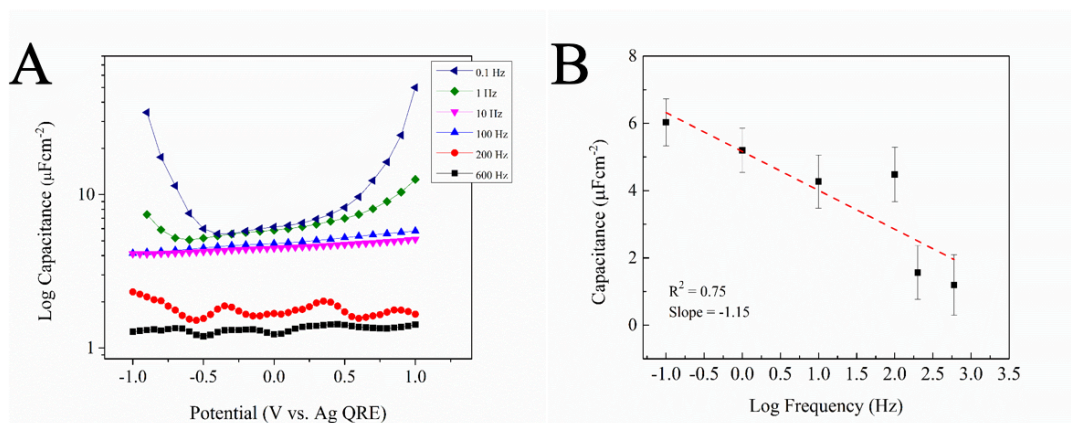


Figure 3.7. (A) Log capacitance-potential curves generated from the single frequency impedance technique for BDD in [HMIM][PF₆] as a function of a fixed AC frequency. The arrow indicates increasing frequency from 0.1 to 600 Hz. (B) Capacitance at -0.5 V as a function of log frequency. ($R^2 = 0.75$). Values are reported as mean \pm std. dev. for $n \geq 3$ measurements with different BDD electrodes.

3.3.6 Shapes of the Capacitance-Potential Curves

Bell- or camel-shape capacitance-potential curves are generally observed for metal electrodes in contact with RTILs, as predicted by the theory put forward by Kornyshev et al. [7]. Parabolic or U-shape curves were observed for all the BDD electrodes used in this work. A similar curve shape has been reported for other BDD and carbon electrodes [18,24,25,31,50,59]. Figure 3.8A compares CVs recorded at 0.1 Vs^{-1} for BDD and Au planar film electrodes in [HMIM][PF₆]. The capacitance at 0.2 V calculated from voltammetric current for Au as a function of scan rate (0.01 to 0.5 Vs^{-1}) using Equation 1 is $21 \mu\text{Fcm}^{-2}$ with $R^2 = 0.995$. The background current for Au is $\sim 5\times$ higher than for BDD at all potentials. The reason for this is that BDD has a lower density of electronic states than does the metal and this leads to a lower excess surface charge density at all potential.

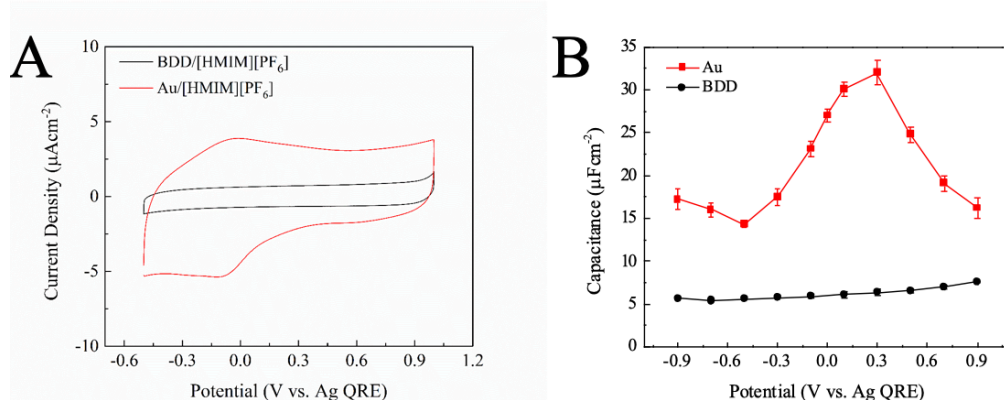


Figure 3.8. A. Comparison of the cyclic voltammetric j vs. E curves recorded at 0.1 Vs^{-1} for BDD (black inner curve) and Au (red outer curve) in [HMIM][PF₆]. (B) Capacitance-potential curves for Au film and BDD electrode in contact with [HMIM][PF₆]. The capacitance values were determined from the full frequency spectrum EIS data. Values are reported as mean \pm std. dev. for $n \geq 3$ measurements with different BDD electrodes.

Figure 3.8B shows C - E trends for the two electrodes in the same RTIL. The capacitance of BDD is 4-7x lower than the capacitance of Au depending on the potential. Capacitance values for

BDD in H₂SO₄ (*ca.* 5-12 $\mu\text{F cm}^{-2}$) are also 3-6x lower than values for a metal electrode, like Au. A capacitance maximum of 32.5 $\mu\text{F cm}^{-2}$ is seen for Au at 0.3 V. In contrast, the capacitance for BDD shows a minimum around -0.7 V and a slight increase with increasing positive potential. The reproducibility of *C-E* data for BDD and Au was quite high given the small error bars.

3.4 Discussion

The goals of the work reported on herein were two-fold: (i) investigating how a change in the RTIL cation type and viscosity affect the potential-dependent capacitance of low-oxygen, boron-doped diamond electrodes and (ii) understanding how the method used affects the measured capacitance in the solvent-less ionic liquids. The diamond films were heavily boron doped (low 10^{21} cm^{-3} range), so the electrodes are semi-metallic in their electronic properties. Generally speaking, there is limited data available in the literature regarding the behavior of conducting diamond and diamond-like carbon electrodes in RTILs. There are two reports on the capacitance of BDD in RTILs in the literature [30,50]. Lucio et al., for example, observed increasing capacitance from 3.9 to 6.4 μFcm^{-2} over a potential range -1.18 to 0.82 V vs. Fc/Fc⁺ in [BMIM][BF₄]. Our capacitance data match well with data in these two studies.

The capacitance values for the BDD electrodes used herein ranged from 4-10 $\mu\text{F cm}^{-2}$ at potentials between -1 and 1 V vs. Ag QRE. The capacitance at all potentials was higher in [BMIM][PF₆] than in [HMIM][PF₆]. This is due to (i) the higher ionic concentration and lower viscosity and (ii) the smaller size of the organic cation and presumably the ion pair size in [BMIM][PF₆]. The latter leads to a counterbalancing charge layer on the ionic liquid side of the interface that is positioned closer to the electrode surface. The capacitance data for the electrodes in the two RTILs are similar to values recorded in 0.5 mol L⁻¹ H₂SO₄. This is expected as the

dielectric constant of these two RTILs is *ca.* 10x lower than water, but the ionic concentration is 5-10x higher than the aqueous electrolyte. Finally, little hysteresis was observed in the capacitance-potential data when making measurements from negative to positive potentials and then in the reverse direction. This observation confirms the stability of the diamond electrode microstructure and surface chemistry over the potential range probed. In other words, BDD behaves as an ideally polarizable electrode in RTILs over the narrow potential range from -1 to 1 V vs. Ag QRE.

Water is an adventitious impurity in RTILs that will increase the capacitance of electrodes due to an increase in the dielectric constant of the medium, less ion pairing and increased interfacial distribution of ions at the electrode as a function of the potential [60]. Water impurity will also increase the voltammetric background current, reduce the working potential window and give rise to an oxidation peak near 2 V vs. Ag QRE [61]. The RTILs used in this study had an estimated water content in the 60-200 ppm range. Anaredy et al. have shown that water content in the range of 100-4000 ppm level has potential-dependent minimum influence on DC voltammetric and capacitive current [43]. It is concluded that the results presented herein are largely not influenced by water contamination.

The results presented herein indicate that the capacitance values for BDD electrodes in RTILs depends on the measurement method used. Lucio et al. first reported this same observation in their work with BDD electrodes [56]. The most accurate method for measuring the capacitance of BDD electrodes is by recording the full frequency EIS data and then fitting the data to an appropriate equivalent circuit. The equivalent circuit used can be a simple Randle's type circuit with the capacitor replaced with a constant phase element (CPE). If such an equivalent circuit is used, the experimental data fit the simulated data at all frequencies except very high frequencies

where the capacitance of leads and connecting wires can have an influence in RTILs. The C-E profiles constructed using single-frequency impedance data produce qualitatively similar curves. However, the magnitude of capacitance varies with the frequency. Care must be taken to make the measurement using an AC frequency at which the RTIL ions can adjust themselves in the interfacial region as fast as the potential change is occurring. These slow processes are considered a general feature of RTILs [57].

A final point that should be discussed is the shape differences of the C-E curves for BDD and Au electrodes. Au electrodes exhibit a capacitance maximum at 0.3 V vs. Ag QRE with decreasing values at potentials positive and negative of the maximum. This shape is expected for by the Kornyshev theory [7,62,63]. Our results are consistent with the reported data in the literature [28,64]. In contrast, a U-shape C-E profile is seen for BDD with a defined minimum within -0.50 to -0.75 V vs. Ag QRE, depending on the RTIL.

Ions in RTILs are generally large and flexible, highly polarizable and chemically complex. Dispersion forces, dipole-dipole interactions, hydrogen bonding and π - π stacking can affect the structuring of RTILs at electrified interfaces in addition to Coulombic forces. RTILs are compressible. Given the total high ionic concentration (4 to 7 M) of RTILs as compared to aqueous or organic electrolytes (e.g. 0.1 M), lack of a molecular solvent to shield inter-ionic and electrode-ionic interactions, various non-Coulombic forces (hydrogen bonding, dispersive forces etc.) and large size of ions with asymmetry in size and shape, the classical Gouy-Chapman-Stern theory should not be applicable. However, various reports in the literature suggest similar behavior of RTILs and dilute aqueous electrolytes [18,24,25,29,50,65]. RTILs have been known to exist in dissociated ions/pairs strongly interacting with neighboring counterions [66,67]. The Shaw and Blanchard groups have independently identified the organization in RTILs extended over micro

scale into the bulk. This is consistent with the existence of paired ions and movement of one ion causes reorganization of neighboring ions acting as a template for ordered (crystal-like) phases [68–70].

A steady increase of capacitance is reported for potential > 0.5 V vs Ag/AgCl in aqueous electrolytes [71]. Adsorption of ions onto metal electrodes is known to produce maxima in the C-E curves [72,73]. This also results in frequency dispersion of the capacitance due to the slowness of the adsorption process and/or the diffusion of the surface-active species. Frequency-dependent C-E trends reveal that the system behaves like an aqueous electrolyte and follows GCS trend at very low frequencies and at high positive as well as negative potentials, ion adsorption is dominant. Low-frequency impedance data show that there is a slow adsorption/desorption process which dominates at very low frequencies. At more positive potentials, the density of accumulated holes at the diamond surface is expected to be very high. In this situation, the capacitance is no longer dominated anymore by solely electrochemical double layer but by the capacitance of the diamond electrode.

How RTIL ions interact with the electrode is also important to consider. Cations are known to form π -stacking and the alkyl chain predominantly orient perpendicular to the electrode [74]. The interfacial confinement of cations adjacent to the electrode dictates the capacitance. These results indicate specific adsorption of large, asymmetrical, and organic RMIM⁺ cations on the surface. Probe microscopy like in-situ STM and AFM results have also revealed that the innermost layer is tightly bound to the electrode and relatively large forces (~ 5 to 20 nN) are required to rupture them [75]. Lockett *et al.* probed the differential capacitance in the family of RTILs [C_(n=2,4,6)MIM][Cl] on GC electrode using EIS and CV [28,45] and found out that the cations show adsorption at the GC electrode and capacitance decreases with the length of alkyl chain. Alam et

al. [15,76] observed the similar preferential adsorption behavior of cations for RTILs, RMIMBF₄ (C_{n=2,6,8}MIM)/Hg interface using electrocapillary curves as a function of potential. The authors concluded that the long alkyl chains aggregate due to strong short-range interactions and form spatially heterogeneous hydrophobic domains at the interface. The anions prefer electrostatic interactions and hydrogen bonding with imidazolium ring and reside away from the electrode. Thus, the capacitance shows strong dependence on alkyl chain length of cations. The same group later showed that mixing [OMIM][BF₄] into [EMIM][BF₄] increased the capacitance, as longer alkyl chain dominates the overall capacitance [77]. These results imply the existence of Helmholtz-like one-ion thick layer that depends directly on the size of cation being adsorbed at the electrode surface and dictates the overall capacitance. The existence of inner (compact) layer is yet not clear from theoretical predictions. However, its existence has been validated by various surface spectroscopic and microscopic measurements like sum frequency generation (SFG) vibrational spectroscopy [17–19,78,79], scanning tunneling microscopy (STM), surface enhanced Raman spectroscopy (SERS), in-situ Fourier transform infrared (FTIR) absorption spectroscopy, and in-situ surface enhanced infrared adsorption spectroscopy (SEIRAS). Baldelli *et al.* used infrared spectroscopy to study interfacial structures and concluded that the orientation of imidazolium ring changes with respect to Pt electrode surface as a function of applied potential [18]. The imidazolium ring twists around C2 atom and allows the anion, [PF₆]⁻, to reach the electrode surface as positive potential is increased [17]. Additionally, the interfacial structure changes from one to approximately five layers exchanging [BF₄]⁻ or [PF₆]⁻ with [N(CN)₂]⁻ [18]. Gebbie *et al.* used direct surface force measurements and revealed the electrostatic screening of Au surface with BMIM⁺ enriched layers [67]. The authors argue that the well-defined polar and non-polar regions along with a lower degree of conformational flexibility of BMIM⁺ as compared to the anionic

assembly, $[\text{Tf}_2\text{N}]^-$ are responsible for specific adsorption of BMIM^+ at the electrode surface. Tokuda *et al.* attribute the persistent adsorption of BMIM^+ at both negative and positive potentials to favorable short-range van der Waals interactions with the electrode surface [80].

Preferential adsorption of large cations (alkyl chains and aromatic rings) has also been reported in aqueous electrolytes [81,82]. Absence of any solvent molecules in ionic liquids further increases the probability of this phenomenon in RTILs because of lack of charge screening by solvent molecules. This work brings light to a few considerations that are needed in uniting experiments and theory to understand the structure and properties of RTIL-electrode interfaces.

3.5 Conclusions

The potential-dependent capacitance of boron-doped nanocrystalline planar diamond (BDD) electrodes was investigated in two imidazolium-based RTILs over a 2-V potential window. The voltammetric behavior and capacitance-potential behavior were assessed using cyclic voltammetry, single-frequency impedance and broadband impedance techniques. The size of the cation and the viscosity were two differences in the RTILs. Capacitance values obtained from EIS and voltammetric data for $[\text{HMIM}][\text{PF}_6]$ and $[\text{BMIM}][\text{PF}_6]$ varied from 5.5 to 7.5 and 8.5 to 11 μFcm^{-2} , respectively. It was demonstrated that:

- (i) the theoretical C - E trend (bell- or camel-shape) as predicted by theory was obtained for an Au electrode but not for BDD. While Au exhibits a bell-shaped C - E curve with a capacitance maximum near 0.3 V vs. Ag QRE, BDD shows a slight U-shape trend with a capacitance minimum near -0.75 V vs. Ag QRE in both the RTILs.
- (ii) The arrangement of ions in the innermost layer to the BDD electrode makes major contribution to overall capacitance. Shorter alkyl chain in the cationic component of imidazolium-based RTILs

gives higher capacitance. This shows that the C-E trends are dictated not only by the electrode material but also by the inherent properties of RTILs (size of ions, viscosity, dielectric constants, concentrations, etc.).

(iii) Minimal capacitive hysteresis observed in the C-E trends, when the direction of potential scan was reversed confirms the stability of BDD microstructure and surface chemistry over the 2-V potential window.

(iv) The C-E trends constructed from single frequency impedance measurements produced qualitatively similar trends as those obtained using EIS. However, the magnitude of capacitance exhibits a significant dispersion with the frequency. Potential dependence of capacitance was observed only at careful selection of lower frequencies (< 10 Hz) that reveal a distinct U-shape trend with a minimum at -0.5 V vs. Ag QRE with increasing capacitance on both sides of the minimum. This indicates that RTILs respond very slowly to the potential perturbation.

3.6 Acknowledgements

The research was made possible by a grant from the Army Research Office (ARO) through contract W911NF-14-1-0063. K.B. kindly thanks Jens Wallauer and Dr. Marcel Drüscher (rhd Instruments GmbH & Co. KG) for providing access to RelaxIS software and for helpful discussions.

REFERENCES

REFERENCES

- [1] M. Armand, F. Endres, D.R. MacFarlane, H. Ohno, B. Scrosati, Ionic-liquid materials for the electrochemical challenges of the future, *Nat. Mater.* 8 (2009) 621–629. doi:10.1038/nmat2448.
- [2] M. Galiński, A. Lewandowski, I. Stepniak, Ionic liquids as electrolytes, *Electrochim. Acta.* 51 (2006) 5567–5580. doi:10.1016/j.electacta.2006.03.016.
- [3] P. Hapiot, C. Lagrost, Electrochemical reactivity in room-temperature ionic liquids, *Chem. Rev.* 108 (2008) 2238–2264. doi:10.1021/cr0680686.
- [4] Z. Wang, M. Guo, X. Mu, S. Sen, T. Insley, A.J. Mason, P. Král, X. Zeng, Highly Sensitive Capacitive Gas Sensing at Ionic Liquid-Electrode Interfaces, *Anal. Chem.* 88 (2016) 1959–1964. doi:10.1021/acs.analchem.5b04677.
- [5] X. Mu, Z. Wang, X. Zeng, A.J. Mason, A robust flexible electrochemical gas sensor using room temperature ionic liquid, *IEEE Sens. J.* 13 (2013) 3976–3981. doi:10.1109/JSEN.2013.2262932.
- [6] I. Borukhov, D. Andelman, H. Orland, Steric Effects in Electrolytes: A Modified Poisson-Boltzmann Equation, *Phys. Rev. Lett.* 79 (1997) 435–438. doi:10.1103/PhysRevLett.79.435.
- [7] A.A. Kornyshev, Double-Layer in Ionic Liquids: Paradigm Change?, *J. Phys. Chem. B.* 111 (2007) 5545–5557. doi:10.1021/jp067857o.
- [8] K.B. Oldham, A Gouy-Chapman-Stern model of the double layer at a metal/ionic liquid interface, *J. Electroanal. Chem.* 613 (2008) 131–138. doi:10.1016/j.jelechem.2007.10.017.
- [9] J.P. Zheng, P.C. Goonetilleke, C.M. Pettit, D. Roy, Probing the electrochemical double layer of an ionic liquid using voltammetry and impedance spectroscopy: A comparative study of carbon nanotube and glassy carbon electrodes in [EMIM]+[EtSO₄]⁻, *Talanta.* 81 (2010) 1045–1055. doi:10.1016/j.talanta.2010.01.059.
- [10] L. Siinor, J. Poom, C. Siimenson, K. Lust, E. Lust, Electrochemical characteristics pyrolytic graphite|mixture of 1-ethyl-3-methylimidazolium tetrafluoroborate and 1-ethyl-3-methylimidazolium iodide interface, *J. Electroanal. Chem.* 719 (2014) 133–137. doi:10.1016/j.jelechem.2014.01.035.
- [11] N. Nishi, S. Yasui, A. Hashimoto, T. Sakka, Anion dependence of camel-shape capacitance at the interface between mercury and ionic liquids studied using pendant drop method, *J. Electroanal. Chem.* 789 (2017) 108–113. doi:10.1016/j.jelechem.2017.02.001.

- [12] D.J. Bozym, B. Uralcan, D.T. Limmer, M.A. Pope, N.J. Szamreta, P.G. Debenedetti, I.A. Aksay, Anomalous Capacitance Maximum of the Glassy Carbon-Ionic Liquid Interface through Dilution with Organic Solvents, *J. Phys. Chem. Lett.* 6 (2015) 2644–2648. doi:10.1021/acs.jpcclett.5b00899.
- [13] L. Siinor, C. Siimenson, K. Lust, E. Lust, Mixture of 1-ethyl-3-methylimidazolium tetrafluoroborate and 1-ethyl-3-methylimidazolium iodide: A new potential high capacitance electrolyte for EDLCs, *Electrochem. Commun.* (2013). doi:10.1016/j.elecom.2013.07.023.
- [14] R. Costa, C.M. Pereira, F. Silva, Double layer in room temperature ionic liquids: influence of temperature and ionic size on the differential capacitance and electrocapillary curves, *Phys Chem Chem Phys.* 12 (2010) 11125–11132. doi:10.1039/c003920a.
- [15] M.T. Alam, M.M. Islam, T. Okajima, T. Ohsaka, Ionic liquid structure dependent electrical double layer at the mercury interface, *J. Phys. Chem. C.* 112 (2008) 2601–2606. doi:10.1021/jp7098043.
- [16] F. Silva, C. Gomes, M. Figueiredo, R. Costa, A. Martins, C.M. Pereira, The electrical double layer at the [BMIM][PF₆] ionic liquid/electrode interface - Effect of temperature on the differential capacitance, *J. Electroanal. Chem.* 622 (2008) 153–160. doi:10.1016/j.jelechem.2008.05.014.
- [17] S. Rivera-Rubero, S. Baldelli, Surface spectroscopy of room-temperature ionic liquids on a platinum electrode: A sum frequency generation study, *J. Phys. Chem. B.* 108 (2004) 15133–15140. doi:10.1021/jp048260g.
- [18] S. Baldelli, Surface structure at the ionic liquid-electrified metal interface, *Acc. Chem. Res.* 41 (2008) 421–431. doi:10.1021/ar700185h.
- [19] S. Baldelli, Probing Electric Fields at the Ionic Liquid - Electrode Interface Using Sum Frequency Generation Spectroscopy and Electrochemistry, (2005) 13049–13051.
- [20] V.O. Santos, M.B. Alves, M.S. Carvalho, P.A.Z. Suarez, J.C. Rubim, Surface-Enhanced Raman Scattering at the Silver Electrode / Ionic Liquid (BMIPF 6), *J. Phys. Chem. B.* 110 (2006) 20379–20385. doi:10.1021/jp0643348.
- [21] S.M. Mahurin, S.P. Surwade, Probing the interaction of ionic liquids with graphene using surface-enhanced Raman spectroscopy, (2015) 585–590. doi:10.1002/jrs.4858.
- [22] N. Nanbu, Y. Sasaki, F. Kitamura, In situ FT-IR spectroscopic observation of a room-temperature molten salt | gold electrode interphase, *Electrochem. Commun.* 5 (2003) 383–387. doi:10.1016/S1388-2481(03)00073-0.
- [23] K. Motobayashi, K. Minami, N. Nishi, T. Sakka, M. Osawa, Hysteresis of potential-dependent changes in ion density and structure of an ionic liquid on a gold electrode: In situ

- observation by surface-enhanced infrared absorption spectroscopy, *J. Phys. Chem. Lett.* 4 (2013) 3110–3114. doi:10.1021/jz401645c.
- [24] M.T. Alam, M.M. Islam, T. Okajima, T. Ohsaka, Capacitance measurements in a series of room-temperature ionic liquids at glassy carbon and gold electrode interfaces, *J. Phys. Chem. C* 112 (2008) 16600–16608. doi:10.1021/jp804620m.
- [25] M.T. Alam, M. Mominul Islam, T. Okajima, T. Ohsaka, Measurements of differential capacitance in room temperature ionic liquid at mercury, glassy carbon and gold electrode interfaces, *Electrochem. Commun.* 9 (2007) 2370–2374. doi:10.1016/j.elecom.2007.07.009.
- [26] T.R. Gore, T. Bond, W. Zhang, R.W.J. Scott, I.J. Burgess, Hysteresis in the measurement of double-layer capacitance at the gold-ionic liquid interface, *Electrochem. Commun.* 12 (2010) 1340–1343. doi:10.1016/j.elecom.2010.07.015.
- [27] C. Gomes, R. Costa, C.M. Pereira, a. F. Silva, The electrical double layer at the ionic liquid/Au and Pt electrode interface, *RSC Adv.* 4 (2014) 28914. doi:10.1039/C4RA03977G.
- [28] V. Lockett, M. Horne, R. Sedev, T. Rodopoulos, J. Ralston, Differential capacitance of the double layer at the electrode/ionic liquids interface, *Phys Chem Chem Phys.* 12 (2010) 12499–12512. doi:10.1039/c0cp00170h.
- [29] M.M. Islam, M.T. Alam, T. Ohsaka, Electrical Double-Layer Structure in Ionic Liquids: A Corroboration of the Theoretical Model by Experimental Results, *J. Phys. Chem. C* 112 (2008) 16568–16574. doi:10.1021/jp8058849.
- [30] C. Cannes, H. Cachet, C. Debiemme-Chouvy, C. Deslouis, J. de Sanoit, C. Le Naour, V. a Zinovyeva, Double Layer at [BuMeIm][Tf 2 N] Ionic Liquid–Pt or –C Material Interfaces, *J. Phys. Chem. C* 117 (2013) 22915–22925. doi:10.1021/jp407665q.
- [31] M.M. Islam, M.T. Alam, T. Okajima, T. Ohsaka, Electrical double layer structure in ionic liquids: An understanding of the unusual capacitance-potential curve at a nonmetallic electrode, *J. Phys. Chem. C* 113 (2009) 3386–3389. doi:10.1021/jp8114447.
- [32] J. Zhang, A.M. Bond, Practical Considerations Associated with Voltammetric Studies in Room Temperature Ionic Liquids, *Analyst.* 130 (2005) 1132–47. doi:10.1039/b504721h.
- [33] R. Jarošová, P.M. De Sousa Bezerra, C. Munson, G.M. Swain, Assessment of heterogeneous electron-transfer rate constants for soluble redox analytes at tetrahedral amorphous carbon, boron-doped diamond, and glassy carbon electrodes, *Phys. Status Solidi Appl. Mater. Sci.* 213 (2016) 2087–2098. doi:10.1002/pssa.201600339.
- [34] A. Tafel, M. Wu, E. Spiecker, P. Hommelhoff, J. Ristein, Fabrication and structural characterization of diamond-coated tungsten tips, (2019). <http://arxiv.org/abs/1902.01369>.
- [35] N. Wächter, C. Munson, R. Jarošová, I. Berkun, T. Hogan, R.C. Rocha-Filho, G.M. Swain,

- Structure, Electronic Properties, and Electrochemical Behavior of a Boron-Doped Diamond/Quartz Optically Transparent Electrode, *ACS Appl. Mater. Interfaces*. (2016) A-M. doi:10.1021/acsami.6b02467.
- [36] L.M. Fischer, M. Tenje, A.R. Heiskanen, N. Masuda, J. Castillo, A. Bentien, J. Émneus, M.H. Jakobsen, A. Boisen, Gold cleaning methods for electrochemical detection applications, *Microelectron. Eng.* 86 (2009) 1282–1285. doi:10.1016/j.mee.2008.11.045.
- [37] R. Jarosova, G.M. Swain, Rapid Preparation of Room Temperature Ionic Liquids with Low Water Content as Characterized with a ta-C:N Electrode, *J. Electrochem. Soc.* 162 (2015) H507–H511. doi:10.1149/2.0191508jes.
- [38] M.C. Granger, M. Witek, J. Xu, J. Wang, M. Hupert, A. Hanks, M.D. Koppang, J.E. Butler, G. Lucazeau, M. Mermoux, J.W. Strojek, G.M. Swain, Standard electrochemical behavior of high-quality, boron-doped polycrystalline diamond thin-film electrodes, *Anal. Chem.* 72 (2000) 3793–3804. doi:10.1021/ac0000675.
- [39] J. Wallauer, M. Balabajew, B. Roling, Impedance Spectroscopy on Electrode | Ionic Liquid Interfaces, 2017. doi:10.1002/9783527682706.ch11.
- [40] H. Tokuda, S. Tsuzuki, M.A.B.H. Susan, K. Hayamizu, M. Watanabe, How ionic are room-temperature ionic liquids? An indicator of the physicochemical properties, *J. Phys. Chem. B.* 110 (2006) 19593–19600. doi:10.1021/jp064159v.
- [41] T. Buffeteau, J. Grondin, J.-C. Lassègues, Infrared Spectroscopy of Ionic Liquids: Quantitative Aspects and Determination of Optical Constants, *Appl. Spectrosc.* 64 (2010) 112–119. doi:10.1366/000370210790572089.
- [42] M.C. Buzzeeo, C. Hardacre, R.G. Compton, Extended electrochemical windows made accessible by room temperature ionic liquid/organic solvent electrolyte systems, *ChemPhysChem.* 7 (2006) 176–180. doi:10.1002/cphc.200500361.
- [43] R.S. Anareddy, A.J. Lucio, S.K. Shaw, Adventitious Water Sorption in a Hydrophilic and a Hydrophobic Ionic Liquid: Analysis and Implications, (2016). doi:10.1021/acsomega.6b00104.
- [44] M.C. Kroon, W. Buijs, C.J. Peters, G.J. Witkamp, Decomposition of ionic liquids in electrochemical processing, *Green Chem.* 8 (2006) 241–245. doi:10.1039/b512724f.
- [45] V. Lockett, R. Sedev, J.R. Horne, T. Rodopoulos, Differential Capacitance of the Electrical Double Layer in Imidazolium-Based Ionic Liquids : Influence of Potential , Cation Size , and Temperature Differential Capacitance of the Electrical Double Layer in Imidazolium-Based Ionic Liquids : Influence of P, (2008) 7486–7495. doi:10.1021/jp7100732.
- [46] R. Atkin, N. Borisenko, M. Drüschler, F. Endres, R. Hayes, B. Huber, B. Roling, Structure and dynamics of the interfacial layer between ionic liquids and electrode materials, *J. Mol.*

- Liq. 192 (2014) 44–54. doi:10.1016/j.molliq.2013.08.006.
- [47] A.J. Lucio, S.K. Shaw, Effects and controls of capacitive hysteresis in ionic liquid electrochemical measurements, *Analyst*. 143 (2018) 4887–4900. doi:10.1039/c8an01085d.
 - [48] K.D. Gnahn M, Pajkossy T, The interface between Au(111) and an ionic liquid, *Electrochim. Acta*. 55 (2010) 6212–6217. doi:10.1016/j.electacta.2009.08.031.
 - [49] M. Balabajew, B. Roling, Minimizing Artifacts in Three-electrode Double Layer Capacitance Measurements Caused by Stray Capacitances, *Electrochim. Acta*. 176 (2015) 907–918. doi:10.1016/j.electacta.2015.07.074.
 - [50] A.J. Lucio, S.K. Shaw, J. Zhang, A.M. Bond, Double-Layer Capacitance at Ionic Liquid-Boron-Doped Diamond Electrode Interfaces Studied by Fourier Transformed Alternating Current Voltammetry, *J. Phys. Chem. C*. 122 (2018) 11777–11788. doi:10.1021/acs.jpcc.8b00272.
 - [51] M. Drüscher, B. Huber, S. Passerini, B. Roling, Hysteresis effects in the potential-dependent double layer capacitance of room temperature ionic liquids at a polycrystalline platinum interface, *J. Phys. Chem. C*. 114 (2010) 3614–3617. doi:10.1021/jp911513k.
 - [52] M. Drüscher, B. Huber, B. Roling, On capacitive processes at the interface between 1-Ethyl-3-methylimidazolium tris(pentafluoroethyl)trifluorophosphate and Au(111), *J. Phys. Chem. C*. 115 (2011) 6802–6808. doi:10.1021/jp200395j.
 - [53] A. Uysal, H. Zhou, G. Feng, S.S. Lee, S. Li, P. Fenter, P.T. Cummings, P.F. Fulvio, S. Dai, J.K. McDonough, Y. Gogotsi, Structural origins of potential dependent hysteresis at the electrified graphene/ionic liquid interface, *J. Phys. Chem. C*. 118 (2014) 569–574. doi:10.1021/jp4111025.
 - [54] C. Pinilla, M.G. Del Pópolo, J. Kohanoff, R.M. Lynden-Bell, Polarization relaxation in an ionic liquid confined between electrified walls, *J. Phys. Chem. B*. 111 (2007) 4877–4884. doi:10.1021/jp067184.
 - [55] A.J. Lucio, S.K. Shaw, Capacitive hysteresis at the 1-ethyl-3-methylimidazolium tris(pentafluoroethyl)-trifluorophosphate–polycrystalline gold interface, *Anal. Bioanal. Chem.* (2018) 1–12. doi:10.1007/s00216-018-0962-5.
 - [56] A.J. Lucio, S.K. Shaw, J. Zhang, A.M. Bond, Double Layer Capacitance at Ionic Liquid - Boron Doped Diamond Electrode Interfaces Studied by Fourier Transformed Alternating Current Voltammetry, *J. Phys. Chem. C*. (2018). doi:10.1021/acs.jpcc.8b00272.
 - [57] Y. Yasui, Y. Kitazumi, H. Mizunuma, N. Nishi, T. Kakiuchi, Comparison of the Ultraslow Relaxation Processes at the Ionic Liquid|Water Interface for Three Hydrophobic Ionic Liquids, *Electrochem. Commun.* 12 (2010) 1479–1482. doi:10.1016/j.elecom.2010.08.011.

- [58] T. Pajkossy, Impedance spectroscopy at interfaces of metals and aqueous solutions - Surface roughness, CPE and related issues, *Solid State Ionics*. 176 (2005) 1997–2003. doi:10.1016/j.ssi.2004.06.023.
- [59] A.J. Lucio, S.K. Shaw, J. Zhang, A.M. Bond, Large-Amplitude Fourier-Transformed AC Voltammetric Study of the Capacitive Electrochemical Behavior of the 1-Butyl-3-methylimidazolium Tetrafluoroborate-Polycrystalline Gold Electrode Interface, *J. Phys. Chem. C*. 121 (2017) 12136–12147. doi:10.1021/acs.jpcc.7b00287.
- [60] S. Bi, R. Wang, S. Liu, J. Yan, B. Mao, A.A. Kornyshev, G. Feng, Minimizing the electrosorption of water from humid ionic liquids on electrodes, *Nat. Commun.* 9 (2018) 1–9. doi:10.1038/s41467-018-07674-0.
- [61] A.M. O'Mahony, D.S. Silvester, L. Aldous, C. Hardacre, R.G. Compton, Effect of water on the electrochemical window and potential limits of room-temperature ionic liquids, *J. Chem. Eng. Data*. 53 (2008) 2884–2891. doi:10.1021/je800678e.
- [62] M. V. Fedorov, A.A. Kornyshev, Ionic liquids at electrified interfaces, *Chem. Rev.* 114 (2014) 2978–3036. doi:10.1021/cr400374x.
- [63] N. Georgi, A.A. Kornyshev, M. V. Fedorov, The anatomy of the double layer and capacitance in ionic liquids with anisotropic ions: Electrostriction vs. lattice saturation, *J. Electroanal. Chem.* 649 (2010) 261–267. doi:10.1016/j.jelechem.2010.07.004.
- [64] Y.Z. Su, Y.C. Fu, J.W. Yon, Z. Bin Chen, B.W. Mao, Double layer of Au(100)/ionic liquid interface and its stability in imidazolium-based ionic liquids, *Angew. Chemie - Int. Ed.* 48 (2009) 5148–5151. doi:10.1002/anie.200900300.
- [65] A.J. Lucio, S.K. Shaw, J. Zhang, A.M. Bond, Large-Amplitude Fourier-Transformed AC Voltammetric Study of the Capacitive Electrochemical Behavior of the 1-Butyl-3-methylimidazolium Tetrafluoroborate-Polycrystalline Gold Electrode Interface, *J. Phys. Chem. C*. 121 (2017) 12136–12147. doi:10.1021/acs.jpcc.7b00287.
- [66] L.-B.R. Perkin Susan, Salanne Mathieu, Madden Paul, Is a Stern and diffuse layer model appropriate to ionic liquids at surfaces ?, *Proc. Natl. Acad. Sci. U. S. A.* 110 (2013) 4121. doi:10.1073/pnas.1314188110.
- [67] M.A. Gebbie, M. Valtiner, X. Banquy, E.T. Fox, W.A. Henderson, J.N. Israelachvili, Ionic liquids behave as dilute electrolyte solutions, *Proc Natl Acad Sci U S A.* 110 (2013) 9674–9679. doi:10.1073/pnas.1307871110.
- [68] K. Ma, R. Jarosova, G.M. Swain, G.J. Blanchard, Charge-Induced Long-Range Order in a Room-Temperature Ionic Liquid, *Langmuir*. 32 (2016) 9507–9512. doi:10.1021/acs.langmuir.6b02639.
- [69] R. Jarosova, G.M. Swain, G.J. Blanchard, Modulation of an Induced Charge Density

- Gradient in the Room- Temperature Ionic Liquid [BMIM]⁺[BF₄]⁻, (2018). doi:10.1021/acs.jpcc.8b02345.
- [70] R.S. Anareddy, S.K. Shaw, Developing Distinct Chemical Environments in Ionic Liquid Films, *J. Phys. Chem. C* 122 (2018) 19731–19737. doi:10.1021/acs.jpcc.8b06608.
- [71] J.A. Garrido, S. Nowy, A. Härtl, M. Stutzmann, The diamond/aqueous electrolyte interface: An impedance investigation, *Langmuir* 24 (2008) 3897–3904. doi:10.1021/la703413y.
- [72] T. Pajkossy, T. Wandlowski, D.M. Kolb, Impedance aspects of anion adsorption on gold single crystal electrodes, *J. Electroanal. Chem.* 414 (1996) 209–220. doi:10.1016/0022-0728(96)04700-6.
- [73] T. Pajkossy, D.M. Kolb, Double layer capacitance of Pt(111) single crystal electrodes, *Electrochim. Acta* 46 (2001) 3063–3071. doi:10.1016/S0013-4686(01)00597-7.
- [74] S. Jo, S.W. Park, Y. Shim, Y.J. Jung, Effects of Alkyl Chain Length on Interfacial Structure and Differential Capacitance in Graphene Supercapacitors: A Molecular Dynamics Simulation Study, *Electrochim. Acta* 247 (2017) 634–645. doi:10.1016/j.electacta.2017.06.169.
- [75] F. Endres, N. Borisenko, S.Z. El Abedin, R. Hayes, R. Atkin, The interface ionic liquid(s)/electrode(s): In situ STM and AFM measurements, *Faraday Discuss.* 154 (2012) 221–233. doi:10.1039/c1fd00050k.
- [76] M.T. Alam, M.M. Islam, T. Okajima, T. Ohsaka, Measurements of differential capacitance at mercury/room-temperature ionic liquids interfaces, *J. Phys. Chem. C* 111 (2007) 18326–18333. doi:10.1021/jp075808l.
- [77] M.T. Alam, M.M. Islam, T. Okajima, T. Ohsaka, Electrical Double Layer in Mixtures of Room-Temperature Ionic Liquids, *J. Phys. Chem. C* 113 (2009) 6596–6601. doi:10.1021/jp810865t.
- [78] C.Y. Peñalber, Sum Frequency Generation Spectroscopy of Imidazolium based Ionic Liquids with Cyano functionalized Anions at Gas Liquid and Solid Liquid Interfaces, 2012.
- [79] C. Aliaga, S. Baldelli, D. Interface, Sum Frequency Generation Spectroscopy and Double-Layer Capacitance Studies of the 1-Butyl-3-Methylimidazolium Dicyanamide – Platinum Interface Sum Frequency Generation Spectroscopy and Double-Layer Capacitance Studies of the, *Society*. (2006) 18481–18491. doi:10.1021/jp063476z.
- [80] H. Tokuda, K. Hayamizu, K. Ishii, M.A.B.H. Susan, M. Watanabe, Physicochemical properties and structures of room temperature ionic liquids. 2. variation of alkyl chain length in imidazolium cation, *J. Phys. Chem. B* 109 (2005) 6103–6110. doi:10.1021/jp044626d.
- [81] J. Lipxowsxl, L. Sttolberg, D.G. Ya, B.P. Ger, S. Mirwald, F.H.E. Gle, *Molecular*

Adsorption At Metal Electrodes, *Electrochim. Acta.* 39 (1994) 1045–1056.

- [82] C. Cachet, M. Keddam, V. Mariotte, R. Wiart, Adsorption of perfluorinated surfactants on gold electrodes-II. Behaviour of ionic compounds, *Electrochim. Acta.* 38 (1993) 2203–2208. doi:10.1016/0013-4686(93)80099-L.

Chapter 4

The Effect of Surface Oxygen on the Wettability and Electrochemical Properties of Boron-Doped Nanocrystalline Diamond Electrodes in Room Temperature Ionic Liquids

4.1 Introduction

Ionic liquids are essentially molten salts at room temperature (RTILs). They are a very interesting class of liquids offering key advantages over organic solvent/electrolyte solutions such as low vapor pressure, non-flammability, electrochemical and chemical stability and ionic conductivity [1–5]. The availability of a wide range of compositionally distinct RTILs makes tuning their electrochemical properties possible. RTILs are generally comprised of a large asymmetric organic cation and a small symmetric inorganic anion. They are totally ionic with no solvent separating the ions. Coulombic interactions are the dominant force between the ions. With no dielectric solvent, the constituent ions do not exist as simple spherical charges [6]. Rather, the ions exist as ion pairs. From a fundamental electrochemical perspective, the use of RTILs allows one to investigate electron-transfer kinetics and redox reaction mechanisms of soluble redox systems in the absence of a solvent as the solvation shell around a redox molecule. Indeed, electron transfer reactions in an RTIL will necessarily be very different from that in a polar solvent/electrolyte system. The short- and long-range organization of the RTIL ions at an electrified interface as well as their unique solvation environment around a redox molecule make the electrochemical properties of these novel media interesting to study [6]. The chemical and electrochemical stability of RTILs leads to large voltammetric working potential windows of 4 to 6 V, depending on the RTIL cation and anion. Applications of RTILs in electrochemistry, tribology, etc. will be influenced by the arrangement of the ions at the electrified interface between

the RTIL and the solid surface, and their physicochemical properties (*e.g.*, electrical conductivity and viscosity).

Boron-doped diamond (BDD) is a new type of carbon electrode that possesses a number of advantageous properties for electrochemical measurements [7–11]. These electrodes are generally hydrogen-terminated when deposited by chemical vapor deposition (CVD) using a methane/hydrogen source gas mixture [7–11]. However, the surface can be easily converted to, for example, an oxygen-termination by exposing the film to an O₂ radio frequency (RF) plasma, electrochemical oxidation or by boiling in strong acids [12–15]. The background voltammetric current and potential-dependent capacitance of BDD electrodes are influenced by the film microstructure and bulk electronic properties. The latter arise from the substitutionally-inserted boron atoms from doping [7,9] and the hydrogen incorporation [16,17]. Furthermore, these electrochemical properties are linked to the electrode surface area, any porosity that exists, the ion accessibility to these pores and the electrolyte/solvent properties. Two other factors that can influence the background voltammetric current and capacitance of BDD electrodes is the fraction of sp² carbon impurity exposed and the surface chemistry, which should affect the ability of an electrolyte solution to wet the electrode surface [18–20]. The wetting behavior of an electrolyte solution can be assessed through contact angle measurements. A smaller contact angle corresponds to a higher degree of surface wetting.

Surface modification of carbon electrodes using RF plasma treatment is an effective way of introducing functional groups to modulate the wettability [21–24]. O₂ plasma treatment of carbon electrodes often causes morphological damage as well as surface chemistry changes [23,24]. Roughening and carbon corrosion can occur due to gasification reactions (CO and CO₂ production) mediated by atomic oxygen produced in the plasma. Such deleterious effects can be

mitigated by controlling treatment parameters such as plasma power, source gas pressure, treatment time, etc. [21].

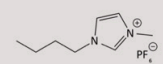
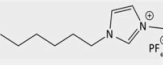
There has been limited work published on the electrochemical behavior of BDD electrodes in RTILs. For example, Zhao *et al.* reported on the working potential window, background voltammetric current magnitude and cyclic voltammetric behavior of ferrocene and cobaltocenium hexafluorophosphate at BDD, glassy carbon, Pt and Au electrodes in multiple protic ionic liquids [25]. The authors also discussed the importance of water impurity and its effect on background current, potential window and diffusional mass transport of the redox systems. Cannes *et al.* reported on the capacitance of BDD, glassy carbon and carbon nitride electrodes in 1-butyl-3-methylimidazolium bis(trifluoromethylsulfonyl)imide [BMIM][Tf₂N] [26]. The capacitance was measured at elevated temperatures and values for BDD were rather high in excess of 100 $\mu\text{F cm}^{-2}$. Ernst *et al.* reported on the reduction of dissolved O₂ at BDD and glassy carbon electrodes in 1-ethyl-3-methylimidazolium bis (trifluoromethylsulfonyl)imide [BMIM][Tf₂N] [27]. The reduction reaction involved the 1e⁻ reduction to the super oxide radical anion. More sluggish electron-transfer kinetics were observed on BDD, as compared to glassy carbon. The sluggish kinetics were attributed to a lower density of electronic states in BDD. Lucio *et al.* reported on the double layer capacitance of BDD electrodes in several RTILs including [BMIM][BF₄] and [BMIM][PF₆] [28]. Capacitance values ranged from 4-8 $\mu\text{F cm}^{-2}$ over the potential range probed in both RTILs. Li *et al.* used Fourier transformed large-amplitude alternating current voltammetry to measure the heterogeneous electron-transfer rate constant for the ferrocene/ferrocenium redox couple in [BMIM][PF₆] on BDD surfaces and cut edges rich in sp² carbon [19]. k^o values on the BDD surface were $1.5 \times 10^{-3} \text{ cm s}^{-1}$. Faster kinetics were observed on the sp² carbon-rich sites. The authors noted

that nonuniform electrode activity is more observable in RTILs due to the slower diffusional time scale.

Other BDD electrode work includes determination of the heterogeneous electron-transfer rate constant for electron-transfer rate constants were determined for ferrocene and ferrocene carboxylic acid (FCA) in [BMIM][BF₄] [29], voltammetric studies of phenolic compound oxidation in an ionic liquid [30], and electrochemical studies of high surface area diamond-coated Si tips in ionic liquids [31].

In this chapter, an investigation is reported on about how the surface chemistry (H vs. O) of boron-doped nanocrystalline diamond thin-film electrodes (referred to as BDD) affects the wettability, background voltammetric current, working potential window and potential-dependent capacitance in two different RTILs: 1-butyl-3-methylimidazolium hexafluorophosphate, [BMIM][PF₆] and 1-hexyl-3-methylimidazolium hexafluorophosphate, [HMIM][PF₆]. Comparison measurements were performed in an aqueous electrolyte, 0.5 mol L⁻¹ H₂SO₄. Cyclic voltammetry and electrochemical impedance spectroscopy were used to study current density-potential (*j*-*E*) and capacitance-potential (*C*-*E*) trends. The physical properties of the two RTILs used are given in Table 4.1.

Table 4.1. Physical properties of [BMIM][PF₆] and [HMIM][PF₆] at 25°C.

| RTIL | Molecular Structure | Mol. Wt. (g mol ⁻¹) | Viscosity (η, cP) | Ionic Conductivity (σ, mS cm ⁻¹) | Dielectric Constant (ε) | Density (ρ, g cm ⁻³) | Ionic Concentration (mol L ⁻¹) |
|--------------------------|---|---------------------------------|-------------------|--|-------------------------|----------------------------------|--|
| [BMIM][PF ₆] |  | 219.12 | 267 | 1.92 | 11.4 | 1.37 | 6 |
| [HMIM][PF ₆] |  | 312.24 | 465 | 0.80 | 8.9 | 1.30 | 4 |

Data were provided by the chemical supplier IoLiTec.

4.2 Materials and Methods

4.2.1 Boron-Doped Diamond Electrodes

The boron-doped nanocrystalline diamond (BDD) thin-films were grown on a p-Si (111) substrate (Virginia Semiconductor, Inc. Fredricksburg, VA, $\sim 0.001 \Omega\text{-cm}$) by microwave-assisted chemical vapor deposition (CVD). A commercial 1.5 kW reactor (Seki Technotron) was used [44]. The silicon substrate was seeded ultrasonically with nanodiamond particles from an “Opal Seed” suspension (Adamas Nanotechnologies Inc., Raleigh, NC) for 30 min in a glass beaker. This suspension contains aggregates ($\sim 30 \text{ nm}$) of detonation nanodiamond particles in dimethyl sulfoxide (DMSO). The seeded substrate was then rinsed 3x with ultrapure water in the beaker followed by wick-drying using a Kimwipe and full drying with a stream of N_2 before being placed in the CVD reactor for overnight pump-down. The BDD film was grown using methane diluted in hydrogen ($\text{C/H} = 1\%$, v/v) at a total gas flow rate of 200 sccm (standard cubic centimeter per minute), a system pressure of 35 Torr, an estimated substrate temperature near 825°C using a disappearing filament optical pyrometer, and a growth time of 5-6 h. Boron doping was accomplished by adding 0.1% (v/v) diborane mixed with hydrogen to the source gas mixture, producing a gas-phase boron concentration of 10 ppm. After deposition, the methane and diborane flows were stopped, and the coated substrate was cooled in a hydrogen plasma for 30 min by slowly reducing the power and pressure down to 150 W and 10 Torr. This post-growth cooling step is critical to minimize the formation of sp^2 -bonded carbon at the surface that would result from the desorption of surface hydrogen ($T \sim 450^\circ\text{C}$) and reconstruction of the surface carbon atoms if the plasma was extinguished (hard shutdown) at the growth temperature [33]. The cooling step in atomic hydrogen is also critical for maintaining a hydrogen-terminated surface [34]. The doping level was estimated to be in the low 10^{21} cm^{-3} range, based on Raman spectroscopy and

Hall effect measurement data of other films deposited using similar conditions [34]. Film thicknesses were 2 - 4 μm , as estimated by the change in weight of the substrate after film deposition and cross-sectional scanning electron micrographs.

4.2.2 Surface Termination of the BDD Films

Hydrogen microwave plasma treatment was used to produce a low-oxygen BDD surface. This was accomplished with a 200 sccm flow of ultrapure hydrogen for a total of 30 min at 800 W. The films were cooled to an estimated temperature of less than 400 $^{\circ}\text{C}$ by slowly reducing the pressure and power over the last 10 min of the treatment [35–37]. These films are referred to as “H-BDD” in the text. A radio frequency (RF) plasma generator (PDC-32G, Harrick Scientific) operating at 18 W was used to produce moderate- and high-oxygen BDD surfaces by exposing them to an Ar or O_2 plasma, respectively. The films were placed in the center of the pyrex reaction chamber that was connected to a mechanical pump and an ultrapure gas feed (Ar or O_2). The samples were plasma treated under static conditions for 12 min using a pressure of 300 mTorr. This was achieved by repeating the following process 3x: full evacuation of the chamber, closing the exhaust valve, and then filling the chamber to desired pressure with the gas. The films with moderate and high oxygen surface coverages are referred to as “Ar-BDD” and “O-BDD”, respectively, in the text.

4.2.3 Chemicals

Ultrapure grade sulfuric acid (99.999%), CAS- 339741, was obtained from Sigma-Aldrich. The RTILs, 1-butyl-3-methylimidazolium hexafluorophosphate [BMIM][PF₆] (IL-0011-UP) and

1-hexyl-3-methylimidazolium hexafluorophosphate [HMIM][PF₆] (IL-0018-UP), were procured from a commercial source (IoLiTec, Tuscaloosa, AL, specified as $\geq 99.5\%$ purity with water content below 100 ppm). The RTILs were purified using a protocol described previously [38]. In short, the ‘as-received’ RTIL was stored over activated carbon (Sigma-Aldrich) for 5 days with occasional stirring. This step removes organic contaminants through adsorption onto the carbon. The RTIL was then withdrawn through a 0.2 μm Teflon syringe filter (Whatman) directly injected into the electrochemical cell. The RTIL was then heated to 70 °C for 1 h while being continuously sparged with ultrapure Ar gas (99.9999 %) (so-called sweeping treatment) [38]. All processes were performed in a dry N₂-purged vinyl glove box (Coy Laboratories). The water content in the RTIL after the sweeping treatment was below 100 ppm, as estimated using thermogravimetric analysis. The mass loss recorded during a temperature scan up to 300 °C was assumed to be due to water loss. The ultrapure water was obtained from a Barnstead E-pure System (Thermo Scientific, USA) filtered through a Milli-Q deionized water purification system with a resistivity $>17\text{ M}\Omega\text{-cm}$.

4.2.4 X-ray Photoelectron Spectroscopy (XPS)

The chemical composition of the BDD films in the near-surface region was determined using X-ray photoelectron spectroscopy (XPS). Spectra were recorded using a Perkin-Elmer PHI 5400 ESCA system with a high-intensity monochromatic X-ray source (Al K α). Samples were analyzed at a base pressure of 10^{-9} Torr with a take-off angle of 45 ° using a pass energy of 29.35 eV. The X-ray power was 350 W and spectra were collected from a spot size *ca.* 250 μm^2 area. The instrument was calibrated using the C1s peak for HOPG (C=C sp², highly ordered pyrolytic graphite) at 284.5 eV as an internal reference. The atomic percentage of each element was calculated from the integrated peak areas divided by relative instrument sensitivity factors for each

element. Deconvolution of core level spectra was accomplished using MultiPAK (v.8.2.0). software with the instrument. The spectra were fit to a Gaussian-Lorentzian ($G/L = 0.8$) peak shape after Shirley background correction to calculate the atomic ratios of carbon and oxygen.

4.2.5 Scanning Electron Microscopy (SEM)

The morphology of the BDD films before and after the plasma treatments was studied by scanning electron microscopy (JEOL 7500F, JEOL Ltd., Center for Advanced Microscopy, MSU). The SEM micrographs were generally collected at 10,000x using a 5.0 kV accelerating voltage and a working distance of 4.5 mm.

4.2.6 Static Contact Angle Measurements

The wettability of the chemically-modified BDD electrodes was investigated by a photographic method using static contact angle measurements (KRÜSS GmbH DSA 100 Drop Shape Analyzer). The contact angles were recorded with ultrapure water and the two purified RTILs. A 0.1 μL droplet was placed on the BDD film using a 15 G Hamilton syringe that was positioned atop the glass pedestal. A photograph of the droplet interfacing with the electrode surface was then taken using a digital camera ~ 12 s after drop placement. The photographs were analyzed using the instrument software. The reported contact angle represents an average of five measurements across each BDD electrode at the center and the four corner regions. The reported angle is also an average of angles at the right- and left-hand side of the droplet, as measured in the photograph. All measurements were made with the instrument in a dry room at a relative humidity of $\leq 0.1\%$.

4.2.7 Electrochemical Measurements

The electrochemical measurements were made at room temperature in a standard three-electrode cell [39]. The BDD working electrode was clamped to the bottom of a three-neck, single compartment glass cell. A copper plate was used as the current collector. To produce good ohmic contact between the working electrode and the current collector, the backside of the p-Si substrate was scratched with SiC 800 grit paper, cleaned and coated with graphitic carbon using a standard pencil. A clean Viton™ O-ring between the bottom of the glass cell and the BDD film defined the geometric electrode area of 0.2 cm² exposed to the electrolyte. The reported current density represents the measured current normalized to the geometric area of the exposed BDD film. A Pt wire (0.5 mm diam.) served as the counter electrode. A large area spiral Ag wire was used as the quasi-reference electrode (Ag QRE). The potential of the Ag QRE in 0.5 mol L⁻¹ H₂SO₄ was 110 ± 6 mV vs. Ag/AgCl (3 mol L⁻¹ KCl). The reference and counter electrodes were positioned close to the working electrode. Approximately 500 µL of RTIL was used in each electrochemical measurement. All the experiments were performed in a dry N₂-purged glove box (Coy Laboratories) at room temperature with relative humidity below the detection limit (0.1% or 1000 ppm) of a digital hygrometer. All glassware was washed using Alconox/ultrapure water solution; rinsed sequentially with deionized water, isopropanol, acetone, and ultrapure water; and finally dried in an oven at 150 °C for at least 12 h before use.

Cyclic voltammetry (CV) and electrochemical impedance spectroscopy (EIS) were performed using a computer-controlled potentiostat (Model 660D, CH Instruments Inc., Austin, TX). CVs were recorded as a function of scan rate (0.01, 0.03, 0.05, 0.1, 0.2, 0.3, 0.4, 0.5 Vs⁻¹) and the capacitance was calculated from the slope of the background current at 0.0 V vs. scan rate plots using equation (1),

$$j_{average} = C_{dl}v \quad (1)$$

where $j_{average}$ ($A\ cm^{-2}$) is average background current density from the positive-going and negative-going sweeps at the specific potential, C_{dl} ($F\ cm^{-2}$) is the double-layer capacitance, and v ($V\ s^{-1}$) is the potential scan rate.

EIS was performed over a full frequency range from 0.1 to 10^5 Hz, with 20 data points collected per decade. A sinusoidal perturbation voltage of 10 mV (rms) was added to each negative-to-positive-going DC potential in 200 mV increments. An equilibration time of 5 min at each potential was allowed before the acquisition of the impedance data. The data were analyzed in the Nyquist plane using the CPE-based electrical equivalent circuit model shown in Figure 4.1 [40]. R_s represents the bulk electrolyte resistance and any electrode ohmic resistance in series with a parallel-connected constant phase element (CPE) and a high-frequency capacitor (C_{hf}). C_{hf} accounts for stray capacitance that arises from the instrumentation or connection cables [41–43]. It is usually in the range of nF and is potential-independent. It contributes to the impedance only at high frequencies > 20 kHz. Other studies using electrochemical methods, such as EIS [44] and single AC frequency measurements [45] [46] [47], have used this simple RC circuit. Small and Wheeler have emphasized the importance of fitting the impedance data using a simple RC circuit to avoid over-parameterization [48].

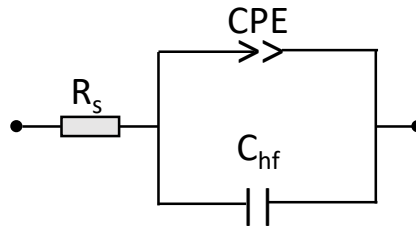


Figure 4.1. The representative electrical equivalent circuit that was used to fit the full-frequency impedance data.

In the Nyquist plane, a pure capacitor ideally exhibits frequency-independent capacitance and gives a straight vertical line along the $Z''-Z'$ plane. However, slightly tilted vertical lines with some curvature were observed for the BDD electrodes at certain potentials. This type of response is commonly modeled using a CPE element [43,49–51]. The cause for this response is the distribution of the activation energies across the electrode surface which is correlated to the existence of a wide variety of active sites differentially activated at a certain potential [52]. Polycrystalline electrodes are known to exhibit capacitance dispersion with frequency due to atomic-scale defects (kinks, steps, pits, and dislocations) and surface roughness at a microscopic level [39,42]. A simple way to account for this inhomogeneity is to use a CPE element:

$$Z_{CPE} = \frac{1}{Q(j.2\pi f)^\alpha} \quad (2)$$

where Z_{CPE} is the impedance for a CPE element in Ω , f is AC frequency in Hz, Q is the effective capacitance for a CPE element in $\Omega^{-1} s^\alpha$ and α is usually between 1 and 0.5 for real electrodes. Q is a pure capacitor when $\alpha = 1$.

4.2.8 Statistical Data Analysis

At least three sets of independent electrochemical measurements were performed in the two purified RTILs using at least three different BDD electrodes; all deposited using identical conditions. Such replicate measurements enabled assessment of the response variability and electrode-to-electrode statistical analysis. Data are presented as mean \pm standard deviation ($n \geq 3$). Statistically significant differences in mean values were determined using the unpaired Student's t -test ($p \leq 0.05$) with the control data being that for H-BDD.

4.3 Results

4.3.1 BDD Surface Termination

The near-surface elemental composition of the plasma-modified BDD films was determined using quantitative XPS. Figure 4.2 shows the elemental survey scans for H-, Ar- and O-BDD thin-film electrodes. The two main elements detected were C and O. The position of the C1s peak for graphite (C=C sp^2) is 284.5 eV, and for diamond (C-C sp^3) is 285.1 eV due to differences in the material work function [53,54]. In the present spectra, C1s and O1s peaks were observed at *ca.* 284.8 and 532.3 eV, respectively. The slight upshift in the C1s peak is due to the sp^3 bonding of carbon atoms in diamond. The peak at 970 eV is for the Auger transition for oxygen [54,55]. A weakly intense B 1s peak (0.23 at. %) was also observed at 188.5 eV, but only for the H-BDD electrode. The B 1s signal was not detected in the survey spectra from either the Ar- or O-BDD films. No other element was present at the detectable levels. The plasmon loss feature was observed at 318.5 eV. It arises from the energy losses of photoelectrons upon the excitation of the bulk and surface plasmons of diamond [56]. It is a characteristic feature of high purity (*i.e.*, low non-diamond carbon impurity) diamond.

As expected, the O1s peak intensity increased for the Ar- and O-BDD electrodes. The atomic O/C ratios were 0.01, 0.08, and 0.17, respectively, for H-, Ar- and O-BDD. An O/C atomic ratio of 0.18 is generally about the maximum oxygen coverage that has been reported for diamond films modified using methods like oxygen plasma and electrochemical oxidation [57–60]. The H₂ plasma produces a surface that is low in surface oxygen and primarily H-terminated. The Ar plasma introduces some surface oxygen since there is always some atmosphere leakage into the RF plasma chamber (mtorr vacuum only). As expected, the O₂ plasma produces the highest oxygen coverage.

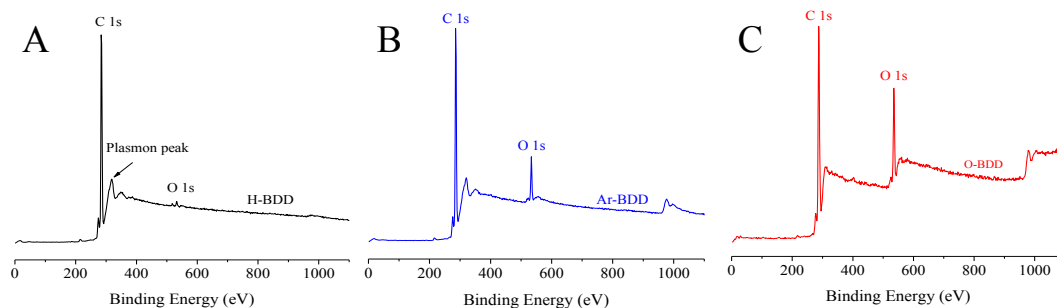


Figure 4.2. XPS survey scans for (A) H-BDD (black curve), (B) Ar-BDD (blue curve) and (C) O-BDD (red curve) thin-films after the different microwave or RF plasma treatments in H_2 , Ar and O_2 , respectively.

Deconvolution of the C1s peak was performed to determine the types of carbon-oxygen functional groups present on the surface (*i.e.*, the different chemical environments around the carbon atoms). Deconvoluted spectra are presented in Figure 4.3 and the results are summarized in Table 4.2. The largest peak area is attributed to the sp^3 carbon present in the films. The position of this peak shifts slightly towards higher binding energies with increasing surface oxygen from 284.5 eV for H-BDD to 284.8 eV for Ar-BDD and 284.9 eV for O-BDD. All other component peaks are reported as a shift relative to this base carbon peak. With increasing surface oxygen coverage, the C1s peak becomes more asymmetric with a tail toward higher binding energies [61] [62]. The higher binding energy components are associated with three different carbon-oxygen functional groups: hydroxyl or ether (C-OH, C-O-C) [+1.5 eV], carbonyl (C=O) [+3 eV], and carboxyl or ester (HO-C=O) [+4.5 eV] groups [62]. The H-BDD C1s spectrum shows the presence of one primary functional group with a shift of +1.8 eV. This is indicative of C-OH or C-O-C functional groups and accounts for 5.4% of the total area of the C1s peak. The C1s spectrum for Ar-BDD shows two functional group types at +1.5 and +3.0 eV consistent with C=O and HO-C=O groups, respectively. These account for 9.9% and 1.2%, respectively, of the total area of the C1s peak. The C1s spectrum for O-BDD reveals C-OH, C=O, and HO-C=O functional groups present

with shifts of +1.5, +3.0, and +3.9 eV. These functional groups account for 12.92%, 0.50%, and 6.91 %, respectively, of the total C1s peak area.

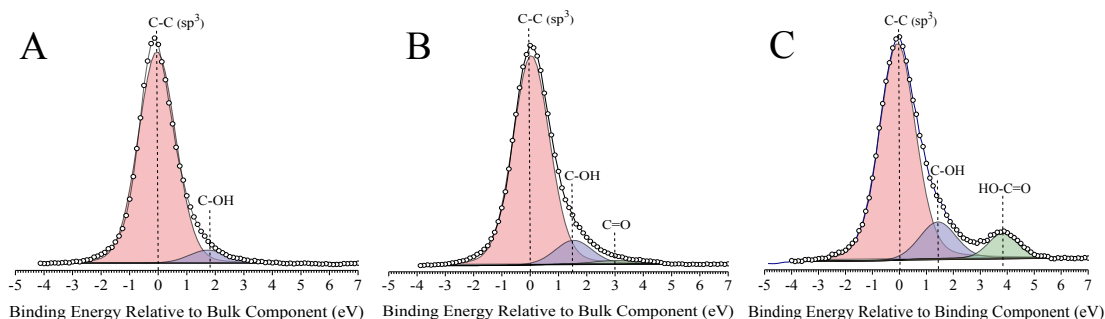


Figure 4.3. Deconvoluted C1s spectra revealing the carbon-oxygen functional group types, C-OH, C=O and HO-C=O, present on (A) H-BDD, (B) Ar-BDD and (C) O-BDD electrodes.

Table 4.2. Summary of the C1s Core Level XPS Data for H-BDD, Ar-BDD and O-BDD Electrodes.

| BDD Film | Binding Energy (eV) | Peak Shift from Base (eV) | Peak Area (%) | Chemical State |
|----------|---------------------|---------------------------|---------------|----------------|
| H-BDD | 284.5 | - | 94.6 | C-C |
| | 286.77 | 1.87 | 5.4 | C-O |
| Ar-BDD | 284.75 | - | 88.9 | C-C |
| | 286.29 | 1.5 | 9.9 | C-O |
| | 287.79 | 3.0 | 1.2 | C=O |
| O-BDD | 284.87 | - | 79.7 | C-C |
| | 286.28 | 1.5 | 12.9 | C-O |
| | 286.78 | 3.0 | 0.50 | C=O |
| | 288.68 | 3.9 | 6.9 | O-C=O |

4.3.2 Surface Film Morphology

SEM was used to evaluate the film morphology before and after the different plasma treatments to verify that no change was introduced. The O₂ plasma, in particular, can be very

damaging to carbon surfaces by roughening through carbon gasification [39,63]. Figure 4.4A and B presents electron micrographs of a BDD electrode before and after 12-min O₂ plasma treatment. Clearly, the exposure did not alter the film morphology. There is no evidence of pitting, etching, film delamination, or general surface roughening. The faceted and polycrystalline film, with some of the larger crystallites on the order of a several hundred nanometers in the lateral dimension, was unchanged after the plasma treatment. There were, however, some very minor morphological changes detected upon close inspection. These are indicated with arrows in Figure 4.4B. At these locations, some pitting and roughening occurred on a few of the crystallites and in the grain boundary between the crystallites. The pits develop because of carbon gasification as CO and CO₂ due to the reaction with atomic oxygen generated in the plasma. The damage though is very minor and highly localized. Etching effects by plasma species, specifically atomic hydrogen in an H₂ plasma, have been reported to be random, inhomogeneous, and dependent on the crystal facet or the orientation of diamond [64]. Although not presented, SEM revealed the H₂ and Ar plasma treatments produced no significant changes in the film morphology. No major or minor damage was detected.

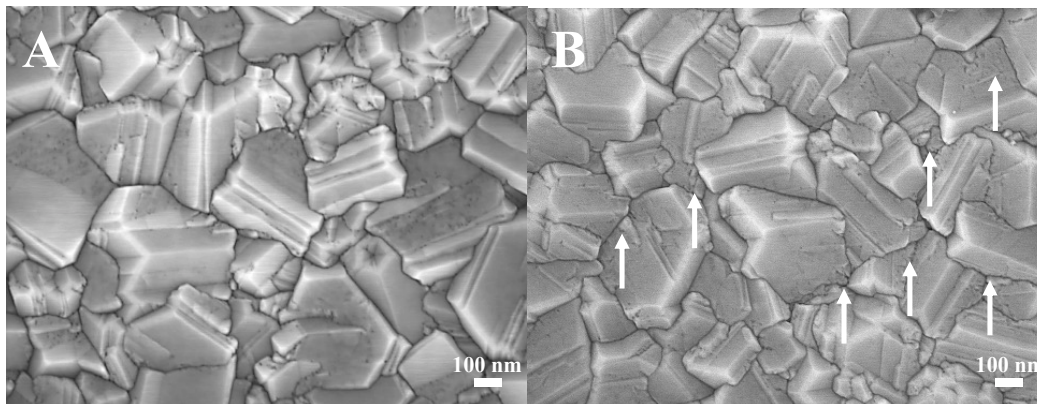


Figure 4.4. SEM micrographs of a nanocrystalline BDD thin-film (A) before and (B) after a 12-min O₂ RF plasma treatment.

4.3.3 Surface Wettability

Figure 4.5 shows photographs of ultrapure water and purified [BMIM][PF₆] droplets on H-BDD, Ar-BDD and O-BDD surfaces. The nominal contact angles for water on H-, Ar-, and O-BDD were 110 ± 1 , 52 ± 6 , and 41 ± 6 degrees, respectively. As expected, the highest contact angle is seen for the H-BDD surface with the lowest XPS O/C atomic ratio. The contact angles decrease for Ar- and O-BDD. On the other hand, the nominal contact angles for [BMIM][PF₆] on H-, Ar- and O-BDD followed the opposite trend: 20 ± 2 , 22 ± 1 , and 49 ± 7 degrees, respectively. The nominal contact angles for [HMIM][PF₆] followed the same trend: 11 ± 2 , 47 ± 2 , and 41 ± 5 degrees for H-, Ar- and O-BDD, respectively. For the RTILs, the greatest wettability is seen on H-BDD; the surface with the lowest surface oxygen coverage. In summary, the wettability of the BDD surface for water increases with increasing polar carbon-oxygen functional group coverage. In contrast, the wettability by [BMIM][PF₆] and [HMIM][BF₆] decrease with increasing polar carbon-oxygen functional group coverage.

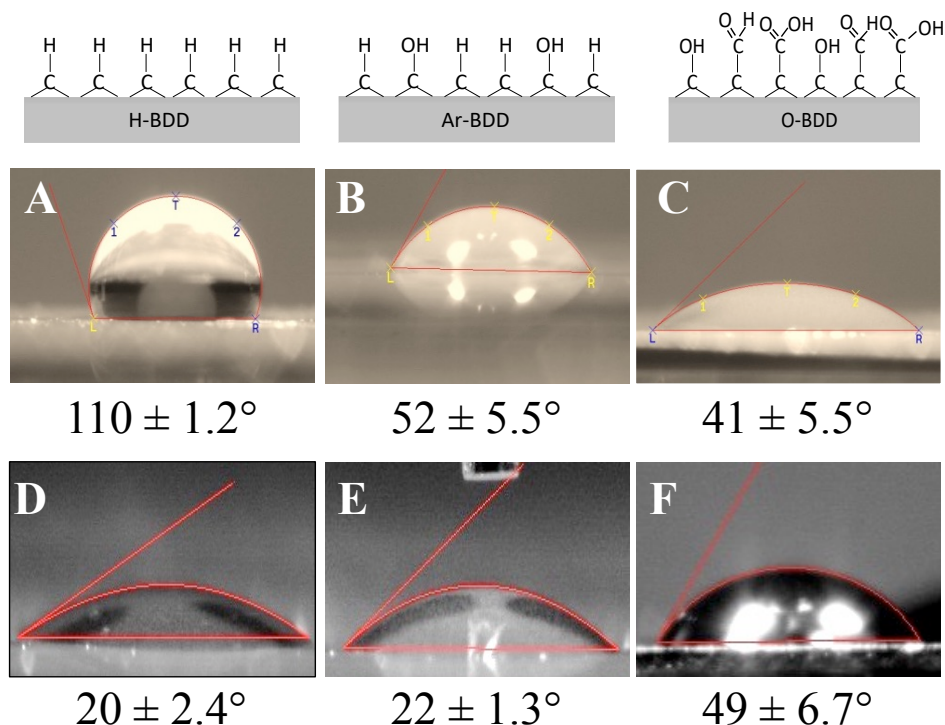


Figure 4.5. The upper panels illustrate the surface terminating oxygen functional groups on the H-, Ar- and O-BDD surfaces. Photographs of droplets and static contact angle data for water (A-C) and for [BMIM][PF₆] (D-F) on the three surfaces. Values are reported as mean ± standard deviation (n = 5 measurements on different areas of each BDD electrode).

4.3.4 Electrochemical Potential Windows

Figure 4.6 shows background cyclic voltammetric curves for H-BDD in both [HMIM][PF₆] and [BMIM][PF₆] over a wide potential range. The working potential window in both RTILs is 6 V. The potentials for the positive and negative-going currents at ± 50 μAcm⁻² were chosen to define the window. The voltammetric current magnitude is higher for [BMIM][PF₆] than for [HMIM][PF₆]. There is an anodic peak around 1.8 V observed on the positive-going sweep and a small cathodic current starting about -1 V in both RTILs. The peak near 1.8 V is presumed due to the oxidation of trace water impurity [65]. The origin of the peak at -1 V is unclear but may be related to the reduction of some residual dissolved oxygen. It should be noted that the 6 V potential

window for BDD in the RTILs is 2x larger than the typical 3 V window observed for BDD in aqueous electrolytes, such as 0.5 mol L⁻¹ H₂SO₄. Similar wide working potential windows in these and other RTILs have been reported previously for BDD electrodes [25,28,29]. The insets overlay the background voltammetric current in both RTILs over a narrower potential range from -0.5 to 1.0 V vs. Ag QRE. The current density at 0 V when scanning over the narrower range is below 1 μAcm^{-2} for both RTILs. However, the current density increased by a factor of 3 to 8 when the potential range was scanned over the full 6 V window. There must be some redox processes that add to the total background current when scanning over the full potential window. For example, the capacitance at 0 V, calculated using equation (i), is 7 μFcm^{-2} when scanning over the narrow potential range. However, it increases by 3.5x to 25 μFcm^{-2} when the potential range was scanned over the full 6 V range.

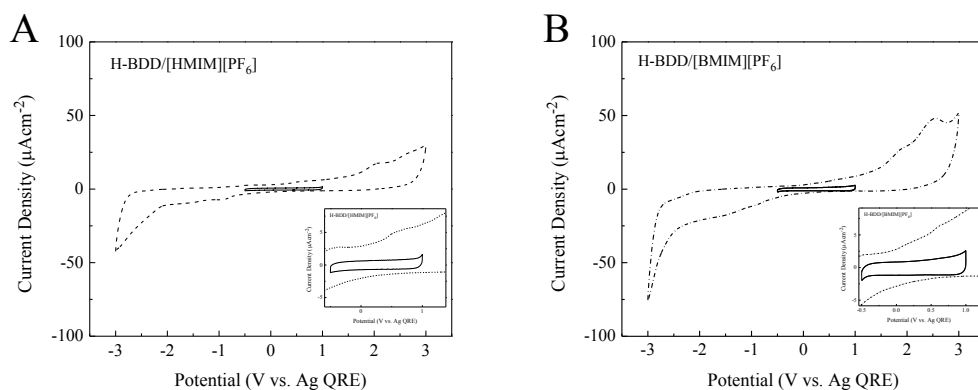


Figure 4.6. Cyclic voltammetric j - E curves for a H-BDD thin-film electrode in (A) [HMIM][PF₆] and (B) [BMIM][PF₆] over a wide potential window of 6 V (dash curves). The narrower potential region of ~2 V (solid curves) used for the capacitance measurements is also shown (solid curve). The insets show j - E curves for H-BDD over a more narrow 1.5 V potential range in (A) [HMIM][PF₆] and (B) [BMIM][PF₆]. Scan rate = 0.1 Vs⁻¹.

4.3.5 Capacitance-Potential (C-E) Trends in RTILs

Figure 4.7A shows j - E curves for H-BDD in [BMIM][PF₆] recorded over a 1.5 V potential window as a function of scan rate from 0.01 to 0.5 Vs⁻¹. The voltammetric curves are symmetrical

about the zero-current line and exhibit a rectangular shape, consistent with a capacitive process. The currents are low (0.1 to $5 \mu\text{A cm}^{-2}$) and increase with the scan rate. Current density vs. scan rate plots at different potentials were generated for the H-, Ar- and O-BDD films in $[\text{BMIM}][\text{PF}_6]$. Figure 4.7B shows plots for the current measured at 0 V . The background current density for all three electrodes increases proportionally with the scan rate ($R^2 \geq 0.999$). This indicates that the background current at this potential, and in fact at other potentials in the -0.5 to 1 V range, is capacitive arising solely from double-layer charging. Capacitance values were calculated from the plot slopes with the following trend in nominal values: H-BDD ($9.1 \mu\text{Acm}^{-2}$) > Ar-BDD ($5.0 \mu\text{Acm}^{-2}$) and O-BDD ($4.1 \mu\text{Acm}^{-2}$) (Table 4.3). The capacitance values for Ar-BDD and O-BDD are half the value for H-BDD. The capacitance values track the wettability trends in the RTILs (*i.e.*, highest capacitance is seen for the electrode with the lowest contact angle). Even in the viscous RTILs, the ion excesses in the interfacial region are established as fast as the potential (*i.e.*, excess surface charge) is changed at these scan rates.

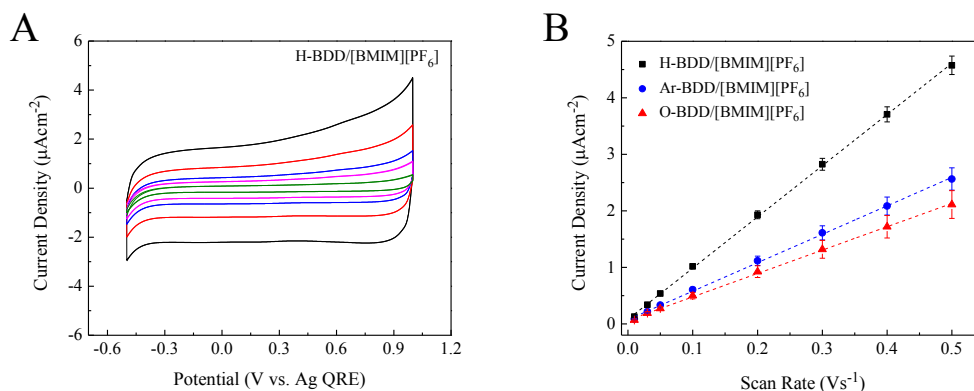


Figure 4.7. (A) Cyclic voltammetric (j -E) curves recorded as a function of scan rate (0.01 to 0.5 Vs^{-1}) for H-BDD thin-film electrode in $[\text{BMIM}][\text{PF}_6]$. (B) A plot of background current density, j , at 0.0 V vs. Ag QRE against scan rate for H-BDD (■), Ar-BDD (●) and O-BDD (▲). Current density values are the average of the positive and negative sweeps in the cyclic voltammogram. Values are plotted as mean \pm std. dev. ($n=3$ electrodes).

Table 4.3. Capacitance values calculated from the linear regression analysis of plots of the current density (μAcm^{-2}) vs. scan rate (Vs^{-1}) for H-, Ar- and O-BDD electrodes in $[\text{BMIM}][\text{PF}_6]$ shown in Fig. 4.7B. Values are reported as mean \pm std. dev. for $n=3$ electrodes.

| BDD Film | C_{dl} (μFcm^{-2}) | R^2 |
|----------|-----------------------------------|--------|
| H-BDD | 9.1 ± 0.3 | 0.9997 |
| Ar-BDD | 5.0 ± 0.6 | 0.9992 |
| O-BDD | 4.1 ± 0.6 | 0.9991 |

The background cyclic voltammetric curves are compared in Figure 4.8A for H-, Ar- and O-BDD in $[\text{BMIM}][\text{PF}_6]$ at a 0.1 Vs^{-1} . The current densities for Ar- and O-BDD at all potentials are lower than for H-BDD, consistent with decreased surface wetting by the RTIL. Plots of the capacitance, determined from the voltammetric data, versus potential are presented in Figure 4.8B. The capacitance for H-BDD increases with increasing positive potential from $8.8 \mu\text{Fcm}^{-2}$ at -0.4 V to $15.1 \mu\text{Fcm}^{-2}$ at 0.9 V . The capacitance for Ar-BDD is relatively independent of applied potential varying from $5.5 \mu\text{Fcm}^{-2}$ at -0.4 V to $6.9 \mu\text{Fcm}^{-2}$ at 0.8 V . The capacitance of O-BDD is also relatively independent of potential but slightly lower than values for the other two electrodes. The capacitance varies from 4.7 at -0.4 V to $6.1 \mu\text{F cm}^{-2}$ at 0.8 V . In summary, the voltammetric current and the potential dependent capacitance follow the trend $\text{H-BDD} > \text{Ar-BDD} > \text{O-BDD}$ in $[\text{BMIM}][\text{PF}_6]$.

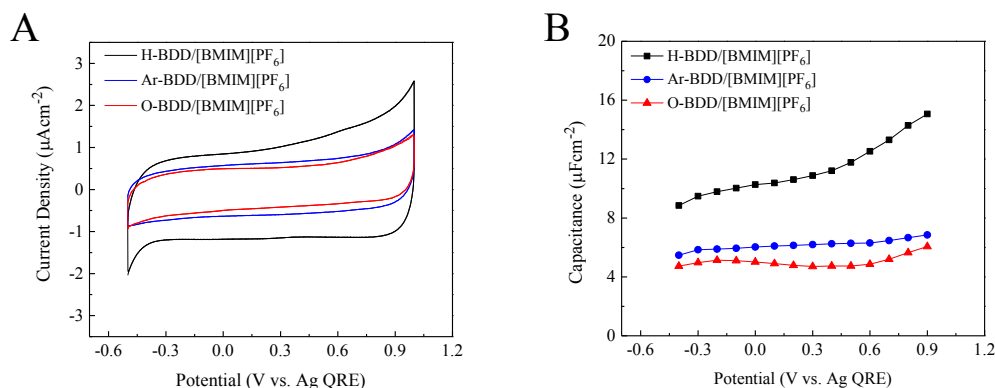


Figure 4.8. (A) Overlay of cyclic voltammetric j - E curves recorded at 0.1 Vs^{-1} for H-BDD (black curve), Ar-BDD (blue curve) and O-BDD (red curve) in [BMIM][PF₆]. (B) Corresponding capacitance-potential (C - E) curves for H-BDD (●), Ar-BDD (●), and O-BDD (▲) in [BMIM][PF₆]. The capacitance values were calculated from the $j_{\text{average}} (\mu\text{Acm}^{-2})/v (\text{Vs}^{-1})$ values according to equation 1. Capacitance values are presented for just one of each modified electrode.

Figure 4.9A shows j - E curves at 0.1 Vs^{-1} for the H-, Ar- and O-BDD thin-film electrodes in [HMIM][PF₆]. H-BDD exhibits the largest current density over the entire potential range. The background current at most of the potentials follows the same trend as seen for the less viscous [BMIM][PF₆]: H-BDD > Ar-BDD > O-BDD. Overall, the currents were lower for all the electrodes in [HMIM][PF₆], as compared to [BMIM][PF₆]. The current density for H-BDD increases in [HMIM][PF₆] from 0.3 to $2.4 \mu\text{Acm}^{-2}$ on the positive-going and from -0.1 to $-1.5 \mu\text{Acm}^{-2}$ on the negative-going potential sweep. The Ar- and O-BDD films exhibit lower but similar current densities over the potential range. The corresponding C - E curves reveal the largest capacitance for H-BDD, increasing from 11 to $15 \mu\text{Fcm}^{-2}$ with increasing positive potential. The

capacitance of both Ar-BDD and O-BDD electrodes exhibits little potential dependence ranging from 8 to 10 μFcm^{-2} .

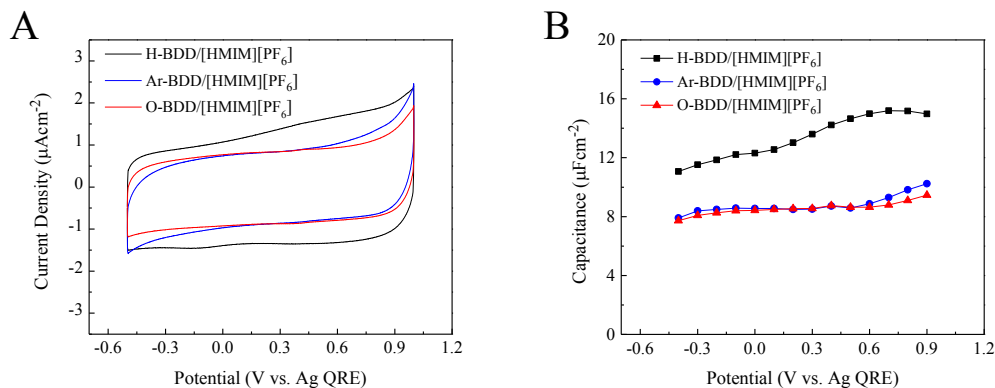


Figure 4.9. (A) Overlay of cyclic voltammetric j - E curves recorded at 0.1 Vs^{-1} for H-BDD (black curve), Ar-BDD (blue curve), and O-BDD (red curve) in $[\text{HMIM}][\text{PF}_6]$. (B) Corresponding capacitance-potential (C-E) curves for H-BDD (■), Ar-BDD (●), and O-BDD (▲) in $[\text{HMIM}][\text{PF}_6]$. The capacitance values were calculated from the $j_{\text{average}} (\mu\text{Acm}^{-2})/\nu (\text{Vs}^{-1})$ values according to equation 1. Capacitance values are presented for just one of each modified electrode.

The C - E data were also obtained using full frequency electrochemical impedance spectroscopy. C - E profiles were constructed from the impedance data as a function of potential. Figure 4.10 shows the real (Z') vs. imaginary (Z'') components of the total impedance in the Nyquist plane for H-BDD in $[\text{HMIM}][\text{PF}_6]$ (Fig. 4.10A) and $[\text{BMIM}][\text{PF}_6]$ (Fig. 4.10B). Data recorded over a broad frequency range from 0.1 to 10^5 Hz as a function of applied potential are presented. Vertical lines are seen of the essentially same magnitude for several of the potentials, consistent with a dominant capacitive process controlling the flow of current through the electrochemical system. The overlap of the curves indicates similar capacitance at these potentials. The steeper and closer to the imaginary axis the plot is, the purer and larger the capacitance is [64]. At negative potentials (-0.7 and -0.9 V), the curves become non-linear at higher frequencies, and the magnitude of Z'' decreases. These curves suggest that there is some non-capacitive current

flowing at these potentials. Similar behavior is seen for [BMIM][PF₆]. The difference in data for the two RTILs is that the deviation from linearity (*i.e.*, pure capacitive process) starts at less negative potentials in [HMIM][PF₆].

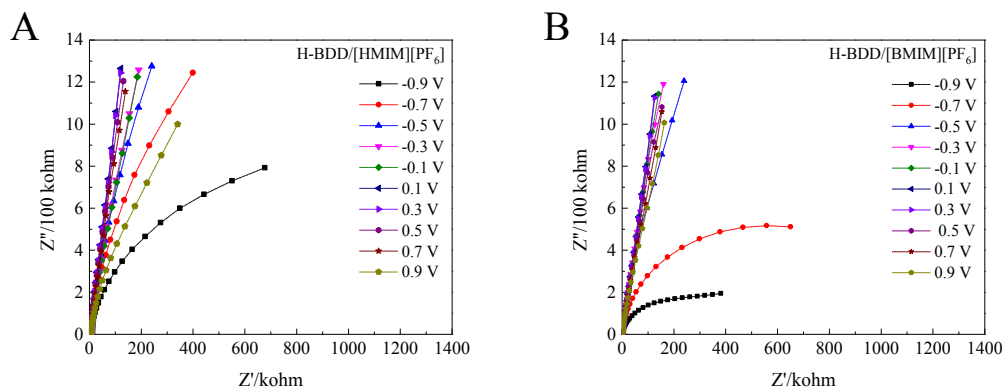


Figure 4.10. Stacked Nyquist plots of the real (Z') vs. imaginary (Z'') components of the total impedance for an H-BDD thin-film electrode in (A) [HMIM][PF₆] and (B) [BMIM][PF₆] as a function of applied potential.

Figure 4.11 compares C - E plots obtained from the EIS data for H-BDD, Ar-BDD, and O-BDD in [HMIM][PF₆] (Fig. 4.11A) and [BMIM][PF₆] (Fig. 4.11B). The capacitance magnitude for H-BDD ranges from 6.2 to 11.7 μFcm^{-2} in [HMIM][PF₆] and from 2.5-12.0 μFcm^{-2} in [BMIM][PF₆]. The capacitance values are in reasonable agreement with the values determined by cyclic voltammetry. This is often the case with BDD electrodes because the surface is largely unreactive such that little current flows at mid-range potentials than is not capacitive in origin. The capacitance values overall are higher in [HMIM][PF₆] than in [BMIM][PF₆]. There is a general trend of increasing capacitance with increasing positive potential for most of the modified electrodes in both RTILs. The exception to this is the capacitance of Ar-BDD and O-BDD in both

the RTILs, which is relatively independent of potential over the range. There is an increase in capacitance seen at potentials positive of 0.8 V.

The shape of the C - E curves for the different modified BDD electrodes is more or less flat. There is no U-shape curvature or inverted parabolic shape as is often reported for metal electrodes in contact with RTILs [66–68]. The exception is the U-shape is seen for H-BDD in [BMIM][PF₆] with a capacitance minimum at -0.4 V vs. Ag QRE. Such a U-shape was not observed for any of the Ar- and O-BDD electrodes tested. The measured capacitance followed the same trend in both RTILs: H-BDD > Ar-BDD and O-BDD. This is similar to the trend seen from the cyclic voltammetric data. Recall that in [BMIM][PF₆], the static contact angles were: $20 \pm 2^\circ$ for H-BDD, $22 \pm 1^\circ$ for Ar-BDD and $49 \pm 7^\circ$ for O-BDD. The largest capacitance is observed for the electrode with the lowest contact angle. Similarly, in [HMIM][PF₆], H-BDD, which has a contact angle of 11 ± 2 , exhibits a higher capacitance than Ar- and O-BDD, which have higher contact angles of 47 ± 2 and 41 ± 5 , respectively. In summary, the BDD electrode capacitance in the RTILs decreases with increasing contact angle (*i.e.*, decreased surface wettability) and increasing surface oxygen coverage.

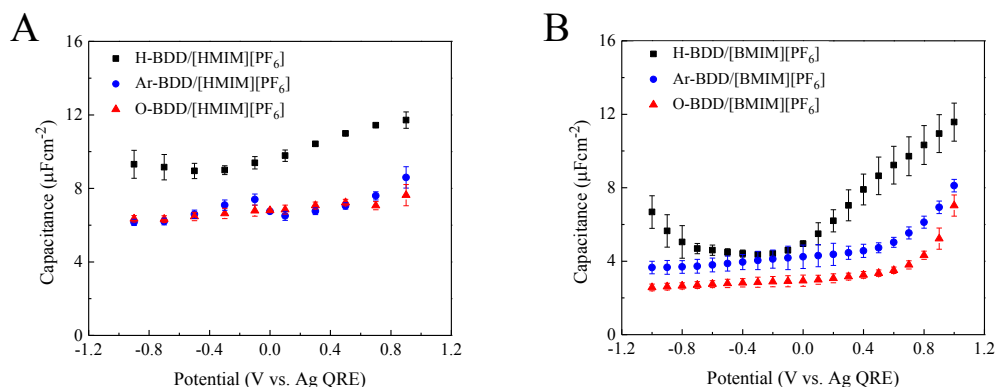


Figure 4.11. Comparison of capacitance-potential (C - E) trends recorded for H-BDD (■), Ar-BDD (●) and O-BDD (▲) in (A) [HMIM][PF₆] and (B) [BMIM][PF₆]. The capacitance values were calculated from EIS data. The data are plotted as mean \pm standard deviation for $n=3$ electrodes.

4.3.6 Capacitance-Potential (*C-E*) Trends in an Aqueous Electrolyte

Comparison measurements were performed with these same modified BDD electrodes in 0.5 mol L⁻¹ H₂SO₄. Figure 4.12A shows background cyclic voltammetric curves recorded at 0.1 Vs⁻¹ using H-BDD and O-BDD thin-film electrodes. It is worth noting that the values for the current densities are 2-10x higher, depending on the potential, than those recorded in [BMIM][PF₆] or [HMIM][PF₆]. The background voltammetric current in 0.5 mol L⁻¹ H₂SO₄ was larger for O-BDD than for H-BDD, consistent with the lower water contact angle on the former. The voltammetric curve for H-BDD is flat and symmetric about the zero-current line over the potential range. In contrast, the curve for O-BDD is also flat and symmetric about the zero current line except at potentials positive of 0.6 V on the positive-going sweep. On the negative-going sweep, there is a small peak current at 0.9 V. The origin of these currents is unclear. Figure 4.12B shows the corresponding current density vs. scan rate plots for O-BDD and H-BDD. Both plots are linear ($R^2 = 0.999$) indicating the current at this potential (0 V) is capacitive. The capacitance for H-BDD and O-BDD, calculated from the slopes of these curves, is 15.9 ± 2.2 and 21.9 ± 1.3 μFcm^{-2} , respectively (Table 4.4). The larger capacitance in aqueous electrolyte explains the larger voltammetric current, as compared to the RTILs. The reasons for the lower capacitance in the RTILs are (i) the dielectric constant of the RTILs is 8-9x lower than the dielectric constant for water and (ii) the true ionic concentration is likely significantly less than the total ionic concentration (4-6 M) of the two RTILs due to ion pairing, with both being less than the ionic concentration in H₂SO₄.

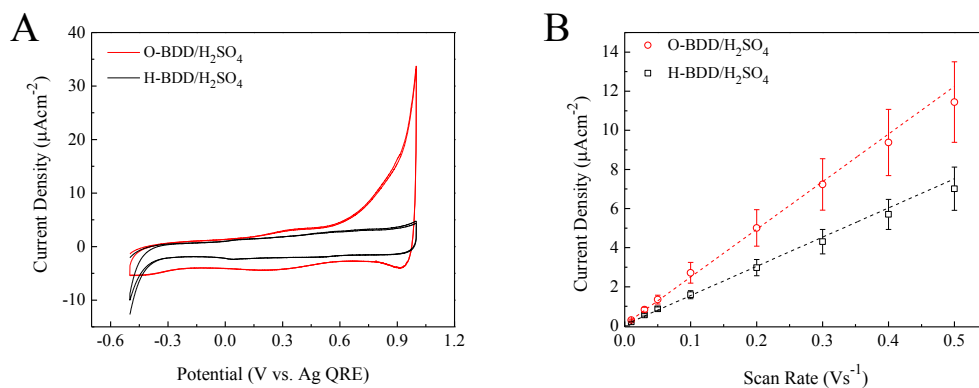


Figure 4.12. (A) Cyclic voltammetric (j - E) curves for O-BDD (outer red curve) and H-BDD (inner black curve) in 0.5 M H₂SO₄. Scan rate = 0.1 Vs⁻¹. (B) A plot of corresponding current density at 0.0 V vs. Ag QRE against scan rate for O-BDD (○) and H-BDD (□) in 0.5 mol L⁻¹ H₂SO₄. Current density values are presented as mean ± std. dev. for n=3 electrodes of each type.

Table 4.4. Capacitance values calculated from current density vs. scan rate plots and linear regression analysis for O-BDD and H-BDD in 0.5 mol L⁻¹ H₂SO₄. Data are presented as mean ± std. dev. for n = 3 electrodes of each type.

| BDD Film | C_{dl} (μFcm ⁻²) | R ² |
|----------|--------------------------------|----------------|
| H-BDD | 15.9 ± 2.2 | 0.9996 |
| O-BDD | 21.9 ± 1.3 | 0.9982 |

The C - E profiles for H-BDD and O-BDD in 0.5 mol L⁻¹ H₂SO₄ constructed from EIS data indicate slightly larger values at all potentials for O-BDD than for H-BDD (Figure 4.13). The capacitance for both the electrodes increases with increasing positive potential. The capacitance for O-BDD increased from 7.4 at -0.9 V to 28.7 at 0.9 V μFcm⁻². For H-BDD, the capacitance increased from 4.0 μFcm⁻² at -0.9 V vs. to 16.7 μFcm⁻² at 0.9 V. In summary, the capacitance is

greater for the BDD electrodes exhibiting the lowest water contact angle and the highest surface oxygen coverage.

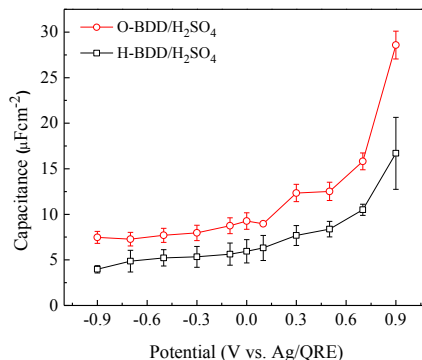


Figure 4.13. Comparison of capacitance-potential (C - E) profiles for O-BDD (\circ) and H-BDD (\square) in $0.5 \text{ mol L}^{-1} \text{ H}_2\text{SO}_4$. The capacitance values were calculated from EIS data. Capacitance values are presented as mean \pm std. dev. for $n=3$ electrodes of each type.

4.4 Discussion

The primary goal of this study was to understand how the surface chemistry (H vs. O) affects the wettability and electrochemical properties of BDD electrodes in two different RTILs, as compared with an aqueous electrolyte solution. The electrochemical properties were evaluated by background cyclic voltammetric j - E curves as a function of scan rate and full-frequency electrochemical impedance spectroscopy as a function of the applied potential. BDD thin-film electrodes were prepared by microwave-assisted CVD method using a 1% methane/hydrogen source gas mixed with diborane at a gas-phase boron concentration of 10 ppm. Extensive care was taken to minimize the formation of sp^2 -bonded carbon impurity at the surface by keeping the methane/hydrogen ratio low at 1% (v/v) and the post-growth cooling procedure. sp^2 -bonded carbon would form at the surface with a hard shut down due to desorption of surface hydrogen at the deposition temperature and reconstruction of the surface carbon atoms to form pi-bonded dimers.

The doping level was estimated to be in the low 10^{21} cm^{-3} range based on Raman spectroscopy and Hall effect measurement data of other films deposited under similar conditions [34]. To generate BDD films with different surface terminations, the films were plasma-treated using appropriate gas. The H_2 plasma cool down produces a surface that is low in oxygen coverage that is primarily H-terminated. The Ar plasma introduced some surface oxygen since there is always some atmosphere leakage into the plasma chamber (mtorr vacuum). The Ar gas in the chamber ionizes and creates a glow discharge around the electrode bombarding the surface with Ar^+ . The ion bombardment also acts to clean the surface.

As expected, the O_2 plasma produced the highest surface oxygen coverage. The XPS atomic O/C ratios were 0.01, 0.08, and 0.17 for H-BDD, Ar-BDD, and O-BDD, respectively. The O/C ratio of 0.18 is about the maximum oxygen coverage that has been reported for BDD films modified using techniques such as oxygen plasma and electrochemical oxidation [69]. XPS measurements further revealed the nature of oxygen-containing groups present on the surface of plasma-treated BDD films. While H-BDD was found to have only C-OH and C-O-C functional groups, Ar-BDD surface was populated with C-OH and C=O groups. In comparison, O-BDD surface presented a more diverse mix of functional groups with XPS revealing the presence of C-OH, C=O, and HO-C=O groups.

One of the critical factors with plasma-treated BDD films is the surface roughening and damage, such as pitting, etching and film delamination that can result particularly in H_2 (atomic H) O_2 (atomic O) plasmas. Pitting occurs due to the gasification of carbon in atomic O to form CO and CO_2 . Pitting can also occur in atomic H due to the formation of CH_4 and C_2H_2 . Pitting and etching in atomic H are localized and dependent on the diamond crystal facet [35]. Such surface roughening would cause increases in the background voltammetric current and capacitance. SEM

micrographs revealed no significant change in the BDD film surface topography after either the H₂ or O₂ plasma treatments. Some very minor and localized pitting was observed in a few select grain boundaries of the film after the O₂ plasma treatment. The surface wettability of the plasma-treated films was investigated by static contact angle measurements using water and RTILs as the contacting liquids. The static contact angle for water on H-BDD, Ar-BDD, and O-BDD were measured to be 110 ± 1.2 , 52 ± 5.5 , and 41 ± 5.5 degrees, respectively. For the RTILs, the corresponding contact angle for H-BDD, Ar-BDD, and O-BDD were 20 ± 2.4 , 22 ± 1.3 , 49 ± 6.7 degrees and 11 ± 2.0 , 47 ± 2.1 and 41 ± 5.4 degrees for [BMIM][PF₆] and [HMIM][PF₆], respectively. The wettability of the BDD surface for water increases with increasing polar carbon-oxygen functional group coverage. In contrast, the wettability by [BMIM][PF₆] and [HMIM][PF₆] decreases with increasing polar carbon-oxygen functional groups coverage.

The background voltammetric current and capacitance for all three modified electrodes are larger in [HMIM][PF₆] due to higher surface wettability. With higher wettability, RTIL ions can approach the BDD surface more closely resulting in greater excess charge density closer to the electrode, hence greater capacitance. Comparing H-BDD, Ar-BDD, and O-BDD, the capacitance is highest for H-BDD electrodes followed by Ar- and O-BDD in both the RTILs. The wettability and capacitance both decrease in the RTILs with increasing surface oxygen coverage. The exact opposite trend was observed in 0.5 M H₂SO₄. The wettability, background current and capacitance all increase with increasing surface oxygen coverage. In aqueous electrolyte, increased capacitance of carbon nanosheets was observed with increased wettability and surface carbon-oxygen functional group coverage [69].

4.5 Conclusions

Boron-doped nanocrystalline diamond thin-film electrodes were chemically modified using microwave or RF plasma treatment to produce low, medium and high surface oxygen coverages. The plasma treatments were performed in H₂, Ar or O₂. The surface oxygen coverage (atomic O/C ratio), as determined from XPS data, was 0.01 for H-BDD, to 0.08 for Ar-BDD and 0.17 for O-BDD. The effect of surface oxygen coverage on the wettability, background voltammetric current, and capacitance in two different RTILs ([BMIM][PF₆] and [HMIM][PF₆]) was investigated. Comparison studies were performed in 0.5 M H₂SO₄. The following are the key findings from the work:

1. The static contact angle of water on the modified electrodes decreased from 110 (H-BDD) to 41 (O-BDD) degrees with increasing surface oxygen coverage, as expected as the surface becomes more hydrophilic.
2. The opposite trend was seen for both RTILs as the contact angle increased from 20 (H-BDD) to 50 (O-BDD) degrees with increasing surface oxygen coverage.
3. The cyclic voltammetric background current and potential-dependent capacitance in both RTILs were largest for BDD electrodes with the lowest surface oxygen coverage ratio (H-BDD) and lowest contact angle.
4. Slightly larger voltammetric background currents and capacitance were observed in [HMIM][PF₆] than in [BMIM][PF₆]. Capacitance values ranged from 8 – 16 $\mu\text{F cm}^{-2}$ over the potential range for H-BDD and from 4 – 6 $\mu\text{F cm}^{-2}$ for O-BDD. The opposite trend was observed in H₂SO₄.
5. Capacitance values were lower in the RTILs on a particular electrode than in the aqueous electrolyte.

6. The working potential window for the BDD electrodes was the same, *ca.* 6V, in both RTILs.

4.6 Acknowledgements

The research was carried out under the framework of project #W911-NF-14-10063 funded by the Army Research Office (GMS).

REFERENCES

REFERENCES

- [1] M. Armand, F. Endres, D.R. MacFarlane, H. Ohno, B. Scrosati, Ionic-liquid materials for the electrochemical challenges of the future, *Nat. Mater.* 8 (2009) 621–629. doi:10.1038/nmat2448.
- [2] M. Galiński, A. Lewandowski, I. Stepniak, Ionic liquids as electrolytes, *Electrochim. Acta.* 51 (2006) 5567–5580. doi:10.1016/j.electacta.2006.03.016.
- [3] H.C.L. Tsuda Tetsuya, W. Tian, Y.X. Jia, H.Y. Yue, Electrochemical Applications of Room-Temperature Ionic Liquids, *Interface (The Electrochem. Soc.* 16 (2007) 42–49. doi:10.1002/elps.200800561.
- [4] S. Passerini, G.B. Appetecchi, Toward more environmentally friendly routes to high purity ionic liquids, *MRS Bull.* 38 (2013) 540–547. doi:10.1557/mrs.2013.155.
- [5] P. Hapiot, C. Lagrost, Electrochemical reactivity in room-temperature ionic liquids, *Chem. Rev.* 108 (2008) 2238–2264. doi:10.1021/cr0680686.
- [6] I. Borukhov, D. Andelman, H. Orland, Steric Effects in Electrolytes: A Modified Poisson-Boltzmann Equation, *Phys. Rev. Lett.* 79 (1997) 435–438. doi:10.1103/PhysRevLett.79.435.
- [7] G.M. Hupert, Matt, Muck, Alexander, Wang, Jian, Stotter Jason, Cvackova, Zuzana, Haymond, Shannon, Show, Yoshiyuki, Swain, Conductive diamond thin-films in electrochemistry, *Diam. Relat. Mater.* 12 (2003) 1940–1949. doi:10.1016/S0925-9635.
- [8] G.M. Swain, Electroanalytical applications of diamond electrodes, *Semicond. Semimetals.* 77 (2004) 121–148. doi:10.1016/S0080-8784(04)80016-4.
- [9] J. V Macpherson, A practical guide to using boron doped diamond in electrochemical research., *Phys. Chem. Chem. Phys.* 17 (2015) 2935–49. doi:10.1039/c4cp04022h.
- [10] N. Yang, G.M. Swain, X. Jiang, Nanocarbon Electrochemistry and Electroanalysis: Current Status and Future Perspectives, *Electroanalysis.* 28 (2016) 27–34. doi:10.1002/elan.201500577.
- [11] J. Wang, G.M. Swain, Dimensionally Stable Pt/Diamond Composite Electrodes in Concentrated H₃PO₄ at High Temperature, *Electrochem. Solid-State Lett.* 5 (2002) E4–E7. doi:10.1149/1.1435563.
- [12] P.E. Pehrsson, T.W. Mercer, J.A. Chaney, Thermal oxidation of the hydrogenated diamond (100) surface, *Surf. Sci.* 497 (2002) 13–28. doi:10.1016/S0039-6028(01)01677-6.

- [13] K. Hayashi, S. Yamanaka, H. Watanabe, T. Sekiguchi, H. Okushi, K. Kajimura, Investigation of the effect of hydrogen on electrical and optical properties in chemical vapor deposited on homoepitaxial diamond films, *J. Appl. Phys.* 81 (1997) 744–753. doi:10.1063/1.364299.
- [14] F.B. Liu, X.M. Li, J.D. Wang, B. Liu, D.R. Chen, Effects of the surface-adsorption of boron-doped diamond electrode on its electrochemical behavior, *Chinese Sci. Bull.* 51 (2006) 1903–1908. doi:DOI 10.1007/s11434-006-2024-1.
- [15] L. a Hutton, J.G. Iacobini, E. Bitziou, R.B. Channon, M.E. Newton, J. V Macpherson, Examination of the Factors Affecting the Electrochemical Performance of Oxygen-Terminated Polycrystalline Boron-Doped Diamond Electrodes BT - Analytical Chemistry, *Anal. Chem.* 85 (2013) 7230–7240. doi:10.1021/ac401042t.
- [16] F. Maier, M. Riedel, B. Mantel, J. Ristein, L. Ley, Origin of surface conductivity in diamond, *Phys. Rev. Lett.* 85 (2000) 3472–5. <http://www.ncbi.nlm.nih.gov/pubmed/11690524>.
- [17] K. Kimura, K. Nakajima, S. Yamanaka, M. Hasegawa, H. Okushi, Hydrogen depth-profiling in chemical-vapor-deposited diamond films by high-resolution elastic recoil detection, *Appl. Phys. Lett.* 78 (2001) 1679–1681. doi:10.1063/1.1356452.
- [18] S. Garcia-Segura, E. Vieira Dos Santos, C.A. Martínez-Huitle, Role of sp³/sp² ratio on the electrocatalytic properties of boron-doped diamond electrodes: A mini review, *Electrochem. Commun.* 59 (2015) 52–55. doi:10.1016/j.elecom.2015.07.002.
- [19] J. Li, C.L. Bentley, S.Y. Tan, V.S.S. Mosali, M.A. Rahman, S.J. Cobb, S.X. Guo, J. V. Macpherson, P.R. Unwin, A.M. Bond, J. Zhang, Impact of sp² Carbon Edge Effects on the Electron-Transfer Kinetics of the Ferrocene/Ferricenium Process at a Boron-Doped Diamond Electrode in an Ionic Liquid, *J. Phys. Chem. C.* 123 (2019) 17397–17406. doi:10.1021/acs.jpcc.9b04519.
- [20] T. Liu, K. Wang, Y. Chen, S. Zhao, Y. Han, Dominant role of wettability in improving the specific capacitance, *Green Energy Environ.* 4 (2019) 171–179. doi:10.1016/j.gee.2019.01.010.
- [21] J.F. Evans, T. Kuwana, Radiofrequency Oxygen Plasma Treatment of Pyrolytic Graphite Electrode Surfaces, *Anal. Chem.* 49 (1977) 1632–1635. doi:10.1021/ac50019a042.
- [22] J.F. Evans, T. Kuwana, Introduction of Functional Groups onto Carbon Electrodes via Treatment with Radio-Frequency Plasmas, *Anal. Chem.* 51 (1979) 358–365. doi:10.1021/ac50039a010.
- [23] S. Bachmann, M. Schulze, J. Morasch, S. Hesse, L. Hussein, L. Krell, J. Schnagl, R.W. Stark, S. Narayan, Aging of oxygen and hydrogen plasma discharge treated a-C:H and ta-C coatings, *Appl. Surf. Sci.* 371 (2016) 613–623. doi:10.1016/j.apsusc.2016.02.192.

- [24] H. Notsu, I. Yagi, T. Tatsuma, D.A. Tryk, A. Fujishima, Introduction of oxygen-containing functional groups onto diamond electrode surfaces by oxygen plasma and anodic polarization, *Electrochem. Solid-State Lett.* 2 (1999) 522–524. doi:10.1149/1.1390890.
- [25] C. Zhao, G. Burrell, A. a J. Torriero, F. Separovic, N.F. Dunlop, D.R. MacFarlane, A.M. Bond, Electrochemistry of room temperature protic ionic liquids., *J. Phys. Chem. B.* 112 (2008) 6923–6936. doi:10.1021/jp711804j.
- [26] C. Cannès, H. Cachet, C. Debiemme-Chouvy, C. Deslouis, J. de Sanoit, C. Le Naour, V. a Zinovyeva, Double Layer at [BuMeIm][Tf 2 N] Ionic Liquid–Pt or –C Material Interfaces, *J. Phys. Chem. C.* 117 (2013) 22915–22925. doi:10.1021/jp407665q.
- [27] S. Ernst, L. Aldous, R.G. Compton, The electrochemical reduction of oxygen at boron-doped diamond and glassy carbon electrodes: A comparative study in a room-temperature ionic liquid, *J. Electroanal. Chem.* 663 (2011) 108–112. doi:10.1016/j.jelechem.2011.10.004.
- [28] A.J. Lucio, S.K. Shaw, J. Zhang, A.M. Bond, Double-Layer Capacitance at Ionic Liquid-Boron-Doped Diamond Electrode Interfaces Studied by Fourier Transformed Alternating Current Voltammetry, *J. Phys. Chem. C.* 122 (2018) 11777–11788. doi:10.1021/acs.jpcc.8b00272.
- [29] D.Y. Kim, J.C. Yang, H.W. Kim, G.M. Swain, Heterogeneous electron-transfer rate constants for ferrocene and ferrocene carboxylic acid at boron-doped diamond electrodes in a room temperature ionic liquid, *Electrochim. Acta.* 94 (2013) 49–56. doi:10.1016/j.electacta.2013.01.140.
- [30] K. Saravanan, S. Sathyamoorthi, D. Velayutham, V. Suryanarayanan, Voltammetric investigations on the relative deactivation of boron-doped diamond, glassy carbon and platinum electrodes during the anodic oxidation of substituted phenols in room temperature ionic liquids, *Electrochim. Acta.* 69 (2012) 71–78. doi:10.1016/j.electacta.2012.02.077.
- [31] F. Gao, G. Lewes-Malandrakis, M.T. Wolfer, W. Müller-Sebert, P. Gentile, D. Aradilla, T. Schubert, C.E. Nebel, Diamond-coated silicon wires for supercapacitor applications in ionic liquids, *Diam. Relat. Mater.* 51 (2015) 1–6. doi:10.1016/j.diamond.2014.10.009.
- [32] R. Jarošová, P.M. De Sousa Bezerra, C. Munson, G.M. Swain, Assessment of heterogeneous electron-transfer rate constants for soluble redox analytes at tetrahedral amorphous carbon, boron-doped diamond, and glassy carbon electrodes, *Phys. Status Solidi Appl. Mater. Sci.* 213 (2016) 2087–2098. doi:10.1002/pssa.201600339.
- [33] A. Tafel, M. Wu, E. Spiecker, P. Hommelhoff, J. Ristein, Fabrication and structural characterization of diamond-coated tungsten tips, (2019). <http://arxiv.org/abs/1902.01369>.
- [34] N. Wächter, C. Munson, R. Jarošová, I. Berkun, T. Hogan, R.C. Rocha-Filho, G.M. Swain, Structure, Electronic Properties, and Electrochemical Behavior of a Boron-Doped

- Diamond/Quartz Optically Transparent Electrode, *ACS Appl. Mater. Interfaces*. (2016) A-M. doi:10.1021/acsami.6b02467.
- [35] V. Seshan, D. Ullien, A. Castellanos-Gomez, S. Sachdeva, D.H.K. Murthy, T.J. Savenije, H.A. Ahmad, T.S. Nunney, S.D. Janssens, K. Haenen, M. Nesládek, H.S.J. Van Der Zant, E.J.R. Sudhölter, L.C.P.M. De Smet, Hydrogen termination of CVD diamond films by high-temperature annealing at atmospheric pressure, *J. Chem. Phys.* 138 (2013). doi:10.1063/1.4810866.
 - [36] H. Kawai, Hydrogen-terminated diamond surfaces and interfaces, *Surf. Sci. Rep.* 26 (1996) 205–259. doi:10.1016/S0167-5729(97)80002-7.
 - [37] Y. Show, V.M. Swope, G.M. Swain, The effect of the CH₄ level on the morphology, microstructure, phase purity and electrochemical properties of carbon films deposited by microwave-assisted CVD from Ar-rich source gas mixtures, *Diam. Relat. Mater.* 18 (2009) 1426–1434. doi:10.1016/j.diamond.2009.09.011.
 - [38] R. Jarosova, G.M. Swain, Rapid Preparation of Room Temperature Ionic Liquids with Low Water Content as Characterized with a ta-C:N Electrode, *J. Electrochem. Soc.* 162 (2015) H507–H511. doi:10.1149/2.0191508jes.
 - [39] M.C. Granger, M. Witek, J. Xu, J. Wang, M. Hupert, A. Hanks, M.D. Koppang, J.E. Butler, G. Lucazeau, M. Mermoux, J.W. Strojek, G.M. Swain, Standard electrochemical behavior of high-quality, boron-doped polycrystalline diamond thin-film electrodes, *Anal. Chem.* 72 (2000) 3793–3804. doi:10.1021/ac0000675.
 - [40] K.D. Gnahn M, Pajkossy T, The interface between Au(111) and an ionic liquid, *Electrochim. Acta.* 55 (2010) 6212–6217. doi:10.1016/j.electacta.2009.08.031.
 - [41] M. Balabajew, B. Roling, Minimizing Artifacts in Three-electrode Double Layer Capacitance Measurements Caused by Stray Capacitances, *Electrochim. Acta.* 176 (2015) 907–918. doi:10.1016/j.electacta.2015.07.074.
 - [42] J. Wallauer, M. Balabajew, B. Roling, Impedance Spectroscopy on Electrode | Ionic Liquid Interfaces, 2017. doi:10.1002/9783527682706.ch11.
 - [43] A.J. Lucio, S.K. Shaw, Effects and controls of capacitive hysteresis in ionic liquid electrochemical measurements, *Analyst.* 143 (2018) 4887–4900. doi:10.1039/c8an01085d.
 - [44] W. Zhou, Y. Xu, Y. Ouchi, Hysteresis Effects in the In Situ SFG and Differential Capacitance Measurements on Metal Electrode/Ionic Liquids Interface, *ECS Trans.* 50 (2013) 339–348. doi:10.1149/05011.0339ecst.
 - [45] M.M. Islam, M.T. Alam, T. Ohsaka, Electrical Double-Layer Structure in Ionic Liquids: A Corroboration of the Theoretical Model by Experimental Results, *J. Phys. Chem. C.* 112 (2008) 16568–16574. doi:10.1021/jp8058849.

- [46] M.T. Alam, M.M. Islam, T. Okajima, T. Ohsaka, Capacitance measurements in a series of room-temperature ionic liquids at glassy carbon and gold electrode interfaces, *J. Phys. Chem. C*. 112 (2008) 16600–16608. doi:10.1021/jp804620m.
- [47] M.T. Alam, J. Masud, M.M. Islam, T. Okajima, T. Ohsaka, Differential Capacitance at Au(111) in 1-Alkyl-3-methylimidazolium Tetrafluoroborate Based Room-Temperature Ionic Liquids, *J. Phys. Chem. C*. 115 (2011) 19797–19804. doi:10.1021/jp205800x.
- [48] L.J. Small, D.R. Wheeler, Influence of Analysis Method on the Experimentally Observed Capacitance at the Gold-Ionic Liquid Interface, *J. Electrochem. Soc.* 161 (2014) H260–H263. doi:10.1149/2.094404jes.
- [49] T.R. Gore, T. Bond, W. Zhang, R.W.J. Scott, I.J. Burgess, Hysteresis in the measurement of double-layer capacitance at the gold-ionic liquid interface, *Electrochem. Commun.* 12 (2010) 1340–1343. doi:10.1016/j.elecom.2010.07.015.
- [50] V. Lockett, R. Sedev, J.R. Horne, T. Rodopoulos, Differential Capacitance of the Electrical Double Layer in Imidazolium-Based Ionic Liquids : Influence of Potential , Cation Size , and Temperature Differential Capacitance of the Electrical Double Layer in Imidazolium-Based Ionic Liquids : Influence of P, (2008) 7486–7495. doi:10.1021/jp7100732.
- [51] R. Atkin, N. Borisenko, M. Drüschler, F. Endres, R. Hayes, B. Huber, B. Roling, Structure and dynamics of the interfacial layer between ionic liquids and electrode materials, *J. Mol. Liq.* 192 (2014) 44–54. doi:10.1016/j.molliq.2013.08.006.
- [52] C.H. Kim, S. Il Pyun, J.H. Kim, An investigation of the capacitance dispersion on the fractal carbon electrode with edge and basal orientations, *Electrochim. Acta.* 48 (2003) 3455–3463. doi:10.1016/S0013-4686(03)00464-X.
- [53] B. Lesiak, L. Kövér, J. Tóth, J. Zemek, P. Jiricek, A. Kromka, N. Rangam, C sp 2 / sp 3 hybridisations in carbon nanomaterials – XPS and (X) AES study, 452 (2018) 223–231. doi:10.1016/j.apsusc.2018.04.269.
- [54] J.I.B. Wilson, J.S. Walton, G. Beamson, Analysis of chemical vapour deposited diamond films by X-ray photoelectron spectroscopy, *J. Electron Spectros. Relat. Phenomena.* 121 (2001) 183–201. doi:10.1016/S0368-2048(01)00334-6.
- [55] R. Graupner, F. Maier, J. Ristein, L. Ley, C. Jung, High-resolution surface-sensitive C core-level spectra of clean and hydrogen-terminated diamond (100) and (111) surfaces, *Phys. Rev. B - Condens. Matter Mater. Phys.* 57 (1998) 12397–12409. doi:10.1103/PhysRevB.57.12397.
- [56] D. Steinmu, F.R. Kloss, M. Najam-ul-haq, M. Rainer, K. Larsson, C. Linsmeier, G. Ko, C. Fehrer, X. Liu, N. Memmel, E. Bertel, C.W. Huck, R. Gassner, Strong binding of bioactive BMP-2 to nanocrystalline diamond by physisorption, 27 (2006) 4547–4556. doi:10.1016/j.biomaterials.2006.04.036.

- [57] I. Yagi, H. Notsu, T. Kondo, D.A. Tryk, A. Fujishima, Electrochemical selectivity for redox systems at oxygen-terminated diamond electrodes, 473 (1999) 173–178.
- [58] P.E. Pehrsson, T.W. Mercer, Oxidation of the hydrogenated diamond (100) surface, 460 (2000) 49–66.
- [59] H. Notsu, I. Yagi, T. Tatsuma, D.A. Tryk, A. Fujishima, Surface carbonyl groups on oxidized diamond electrodes, 492 (2000) 31–37.
- [60] H. Notsu, T. Fukazawa, T. Tatsuma, D.A. Tryk, Hydroxyl Groups on Boron-Doped Diamond Electrodes and Their Modification with a Silane Coupling Agent, (2001) 7–9. doi:10.1149/1.1346556.
- [61] R.G. Compton, C.H. Goeting, F. Marken, A. Gutie, J.S. Foord, Electrochemically induced surface modifications of boron-doped diamond electrodes: an X-ray photoelectron spectroscopy study, 9 (2000) 390–396.
- [62] A. Proctor, P.M.A. Sherwood, X-ray photoelectron spectroscopic studies of carbon fibre surfaces. I. carbon fibre spectra and the effects of heat treatment, J. Electron Spectros. Relat. Phenomena. 27 (1982) 39–56. doi:10.1016/0368-2048(82)85051-2.
- [63] C.L. Cheng, H.C. Chang, J.C. Lin, K.J. Song, J.K. Wang, Direct observation of hydrogen etching anisotropy on diamond single crystal surfaces, Phys. Rev. Lett. 78 (1997) 3713–3716. doi:10.1103/PhysRevLett.78.3713.
- [64] E. Mahé, D. Devilliers, C. Comninellis, Electrochemical reactivity at graphitic microdomains on polycrystalline boron doped diamond thin-films electrodes, Electrochim. Acta. 50 (2005) 2263–2277. doi:10.1016/j.electacta.2004.10.060.
- [65] R.S. Anareddy, A.J. Lucio, S.K. Shaw, Adventitious Water Sorption in a Hydrophilic and a Hydrophobic Ionic Liquid: Analysis and Implications, (2016). doi:10.1021/acsomega.6b00104.
- [66] Y.Z. Su, Y.C. Fu, J.W. Yon, Z. Bin Chen, B.W. Mao, Double layer of Au(100)/ionic liquid interface and its stability in imidazolium-based ionic liquids, Angew. Chemie - Int. Ed. 48 (2009) 5148–5151. doi:10.1002/anie.200900300.
- [67] M.T. Alam, M. Mominul Islam, T. Okajima, T. Ohsaka, Measurements of differential capacitance in room temperature ionic liquid at mercury, glassy carbon and gold electrode interfaces, Electrochem. Commun. 9 (2007) 2370–2374. doi:10.1016/j.elecom.2007.07.009.
- [68] S. Baldelli, Surface structure at the ionic liquid-electrified metal interface, Acc. Chem. Res. 41 (2008) 421–431. doi:10.1021/ar700185h.
- [69] S. Deheryan, D. J. Cott, P. W. Mertens, M. Heyns, P. M. Vereecken, Direct correlation between the measured electrochemical capacitance, wettability and surface functional

groups of CarbonNanosheets, *Electrochim. Acta.* 132 (2014) 574–582.
doi:10.1016/j.electacta.2014.03.148.

Chapter 5

Effect of Nitrogen Incorporation on Electrode Microstructure, Voltammetric Properties and Capacitance of Nitrogen-Incorporated Tetrahedral Amorphous Carbon Thin-Film Electrodes

5.1 Introduction

Diamond-like carbons are one class of carbon electrodes that have lately become extremely attractive to the electrochemistry community. Enhanced interest in these materials stems from their advantageous physical, chemical, and electrochemical properties, which can be tuned by varying the ratio of sp^2/sp^3 -bonded carbon content during film growth. While the graphitic carbons and diamonds have been extensively investigated over the last four decades, and their structure-property relationships are well-established [1] [2], diamond-like carbons remain comparatively under-explored.

One of the diamond-like carbons is nitrogen-incorporated tetrahedral amorphous carbon ($ta-C:N$). Its physical, chemical, electrical, and electrochemical properties are governed by the ratio of sp^2 clustering and the heteroatom (nitrogen) incorporation. $ta-C:N$ electrodes contain a mixture of sp^2 carbon clusters and sp^3 carbon domains. Incorporation of nitrogen has emerged as one of the important tools available to modulate the electronic and interfacial chemistry as well as the physicochemical properties of the electrode. The addition of nitrogen to amorphous carbon electrode usually has complex and multifaceted effects such as a change in the semiconducting/metallic character [3], surface wettability [4], electron-transfer kinetics and double-layer capacitance. Owing to the relatively higher content of sp^3 -bonded carbon, $ta-C:N$ boasts of some of diamond's superlative properties like excellent mechanical strength, high

thermal conductivity, low background current, and anti-fouling nature. There is a great interest in understanding how best to tailor the growth parameters to tune the interfacial capacitance, surface chemistry and bulk electronic properties in *ta*-C:N electrodes. Characterizing the material properties of electrodes is critically important to understand and optimize the growth parameters to tune the electrode for a particular electrochemical application.

This chapter is focused on the detailed characterization of physical, chemical and electronic properties of *ta*-C:N_x films with different nitrogen content and correlate how the microstructure (sp²/sp³), chemical composition (surface and bulk), and electronic properties correlate with electrochemical performance including available potential window, voltammetric background current and potential-dependent capacitance in RTILs. The electrochemical properties were investigated using cyclic voltammetry (CV) and electrochemical impedance spectroscopy (EIS). Comparative measurements were made for glassy carbon (pure sp² carbon) and BDD (pure sp³ carbon).

5.2 Materials and Method

5.2.1 RTILs

The ultrapure grade RTIL, 1-hexyl-3-methylimidazolium hexafluorophosphate [HMIM][PF₆] (IL-0018-UP), was procured from a commercial source, IoLiTec (Ionic Liquids Technologies GmbH), Tuscaloosa, AL, $\geq 99.5\%$ purity, water content below 100 ppm). Unless otherwise stated, the RTIL samples were mixed with activated charcoal (Sigma-Aldrich) and stirred vigorously using a magnetic plate for two days. Then, the samples were left undisturbed for two weeks to allow the charcoal powder to settle at the bottom of a 20-mL glass vial. The RTIL

was then filtered using a 0.2 μm Teflon syringe filter (Whatman) directly into the electrochemical cell. Approximately 0.5 mL of RTIL was used for each experiment. The RTIL sample was then heated at 70 $^{\circ}\text{C}$ for 60 minutes while purging with ultrahigh purity Ar (99.999%) at a high flow rate. The Ar gas was passed through drierite desiccants twice before introducing into the dry- N_2 filled glove box (Coy Laboratories). To remove any dissolved oxygen or carbon dioxide, the RTIL was sparged with ultrapure Ar at least 15 minutes prior to the experiments, and a blanket of Ar was maintained over the RTIL during the experiments. All glassware used was washed using Alconox/ultrapure water solution and then triply rinsed sequentially with deionized water, isopropanol, acetone, and ultrapure water, and finally dried in an oven at 150 $^{\circ}\text{C}$ for at least 12 h before use. All preparation and the electrochemical measurements were done in a dry N_2 purged glove box (Coy Laboratories, Grass Lake, MI). The relative humidity in the glove box was maintained at 0.0 % or below the detection limit (0.1%) of a digital hygrometer.

5.2.2 Electrodes

5.2.2.1 Nitrogen-Incorporated Tetrahedral Amorphous Carbon Thin Film Electrodes

The *ta*-C:N films were grown on a boron-doped Si (111) (Virginia Semiconductor, Fredericksburg, VA; 10^{-3} $\Omega\text{-cm}$) using a Laser-Arc physical vapor deposition system at the Fraunhofer Center for Coatings and Diamond Technologies, MSU. The deposition method is based on laser-controlled, high-current cathodic vacuum arc deposition [5–9]. A pulsed-laser beam is rastered across a rotating high-purity graphite target that serves as the cathode. Each laser pulse generates small localized plasma that delivers free charge carriers for the arc discharge. The arc discharge lasts only 125 μs before the laser triggers a new, staggered plasma across the graphite

cathode. This discharge consists of highly ionized C atoms and small ionized carbon atom clusters that are accelerated toward the substrate (grounded mode). This process produces hard (30 – 60 GPa) and dense *ta*-C films. The substrate-target distance was approximately 30 cm. The substrates were rotated during the growth to obtain uniform film deposition. The arc evaporation is associated with the emission of microparticles of carbon originating from the graphite drum (*i.e.*, cathode surface) [9]. These particles can get incorporated into the growing film and impact surface roughness. The nitrogen-incorporated films were deposited in the presence of N₂ gas at a flow rate of 10, 30 and 50 sccm, a pulse rate of 350 Hz and a peak arc current of > 100 A. Increased levels of nitrogen in the chamber leads to increased nitrogen incorporation into the film and increased electrical conductivity [10–12]. The substrate temperature during the deposition was below 100 °C. The film growth rate was 2-3 μm/h.

5.2.2.2 Boron-Doped Diamond Electrodes

The boron-doped nanocrystalline diamond (BDD) thin-films were grown on a p-Si (111) substrate (Virginia Semiconductor, Inc. Fredricksburg, VA, ~ 0.001 Ω-cm) by microwave-assisted chemical vapor deposition (CVD). A commercial 1.5 kW reactor (Seki Technotron) was used [6]. The silicon substrate was seeded ultrasonically with nanodiamond particles from an Opal seed suspension (Adámas Nanotechnologies Inc., Raleigh, NC) for 30 minutes in a glass beaker. This suspension contains aggregates (~30 nm) of detonation diamond particles in dimethyl sulfoxide (DMSO). The seeded substrate was then rinsed 3x with ultrapure water followed by wick-drying using a Kimwipe and full drying with a stream of N₂ before being placed in the CVD reactor for overnight pump-down. The BDD film was grown using methane diluted in hydrogen (C/H = 1%,

v/v) at a total gas flow rate of 200 sccm (standard cubic centimeter per minute), a system pressure of 35 Torr, an estimated substrate temperature near 825 °C, and a growth time of 5-6 h. Boron doping was accomplished by adding 0.1% (v/v) diborane in hydrogen to the source gas, producing a gas-phase concentration of 10 ppm. After deposition, the methane and diborane flows were stopped, and the coated substrate was cooled under a hydrogen plasma for 30 min by slowly reducing the power and pressure down to 150 W and 10 Torr. This post-growth cooling step is critical to minimize the formation of sp²-bonded carbon at the surface that would result from the desorption of surface hydrogen (T ~ 450 °C) and reconstruction of the surface carbon atoms if the plasma was extinguished at the growth temperature [13]. The cooling step in atomic hydrogen is critical for maintaining a hydrogen-terminated surface [14]. The doping level was estimated to be in the low 10²¹ cm⁻³ range based on Raman spectroscopy and Hall effect measurement data of other films deposited using similar conditions [15]. Film thicknesses were 2 - 4 μm, as estimated by the change in weight of the substrate after film deposition and cross-sectional SEM micrographs.

5.2.2.3 Glassy Carbon Electrodes

The glassy carbon (GC-20, Tokai Ltd.) electrode was polished with 1.0, 0.3 and 0.05 μm diameter Micropolish II alumina powder (Buehler) on microcloth PSA (Buehler) pads, sequentially with ten minutes of each step. The alumina powder was slurried with deionized water, and the polishing was performed manually in an 'eight' digit shape with slight pressure on the electrode [16]. The electrode was rinsed with deionized water to remove alumina powder debris and sonicated in isopropanol for ten minutes after each polishing step. Finally, the electrode was

rinsed with copious deionized water and ultrasonically cleaned for 20 minutes to remove any polishing debris. The electrodes were immediately used for the electrochemical measurements.

5.2.3 Characterization Techniques

5.2.3.1 Visible Raman Spectroscopy

Visible Raman spectroscopy was performed using a Renishaw *in Via Reflex* Confocal Raman microscope equipped with a Nd:YAG laser source. The excitation wavelength was 532 nm. Spectra were acquired with *Wire* Interface software using a laser power of 0.45 W (1% of 45W maximum power) at the sample and 1800 lines mm⁻¹ grating. Spectra were acquired at single spots. The typical integration time per spectrum was 10 s. The Raman spectrometer was calibrated with a Type IIa single-crystal diamond standard (phonon line at 1332 cm⁻¹). The Raman spectra of *ta*-C:N_x films were fitted using Voigt (Gaussian/Lorentzian, 0.8) function peak.

5.2.3.2 X-ray Photoelectron Spectroscopy

The chemical composition of the BDD films in the near-surface region was determined using X-ray photoelectron spectroscopy (XPS). XPS spectra were recorded using a Perkin-Elmer PHI 5400 ESCA system with a high-intensity monochromatic X-ray source (Al K α). Samples were analyzed at a base pressure of 10⁻⁹ Torr with a take-off angle of 45 ° using a pass energy of 29.35 eV. The X-ray power was 350 W, and scans were acquired over a 250 μ m² area. The instrument was calibrated using the C1s peak for HOPG (highly ordered pyrolytic graphite) at 284.5 eV as an internal reference. The atomic percentage of each element was calculated from the peak areas

divided by relative sensitivity factors for the PHI 5400 system. The deconvolution of core-level spectra was accomplished using MultiPAK v.8.2.0. Software. The spectra were fit to a Gaussian-Lorentzian (G/L = 0.8) peak shape after Shirley background correction to calculate the elemental atomic ratios.

5.2.3.3 High-Resolution Transmission Electron Microscopy (HR-TEM)

HRTEM images were collected using a field-emission microscope (JEOL-2200FS, Tokyo, Japan) operating at 200 kV. A Gatan 1024 x 1024 UltraScan 4000 CCD camera was used to capture digital HR-TEM images.

5.2.3.4 Electron Energy Loss Spectroscopy (EELS)

Small-spot EELS measurements were made in scanning transmission electron microscopy mode (STEM). A Cu grid was used as a substrate. The *ta*-C:N_x films were grown directly on the Formavar (carbon-coated Cu grid), Ted-Pella#01883-F. The grid had holes of ~1 μm diameter with ~4 μm spacing in between the holes. The thin sections of *ta*-C:N film hanging freely in between the voids were used to collect the HR-TEM images. Multiwalled carbon nanotubes (CNTs) were used as a standard for sp² carbon. To minimize contamination, the measurements were performed at liquid nitrogen temperature. The sp² content was calculated from peak area under π* and σ* excitations with peak center at 285 and 291.1 eV, respectively [17].

$$sp^2 = \frac{area(\pi^*)}{area(\pi^* + \sigma^*)}$$

5.2.4 Electrochemical Techniques

A single-compartment glass cell was used in a three-electrode measurement configuration [18]. The working electrode (BDD) was clamped to the bottom of the cell. The backside electrical contact was made to the BDD electrode by scratching the conducting p-Si substrate with SiC 800 grit paper, and then cleaning and coating the area with a layer of carbon from a pencil. This procedure produces a good ohmic contact between the working electrode and a copper current collector plate. A Viton™ O-ring between the cell and the working electrode defined the exposed geometric area of 0.2 cm². The counter electrode was a high purity platinum wire (0.5 mm diam.) sealed in glass, and a large area, spiral silver wire served as the quasi-reference electrode (Ag QRE). The potential of the Ag QRE in 0.5 mol L⁻¹ H₂SO₄ was 130 ± 4 mV vs. Ag/AgCl (3M KCl). Approximately 0.5 mL of ionic liquid was used for an experiment. Ar gas (99.9999% Praxair Inc.) blanketed the RTIL during an experiment with all the electrochemical experiments being performed at room temperature in a dry N₂-purged vinyl glove box. All glassware was washed with detergent and then rinsed sequentially with deionized water, isopropanol, acetone, and ultrapure water, and finally, dried in an oven at 150 °C for at least 12 h before use. The ultrapure water was obtained by passing house deionized water through a Barnstead E-Pure System (ion exchange and activated carbon columns, Thermo Scientific, USA). The ultrapure water had an electrical resistivity of > 17 MΩ-cm.

5.2.4.1 Cyclic Voltammetry

Cyclic voltammetry (CV) measurements were made using a computer-controlled potentiostat (Model 660D, CH Instruments Inc., Austin, TX). CVs were recorded as a function of

scan rate (0.01, 0.03, 0.05, 0.1, 0.2, 0.3, 0.4, 0.5 V s⁻¹) and the capacitance was calculated from the slope of background current at 0.2 V vs. scan rate plots using equation,

$$j_{average} = C_{dl}v \quad (i)$$

where $j_{average}$ (A cm⁻²) is average background current density from the positive-going and negative-going sweeps at a specific potential, C_{dl} (F cm⁻²) is the double-layer capacitance, and v (V s⁻¹) is the potential scan rate.

5.2.4.2 Electrochemical Impedance Spectroscopy

Electrochemical impedance spectroscopy (EIS) was performed at different applied DC potentials using a broad frequency spectrum from 0.1 to 10⁵ Hz with 20 data points collected per decade. A sinusoidal perturbation voltage of 10 mV (rms) was added to each negative-to positive-going DC applied potential in 200 mV increments. An equilibration time of 200 s was allowed before the acquisition of the impedance data at each potential. The full frequency EIS data were analyzed in the Nyquist plane using the CPE-based electrical equivalent circuit shown in Figure 5.1. R_s represents bulk electrolyte resistance and any electrode ohmic resistance in series with a parallel-connected constant phase element (CPE), C_{hf} is the high-frequency capacitance associated with the external electrical leads. As mentioned, the origin of C_{hf} is the capacitance that arises from the connecting electrical leads [19]. C_{hf} is usually in the range of nF and is potential-independent at the higher frequencies.

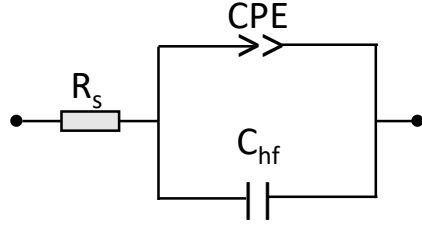


Figure 5.1. The representative electrical equivalent circuit that was used to fit the full-frequency impedance data.

In the Nyquist plot format, a pure capacitor exhibits frequency-independent impedance and produces a straight vertical line along the Z'' (imaginary) – Z' (real) plane in this plot. Polycrystalline electrodes are well known to exhibit a capacitance dispersion with frequency due to the atomic scale defects (steps, kinks, dislocations) and surface roughness (corrugations, grooves) that lead to inhomogeneities in the current density and local distribution of response time constants [38, 39]. The simplest way to compensate for this inhomogeneity is to use a CPE element that accounts for the frequency-dependent capacitance according to:

$$Z_{CPE} = \frac{1}{Q(j.2\pi f)^\alpha} \quad (2)$$

where Z_{CPE} is the impedance for a CPE element in Ω , f is AC frequency in Hz, Q is the effective capacitance for a CPE element in $\Omega^{-1} s^\alpha$ and α is 1 for an ideal capacitor whose phase angle of -90° and less than 1 for a phase angle less than $(-90^\circ * \alpha)$. EIS measures the total impedance response of the system. To separate impedance of individual components, one must interpret the impedance data based on the behavior of an appropriate equivalent electrical circuit. At lower frequencies, the capacitor gets charged, and the current increases at a decreasing rate, as predicted

by the circuit's time constant. At higher frequencies, the capacitor acts as a short, and the resistance dominates the system. This inflection point is known as “knee frequency”.

5.3 Results

5.3.1 X-ray Photoelectron Spectroscopy (XPS)

XPS was used to determine the sp^2 and sp^3 bonded carbon ratio in the films and the atomic O, N, and C signals in the near-surface of the ta -C:N films. Figure 5.2 compares the elemental survey scans for ta -C:N₀ (black curve), ta -C:N₁₀ (red curve), ta -C:N₃₀ (blue curve), and ta -C:N₅₀ (pink curve) films. The highlighted regions show binding energy for C1s (280 to 292 eV), N1s (394 to 406 eV), and O1s (528 to 536 eV). No other element was observed at a detectable level.

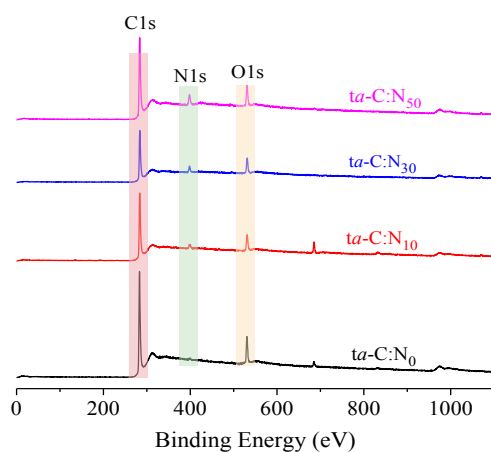


Figure 5.2. XPS survey spectra of ta -C:N₀ (black curve), ta -C:N₁₀ (red curve), ta -C:N₃₀ (blue curve), and ta -C:N₅₀ (pink curve) films over a wide energy range from 0 to 1100 eV. The highlighted areas represent C1s, N1s, and O1s region *ca.* 285, 400, and 530 eV, respectively.

Table 5.1 shows the relative elemental composition of ta -C:N_x films. A low level of surface oxygen (9 to 12%) was observed due to exposure to the laboratory air for extended periods before XPS measurements. The oxygen levels are relatively constant for all ta -C:N_x films. However, the

nitrogen atomic ratio (N/C) increases from *ca.* 1 to 4, 6, and 8 % for *ta*-C:N₀, *ta*-C:N₁₀, *ta*-C:N₃₀, and *ta*-C:N₅₀, respectively. The relatively constant O/C and increasing N/C ratio with increases in the flow of nitrogen during growth can be distinctly observed in Figure 5.3.

Table 5.1. Summary of the relative elemental composition of *ta*-C:N_x films calculated using XPS. The % ratios were calculated by integrating the peak area for the respective elements. Shirley background subtraction method was used to define the baseline.

| Sample | C1s (%) | N1s (%) | O1s (%) | O/C | N/C |
|------------------------------|--------------|-------------|--------------|---------------|---------------|
| <i>ta</i> -C:N ₀ | 87.94 ± 1.36 | 1.02 ± 0.38 | 11.04 ± 0.99 | 0.139 ± 0.013 | 0.016 ± 0.005 |
| <i>ta</i> -C:N ₁₀ | 85.07 ± 1.46 | 4.15 ± 1.14 | 10.78 ± 2.61 | 0.160 ± 0.034 | 0.036 ± 0.079 |
| <i>ta</i> -C:N ₃₀ | 81.61 ± 1.15 | 6.08 ± 1.36 | 12.31 ± 0.21 | 0.148 ± 0.008 | 0.079 ± 0.025 |
| <i>ta</i> -C:N ₅₀ | 82.58 ± 2.51 | 7.93 ± 0.59 | 9.48 ± 1.93 | 0.143 ± 0.028 | 0.096 ± 0.010 |

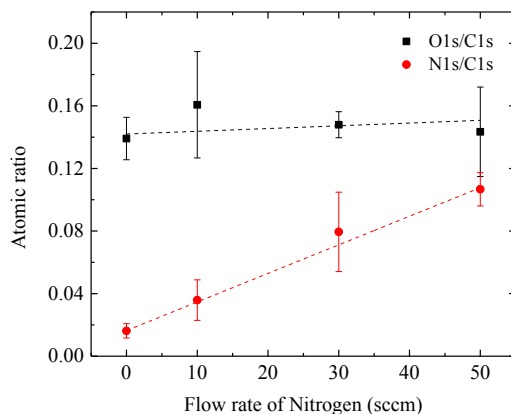


Figure 5.3. Plots of the N/C (●) and O/C (■) atomic ratios as a function of nitrogen flow rate during the growth of *ta*-C:N_x films. The ratios were calculated from C1s, N1s and O1s peak area integration. The error bar represents standard deviation. (n = 2).

Figure 5.4 shows deconvoluted XPS spectra of C1s energy region for (A) *ta*-C:N₀, (B) *ta*-C:N₁₀, (C) *ta*-C:N₃₀, and (D) *ta*-C:N₅₀. Deconvolution of C1s peak reveals two dominant signals at 283.6 eV, which is assigned to sp² C and at 284.6 eV, which corresponds to sp³ C. Three other peaks were observed for C-N, C=N, and C=O functional groups at *ca.* 285.5, 286.6, and 287.5 eV respectively. Table 5.2 shows relative peak area (%) of these functional groups for *ta*-C:N_x films.

The relative area of sp^2 peak increases from 55.4% for $ta-C:N_0$ to 63.2% for $ta-C:N_{10}$, 67.3% for $ta-C:N_{30}$, and 69.74 % for $ta-C:N_{50}$. Consequently, the peak area for sp^3 carbon decreases from 35.55% for $ta-C:N_0$ to 25.13% for $ta-C:N_{10}$, 21.49% for $ta-C:N_{30}$, and 20.59% for $ta-C:N_{50}$ with increasing nitrogen flow rate during film growth. The higher-binding-energy components correspond to carbon-nitrogen (C-N and C=N) and carbon-oxygen (C=O) functional groups. Importantly, more nitrogen was observed at the surface for the films grown with a higher nitrogen flow rate during deposition, and the sp^2 C component increased with the nitrogen content at the surface [20].

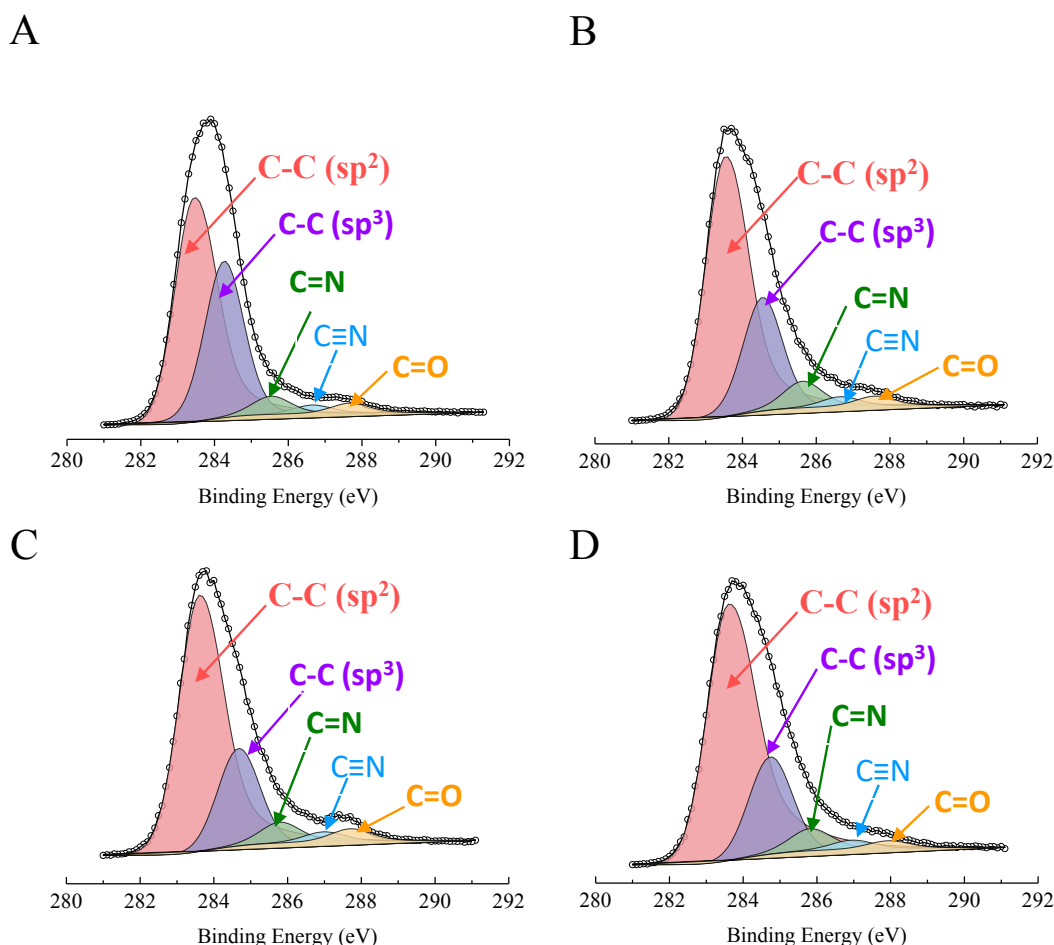


Figure 5.4. Deconvoluted peak fits of core C1s energy region of the XPS spectra showing sp^2 C, sp^3 C, C-N, C=N and C=O functional groups for $ta-C:N_x$ films: (A) $ta-C:N_0$, (B) $ta-C:N_{10}$, (C) $ta-C:N_{30}$, and (D) $ta-C:N_{50}$.

Table 5.2. Details of C1s peak components for *ta*-C:N_x= 0, 10, 30, 50 thin films.

| ta-C:N₀ | | | | ta-C:N₁₀ | | | |
|---------------------------|-----------|---------------|---------------------|----------------------------|-----------|---------------|---------------------|
| Peak (eV) | FWHM (eV) | Peak Area (%) | Chemical bond | Peak (eV) | FWHM (eV) | Peak Area (%) | Chemical bond |
| 283.46 | 1.36 | 55.37 | C-C sp ² | 283.61 | 1.39 | 63.72 | C-C sp ² |
| 284.26 | 1.25 | 35.55 | C-C sp ³ | 284.64 | 1.26 | 25.13 | C-C sp ³ |
| 285.54 | 1.25 | 4.47 | C-N | 285.61 | 1.26 | 6.34 | C-N |
| 286.66 | 1.25 | 2.13 | C=N | 286.75 | 1.26 | 2.41 | C=N |
| 287.68 | 1.25 | 2.48 | C=O | 287.76 | 1.26 | 2.40 | C=O |

| ta-C:N₃₀ | | | | ta-C:N₅₀ | | | |
|----------------------------|-----------|---------------|---------------------|----------------------------|-----------|---------------|---------------------|
| Peak (eV) | FWHM (eV) | Peak Area (%) | Chemical bond | Peak (eV) | FWHM (eV) | Peak Area (%) | Chemical bond |
| 283.62 | 1.45 | 67.32 | C-C sp ² | 283.61 | 1.58 | 69.74 | C-C sp ² |
| 284.68 | 1.33 | 21.49 | C-C sp ³ | 284.74 | 1.37 | 20.59 | C-C sp ³ |
| 285.80 | 1.33 | 5.32 | C-N | 285.83 | 1.37 | 5.4 | C-N |
| 286.99 | 1.33 | 2.62 | C=N | 286.96 | 1.37 | 2.3 | C=N |
| 287.72 | 1.33 | 3.25 | C=O | 287.95 | 1.37 | 1.96 | C=O |

Figure 5.5 shows the deconvoluted core N1s peak fits for nitrogen-oxygen and nitrogen-carbon functional groups. *ta*-C:N₀ film (A) shows two major components at 398.5 and 400.4 eV corresponding to C≡N (34.8%) and C=N (65.2%) groups, respectively. *ta*-C:N₁₀ (B) shows three components at 397.5, 398.8, and 400.5 eV and are assigned to C-N (23.6%), C≡N (71.1%) and C=N (5.3%), respectively [21]. *ta*-C:N₃₀ (C) shows three components at 397.4, 398.6, and 400.8 eV and are assigned to C-N (9%), C≡N (56.2%) and C=N (34.8%), respectively [21]. *ta*-C:N₅₀ (D) films also shows three components at 397.6, 398.9, and 400.6 eV, which are assigned to C-N (33.2%), C=N (58.9%), and C≡N (8%), respectively.

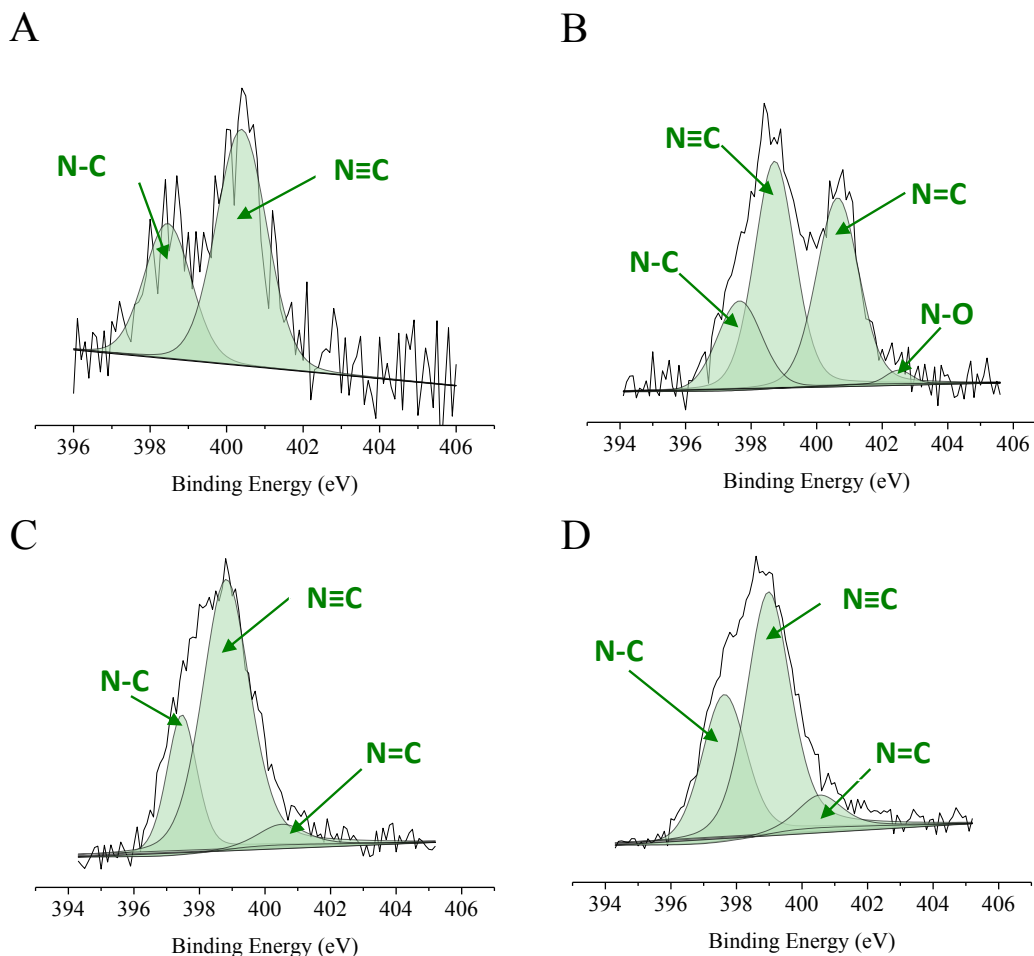


Figure 5.5. Deconvoluted peak fits of core N1s energy region of the XPS spectra showing nitrogen-oxygen and nitrogen-carbon functional groups for *ta*-C:N_x films: (A) *ta*-C:N₀, (B) *ta*-C:N₁₀, (C) *ta*-C:N₃₀, and (D) *ta*-C:N₅₀.

Figure 5.6 shows the deconvoluted core O1s peak fits for oxygen-carbon functional groups. *ta*-C:N₀ film (A) shows two major components at 531.2 and 532.3 eV corresponding to O=C sp² (70.8%) and OH-C sp³ (29.2%) groups, respectively [20]. *ta*-C:N₁₀ (B) shows two components at 531.0 eV and 532.34 eV and are assigned to O=C sp² (62.6%), OH-C sp³ (37.4%), respectively. *ta*-C:N₃₀ (C) shows two components at 531.0 eV and 532.2 eV and are assigned to O=C sp² (59.3%), OH-C sp³ (40.72%). *ta*-C:N₃₀ (D) films also shows two components at 531.1 and 532.2 eV, which are assigned to O=C sp² (62.16%), OH-C sp³ (34.8%).

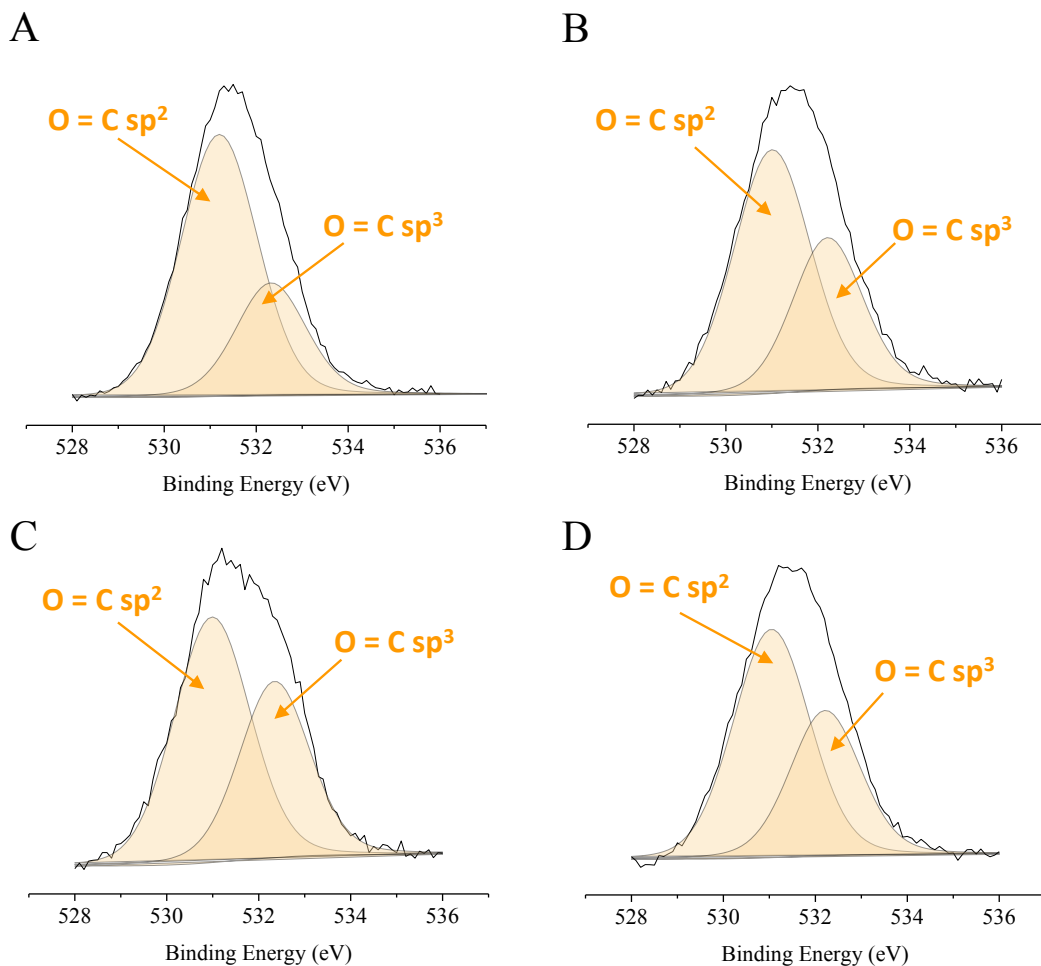


Figure 5.6. Deconvoluted peak fits of core O1s energy region of the XPS spectra showing oxygen-sp² C and oxygen-sp³ C functional groups for *ta*-C:N_x films: (A) *ta*-C:N₀, (B) *ta*-C:N₁₀, (C) *ta*-C:N₃₀, and (D) *ta*-C:N₅₀.

Table 5.3 compares the relative atomic ratio of sp²/sp³-bonded carbon on the surface of *ta*-C:N_x films. The sp² carbon content increases from 1.56% for *ta*-C:N₀, to 2.54% for *ta*-C:N₁₀, 3.13% for *ta*-C:N₃₀, and 3.39% for *ta*-C:N₅₀. The XPS data reveal that the sp²-bonded carbon on the surface of *ta*-C:N_x films increases significantly with the nitrogen content.

Table 5.3. Summary of XPS data showing sp^2/sp^3 carbon content calculated from deconvoluted spectra of C1s for $ta-C:N_x$ thin-films electrodes. ($n = 6$).

| Sample | sp^2/sp^3 C | Std. deviation ($n = 3$) |
|---------------|---------------|-------------------------------|
| $ta-C:N_0$ | 1.56 | 0.406 |
| $ta-C:N_{10}$ | 2.54 | 0.041 |
| $ta-C:N_{30}$ | 3.13 | 0.440 |
| $ta-C:N_{50}$ | 3.39 | 0.071 |

5.3.2 Raman Spectroscopy

Visible Raman spectroscopy was used to probe the microstructure of the three-electrode films used in the study. Figure 5.6 shows the visible Raman spectra for BDD (blue curve), GC (black curve), and $ta-C:N_{30}$ (red curve) electrodes in the range of 100-1900 cm^{-1} . These spectra are representative of six spectra recorded at the outer four quadrants and center of the films. The spectra obtained at different spots overlap. This indicates that the microstructure is uniform across the electrode. Multiple peaks were seen for BDD. The BDD spectrum shows intense sharp peaks at 520 and 1328 cm^{-1} with FWHM of 11.5 cm^{-1} accompanied with broad shoulder peaks at 980 and 1215 cm^{-1} . The first-order signature diamond phonon line is observed at 1332 cm^{-1} [22]. This peak is usually shifted to lower wavenumbers for heavily-doped diamond films. For these films, it is shifted to 1328 cm^{-1} , indicative of intrinsic stress in the film due to boron incorporation [23]. This shift is accompanied by an increase in intensity at 488 and 1215 cm^{-1} [22]. The scattering at 488 cm^{-1} overlaps with the signal from Si substrate at 520 cm^{-1} . This peak increases with boron doping levels and has been assigned to the vibration modes of boron dimers and clusters [24] [25]. The peak at 1215 cm^{-1} arises due to defects in the diamond lattice brought about by high doping levels, mainly due to carbon-boron complexes. The broad shoulder *ca.* 1100 cm^{-1} and its

companion peak at 1470 cm^{-1} has been assigned to polymeric sp^2 carbon phases in the grain boundaries [26]. Finally, a broad shoulder at 1560 cm^{-1} arises due to scattering by some crystallite graphite that increases with boron doping levels [22]. Thus, the Raman spectrum of BDD is indicative of a heavy-doped nanocrystalline microstructure that is uniform across the film.

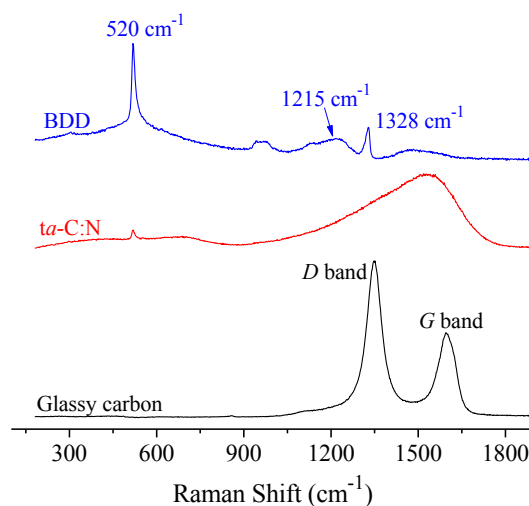


Figure 5.7. Visible Raman spectra of boron-doped diamond (blue curve), glassy carbon (black curve), and ta-C:N_{30} (red curve) thin-film electrode.

The Raman spectrum for GC displays two distinct broad peaks between 1200 and 1700 cm^{-1} , as shown in Figure 5.7. These two peaks are characteristic of amorphous graphitic carbons [27]. The peak *ca.* 1340 is called disorder-induced or D band [28] is due to a disorder-allowed A_{1g} breathing mode of sp^2 carbon atoms in six-membered rings. Another peak *ca.* 1580 cm^{-1} is known as graphitic or simply G band, and it arises due to optical phonon mode with E_{2g} symmetry linked with an in-plane C-C stretching of sp^2 -bonded carbon atoms in rings and chains [29].

ta-C:N_{30} electrode shows a broad asymmetric peak centered *ca.* 1530 cm^{-1} . The Raman spectrum is dominated by modes of graphitic lattice, D, and G bands because sp^2 carbon has a 50 to 230x higher scattering coefficient as compared to sp^3 carbon (9×10^{-7} for diamond, and 500 x

$10^{-7} \text{ cm}^{-1}/\text{sr}$ for graphite) [30,31]. Thus, the excitation of π state is more pronounced in the Raman spectra.

To learn about the effect of nitrogen incorporation in $ta\text{-C:N}_x$ films, Raman spectra were compared for $ta\text{-C:N}_x$ as shown in Figure 5.7. The peak becomes more asymmetric with increasing nitrogen content as the scattering intensity *ca.* 1350 cm^{-1} increases. This trend is indicative of an increasing fraction of sp^2 -bonded carbon in the films. The increase in asymmetry and broadening is accompanied with a slight shift in the center of G band towards lower wavenumbers. Table 5.4 compares the G band center, full width half maximum (FWHM), and intensity of D band (I_D)/intensity of G band (I_G) for the $ta\text{-C:N}$ films. While the G band shifts to lower wavenumbers accompanied with a decrease in FWHM, the ratio of intensity of D and G band increases as the nitrogen content in the film increases. More importantly, the characteristic feature of these spectra is the increase in the I_D/I_G and a decrease in the FWHM of D band. Figure 5.8 shows increase in the I_D/I_G ratio from 0.31 (for $ta\text{-C:N}_0$) to 0.56 ($ta\text{-C:N}_{10}$), 1.42 ($ta\text{-C:N}_{30}$), and 1.39 ($ta\text{-C:N}_0$).

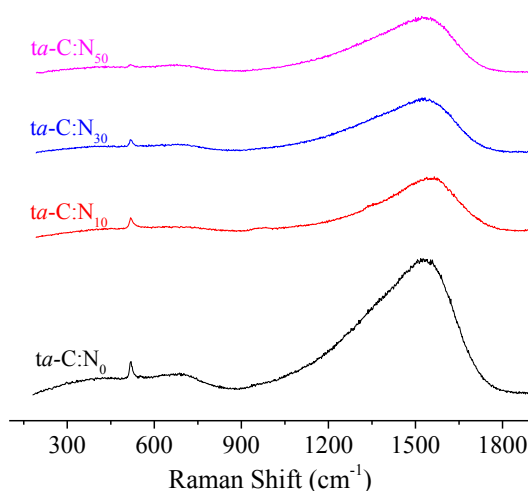


Figure 5.8. Visible Raman spectra of $ta\text{-C:N}_x$ thin-film electrodes grown in the presence of different levels of nitrogen flow rate, $ta\text{-C:N}_0$ (black curve), $ta\text{-C:N}_{10}$ (red curve), $ta\text{-C:N}_{30}$ (blue curve), and $ta\text{-C:N}_{50}$ (pink curve).

Table 5.4. Summary of visible Raman data for $ta\text{-C:N}_x$ thin-films electrodes deposited in the presence of 0, 10, 30 and 50 sccm nitrogen. The G band peak center, FWHM, and I_D/I_G ratios were compared.

| Sample | G band center (cm ⁻¹) | FWHM (cm ⁻¹) | I_D/I_G |
|----------------------|-----------------------------------|--------------------------|-------------|
| $ta\text{-C:N}_0$ | 1560.78 ± 0.41 | 283.54 ± 1.49 | 0.31 ± 0.01 |
| $ta\text{-C:N}_{10}$ | 1554.30 ± 0.41 | 270.80 ± 2.16 | 0.56 ± 0.02 |
| $ta\text{-C:N}_{30}$ | 1550.60 ± 1.09 | 237.25 ± 2.94 | 1.42 ± 0.03 |
| $ta\text{-C:N}_{50}$ | 1550.18 ± 0.35 | 237.08 ± 2.12 | 1.39 ± 0.01 |

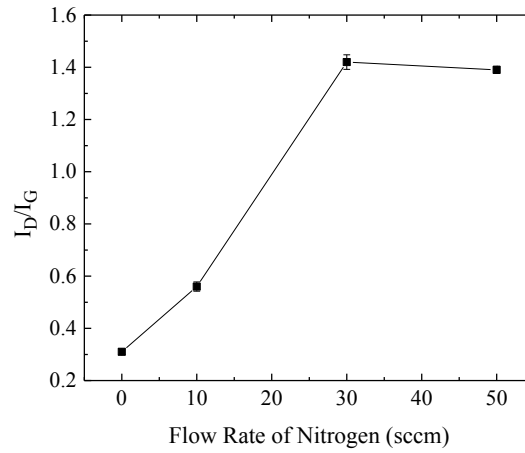


Figure 5.9. Plot of intensity of D band (I_D)/intensity of G band (I_G) calculated from visible Raman spectra of $ta\text{-C:N}_x$ thin-film as a function of different levels of nitrogen flow rate during growth.

5.3.3 Electron Energy Loss Spectroscopy (EELS)

The carbon K-edge spectra were collected at 20 spots for $ta\text{-C:N}_x$ films. The spectra are shown in Figure 5.10A for $ta\text{-C:N}_0$ (black curve), $ta\text{-C:N}_{10}$ (red curve), $ta\text{-C:N}_{30}$ (blue curve), and $ta\text{-C:N}_{50}$ (pink curve). The spectra exhibit mixed characteristics of π^* and σ^* excitations. The area between 280 and 285 eV is reflective of sp^2 -bonded carbon, while the area between 285 to 291.2 eV is characteristic of sp^3 -bonded carbon [17]. A ratio of area under π/σ region is an estimate of

sp^2/sp^3 content in the film. Corresponding values of sp^2/sp^3 carbon content are shown in Figure 5.10B. The fraction of sp^2 carbon increases with the nitrogen content.

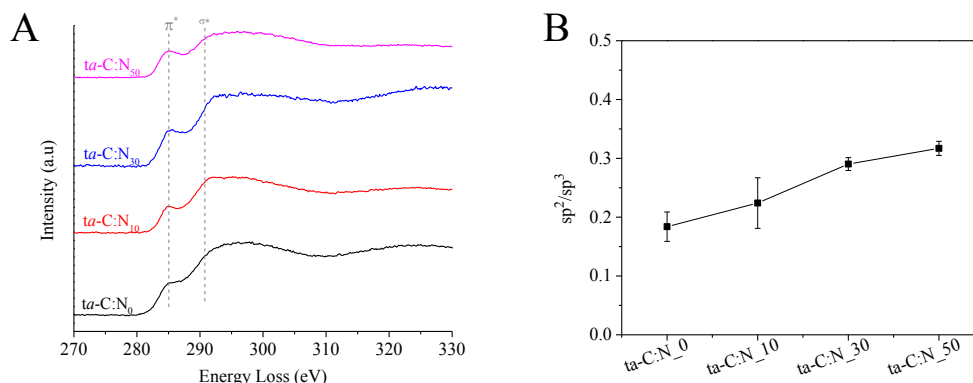


Figure 5.10. Electron energy loss spectra (EELS) at the C-K edge for $ta-C:N_0$ (black curve), $ta-C:N_{10}$ (red curve), $ta-C:N_{30}$ (blue curve), and $ta-C:N_{50}$ (pink curve). (B) Corresponding sp^2/sp^3 ratio calculated from peak area under π^* and σ^* excitations as a function of $ta-C:N_x$ films deposited with 0, 10, 30 and 50 sccm nitrogen. The error bars represent standard deviation for 12 measurements.

5.3.4 High-Resolution Transmission Electron Microscopy (HR-TEM)

HR-TEM was used to obtain insights into the morphological features of the films, specifically the location and ordering of sp^2 and sp^3 carbon domains. Representative HR-TEM images are shown in Figure 5.11 for $ta-C:N_0$, $ta-C:N_{10}$, $ta-C:N_{30}$, and $ta-C:N_{50}$ films. An interlayer spacing of 0.354 nm corresponds to sp^2 carbon, and 0.20 nm corresponds to sp^3 carbon. Contiguous paths with wavy lattice fringes can be seen. The images show randomly oriented, disordered carbon domains. The curled structures indicated by arrows represent interlayer spacing of around 0.36 nm and 0.20 nm corresponding to graphitic and sp^3 carbon, respectively. While the images mostly depict heterogeneous microstructure throughout the film, some clusters of ordered domains (1-4 nm long) that are arranged in stacks were observed as demarked by red color rectangular frames. No pattern was observed in the distribution of ordered domains. The blue color rectangular

frames indicate regions where interlayer spacing was close to that of graphite. Overall, the films are amorphous in nature with irregular interplanar spacing between neighboring atoms and ripple-like structures throughout the film.

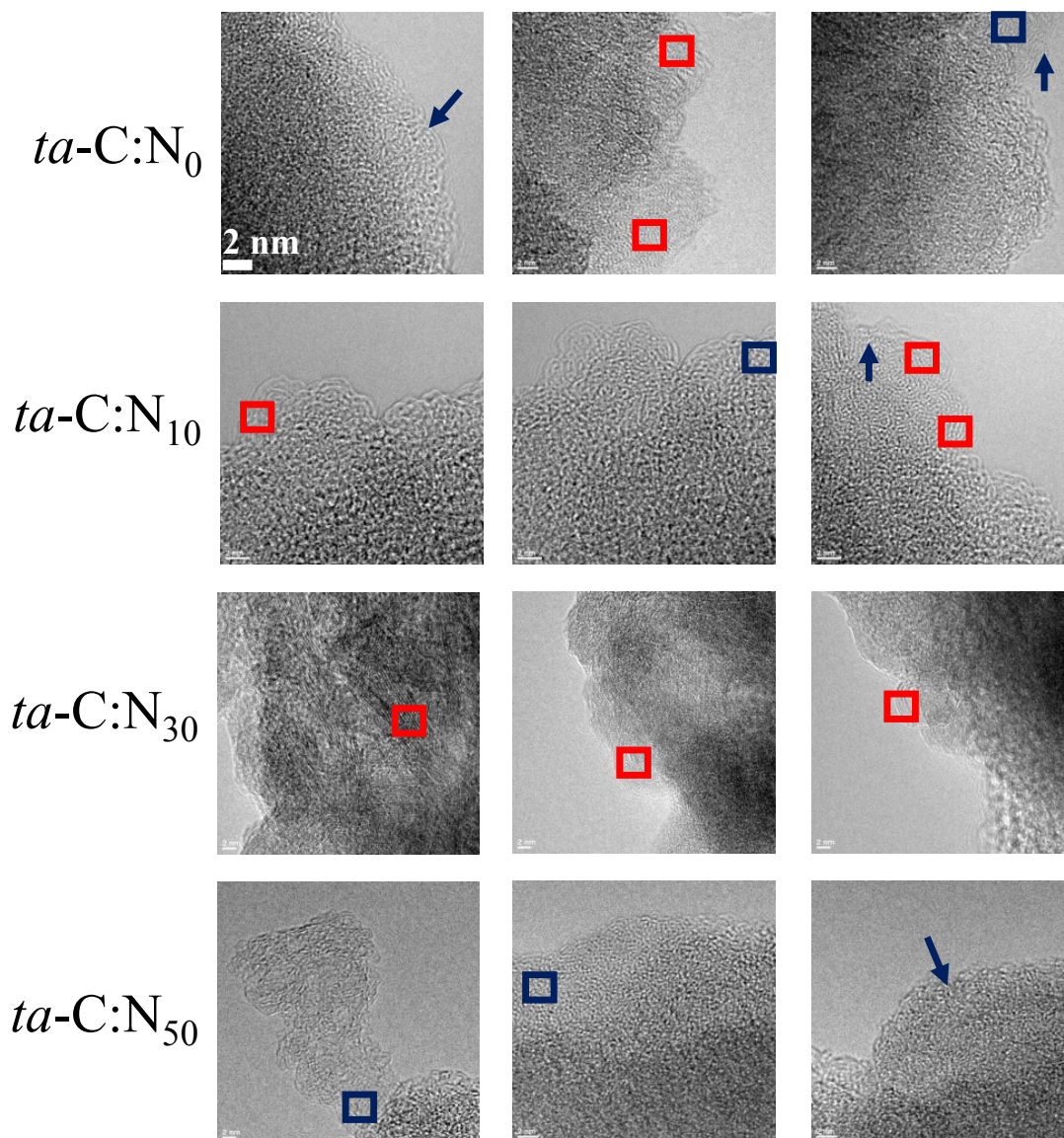


Figure 5.11. Representative HR-TEM images of different regions of $ta\text{-C:N}_0$, $ta\text{-C:N}_{10}$, $ta\text{-C:N}_{30}$, and $ta\text{-C:N}_{50}$ films. The red and blue colored rectangular frames represent domains with interlayer spacing close graphite and diamond, respectively. The arrows indicate rippled-like microstructure.

5.3.5 Cyclic Voltammetry

Figure 5.12 shows comparison of background voltammetric current for BDD, *ta*-C:N₀, *ta*-C:N₁₀, *ta*-C:N₃₀, *ta*-C:N₅₀ and GC electrodes in [HMIM][PF₆] recorded at 0.1 Vs⁻¹. A current density of 80 μAcm^{-2} was used to choose the electrochemical potential window. The BDD, *ta*-C:N₀, *ta*-C:N₁₀, *ta*-C:N₃₀, *ta*-C:N₅₀, and GC electrodes give a potential window of 6, 4.5, 4.5, 4.0, 3.5, and 3.0 V vs. Ag QRE, respectively, in [HMIM][PF₆]. A 2 V potential window was chosen to further investigate the capacitive processes.

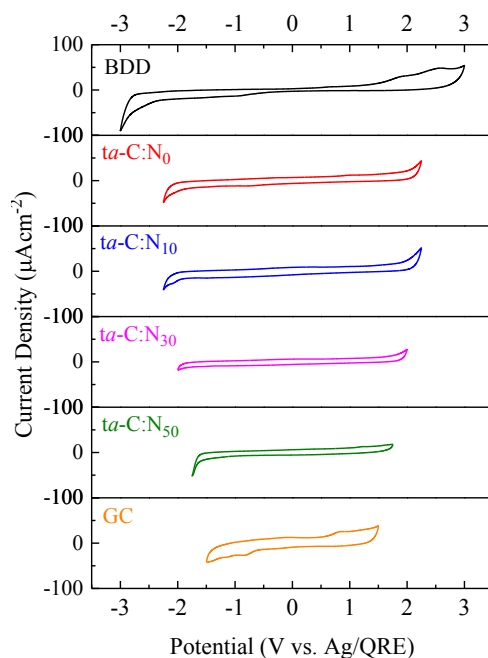


Figure 5.12. Cyclic voltammetric *j*-*E* curves for BDD (black curve), *ta*-C:N₀ (red curve), *ta*-C:N₁₀ (blue curve), *ta*-C:N₃₀ (pink curve), *ta*-C:N₅₀ (green curve), and glassy carbon (yellow curve) electrodes in [HMIM][PF₆]. The corresponding potential windows for BDD, *ta*-C:N₀, *ta*-C:N₁₀, *ta*-C:N₃₀, *ta*-C:N₅₀, and GC are 6, 4.5, 4.5, 4.0, 3.5, and 3.0 V vs. Ag QRE, respectively. Scan rate = 0.1 Vs⁻¹.

Figure 5.13 compares the scan rate-dependent voltammetric currents for *ta*-C:N₀, *ta*-C:N₁₀, *ta*-C:N₃₀, *ta*-C:N₅₀ in [HMIM][PF₆]. The current density increases linearly ($R^2 > 0.998$) with scan

rate (0.01 to 0.5 Vs^{-1}). The capacitive current of $ta\text{-C:N}_x$ electrodes increase with the nitrogen content in the film. The background current density recorded at 0.1 Vs^{-1} increases from 1.55 μAcm^{-2} for $ta\text{-C:N}_0$ to 1.87, 2.13 and 2.61 for $ta\text{-C:N}_{10}$, $ta\text{-C:N}_{30}$, and $ta\text{-C:N}_{50}$, respectively. A slope of unity establishes a pure capacitive current. The capacitance calculated from background voltammetric current density vs. scan rate increases from 12.84 to 14.85, 16.63, and 20.55 for $ta\text{-C:N}_0$, $ta\text{-C:N}_{10}$, $ta\text{-C:N}_{30}$ and $ta\text{-C:N}_{50}$, respectively.

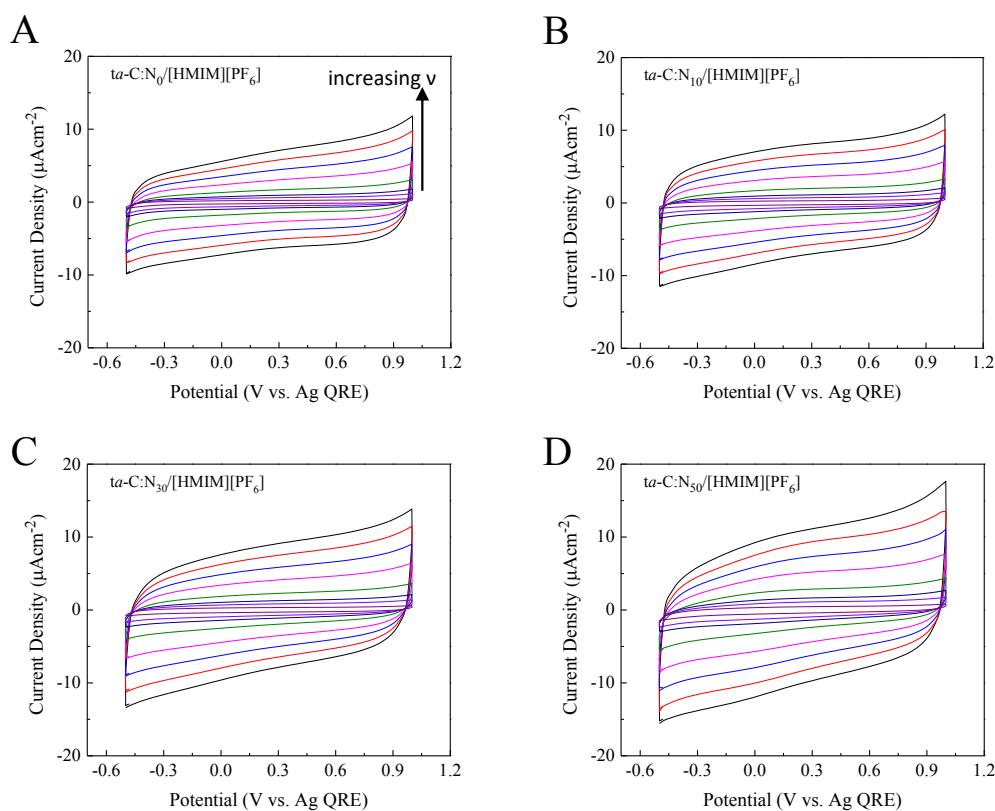


Figure 5.13. Cyclic voltammetric j - E curves for (A) $ta\text{-C:N}_0$ (B) $ta\text{-C:N}_{10}$ (C) $ta\text{-C:N}_{30}$ and (D) $ta\text{-C:N}_{50}$ thin-film electrodes in $[\text{HMIM}][\text{PF}_6]$ as a function of scan rate (0.01 to 0.5 Vs^{-1}). The scale of y-axis (current density) is kept constant for comparison purposes.

Figure 5.14 shows current density at 0.2 V vs. scan rate plots on the log scale to find out if the current densities follow trends for a pure capacitive process. A slope of unity is indicative of a

pure capacitive charging and discharging of the interface. These plots demonstrate an excellent linear relationship with a slope of 0.81 to 0.86 with $R^2 > 0.999$.

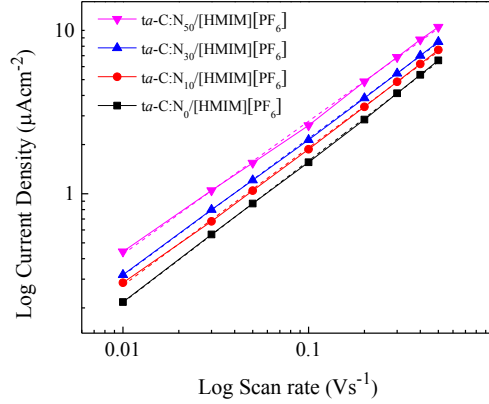


Figure 5.14. Log-log plot of current density, j , at 0 V vs. scan rate, v , in [HMIM][PF₆].

5.3.6 Electrochemical Impedance Spectroscopy

The admittance data were modeled using the equivalent electrical circuit shown in Figure 5.1. The impedance was analyzed in the complex admittance plane as it is known to be more sensitive to the capacitive processes. The following equation was used to calculate capacitance (Q) of a constant phase element (CPE) from the admittance, $Y_0 = 1/Z^{-1}$:

$$Y_{R_s-(C_{hf})(CPE)}(\omega) = j\omega C + \frac{1}{R_s + Z_0 \cdot \omega^{-\alpha} \cdot \cos\left(\frac{\alpha\pi}{2}\right) - jZ_0 \cdot \omega^{-\alpha} \cdot \sin\left(\frac{\alpha\pi}{2}\right)} \quad (ii)$$

where R_s represents the uncompensated ohmic resistance of bulk electrolyte connected in series with a parallel-connected high-frequency capacitor (C_{hf}) and a constant phase element (CPE), representing a non-ideal capacitor with Z_0 being equivalent to Q_0^{-1} and $0 < \alpha < 1$ denotes the CPE exponent. The α parameter relates the homogeneity of CPE with $\alpha = 1$ for a pure capacitor.

The impedance data were validated using Kramers-Kronig test [19]. Figure 5.15 shows a depressed semi-circle with deviation at frequencies > 21 kHz, observed as a vertical spike demarked by the red circle.

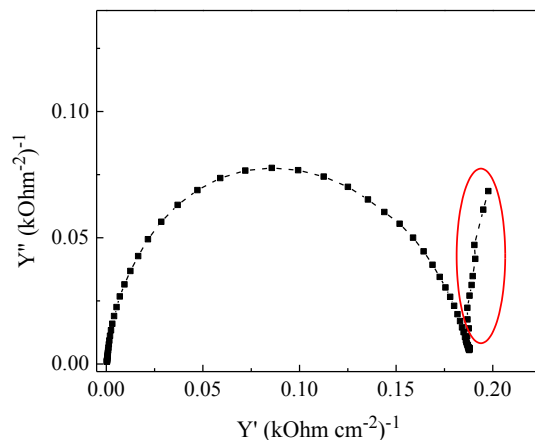


Figure 5.15. Representative admittance plot of $ta\text{-C:N}_{30}$ in $[\text{HMIM}][\text{PF}_6]$ at 0.1 V vs. Ag QRE. The black dash line represents fit to the equivalent circuit. The red circle demarks the impedance data in high frequency range (> 21 kHz) that corresponds to C_{hf} element.

Figure 5.16 shows capacitance-potential trends for $ta\text{-C:N}_0$, $ta\text{-C:N}_{10}$, $ta\text{-C:N}_{30}$ and $ta\text{-C:N}_{50}$ in $[\text{HMIM}][\text{PF}_6]$. The capacitance for $ta\text{-C:N}_0$ varies from 7.65 to 9.75 μFcm^{-2} . It changes from 10.56 to 11.00 μFcm^{-2} for $ta\text{-C:N}_{10}$, 12.30 to 14.06 μFcm^{-2} for $ta\text{-C:N}_{30}$, and 11.55 to 12.94 μFcm^{-2} for $ta\text{-C:N}_{50}$ electrodes.

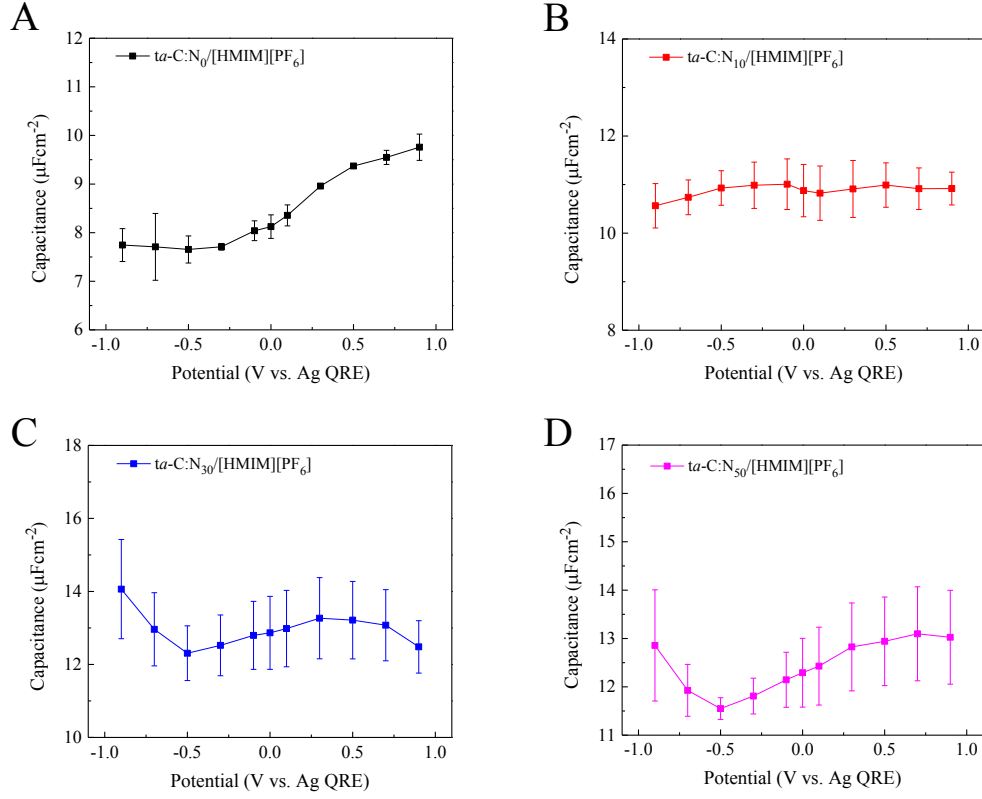


Figure 5.16. Capacitance-potential (C-E) profiles for (A) *ta*-C:N₀ (B) *ta*-C:N₁₀ (C) *ta*-C:N₃₀ and (D) *ta*-C:N₅₀ thin-film electrodes in [HMIM][PF₆]. The C-E profiles were generated using the impedance data in the full frequency (0.1 to 10⁵ Hz) spectra. Mean values of capacitance taken from three independent sets of experiments were plotted. The error bars represent standard deviation for n = 3.

Lastly, the impedance data were used to extract information on time constants of the electrochemical system [32–34]. Roling and co-workers [33] have suggested Cole-Cole analyses, which use the capacitance term and τ as the fitting parameters. The data are fit in the complex capacitance plane using the empirical equation.

$$\hat{C}(f) = \frac{C_{EDL}}{1 + (j \cdot 2\pi f \tau_{EDL})^\alpha}$$

$$= C_{EDL} \left[\frac{1 + (2\pi f \tau_{EDL})^\alpha \cos \frac{\pi\alpha}{2}}{1 + 2(2\pi f \tau_{EDL})^\alpha \cos \frac{\pi\alpha}{2} + (2\pi f \tau_{EDL})^{2\alpha}} - j \cdot \frac{1 + (2\pi f \tau_{EDL})^\alpha \sin \frac{\pi\alpha}{2}}{1 + 2(2\pi f \tau_{EDL})^\alpha \cos \frac{\pi\alpha}{2} + (2\pi f \tau_{EDL})^{2\alpha}} \right] \quad (\text{iii})$$

where C_{EDL} (μFcm^{-2}) is a capacitive term for the electrical double layer, τ_{EDL} is time constant or double layer formation time ($\tau_{EDL} = R_s.C_{EDL}$) in seconds, f represents frequency (Hz). α represents how ideal the capacitive process is (*e.g.* $\alpha = 1$ gives an ideal perfect semicircle in the admittance plot). When more than one capacitive process takes place at the interface, Cole terms are added in parallel in the complex plane (*i.e.* two Cole terms means two capacitive processes occur, and two C_{EDL} and τ_{EDL} are used as fitting parameters. Figure 5.17 shows capacitance-potential trends for the two deconvoluted processes: C_{EDL} (potential-dependent ‘fast’ process) and C_{bulk} (viscosity-dependent ‘slow’ process). These correlations have been established by Roling and co-workers [33].

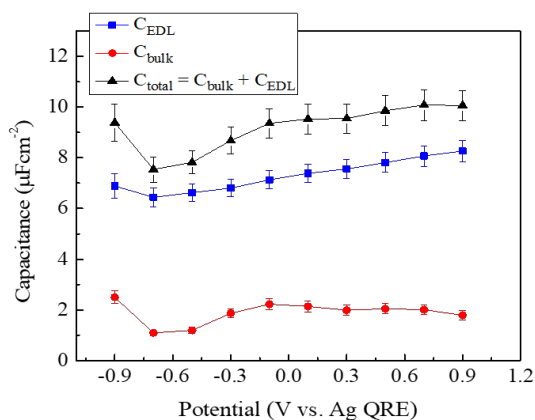


Figure 5.17. Capacitance vs. potential profile for *ta*-C:N₃₀ electrode in [HMIM][PF₆] at 0.1 V vs. Ag QRE. The total capacitance (\blacktriangle) term was deconvoluted into two capacitive processes C_{EDL} (\blacksquare) and C_{bulk} (\bullet) using Cole terms in the complex plane impedance analyses.

5.4 Discussion

In this chapter, we have sought to systemically investigate the correlation between the physical, chemical, and electronic properties of *ta*-C:N_x electrodes with different nitrogen content and their electrochemical behavior in RTILs. Our data demonstrate how the nitrogen content of *ta*-C:N_x films affects the electrode microstructure (sp^2/sp^3) and chemistry (bulk as well as surface).

To elucidate the effect of local chemical bonding, we employed XPS to obtain sp^2/sp^3 ratio in the near-surface region, and Raman and EELS in the bulk. The physicochemical properties of $ta-C:N$ electrodes manifestly affect the electrochemical potential windows, voltammetric currents, and potential-dependent capacitance in a model RTIL, [HMIM][PF₆].

$ta-C:N_x$ thin films that were grown in the presence of different volumetric flow rates (0, 10, 30, and 50 sccm) of nitrogen were used for the study. Increasing the flow rate led to greater incorporation of nitrogen in the films. XPS is a key technique that can be used to study chemical bonds between different carbon atoms. It can be used to obtain valuable information about the carbon films (a) elemental purity of the material over first 10-100 nanometer from the surface into the bulk of the material, (b) information on phase (diamond vs. graphite based on different work functions) using the deconvoluted components of the C1s peak [35], (c) identification of atoms such as oxygen, nitrogen or hydrogen, other than C, which may impact the chemistry and are bonded to carbon through single, double or triple bond. We used XPS to investigate the nature of carbon hybridization (sp^2/sp^3) at the surface as well as to quantify the heteroatoms (oxygen and nitrogen) bonded to the carbon atoms [36–40]. The data revealed that the nitrogen levels at the surface increase from 1% for films grown without nitrogen flow (i.e., at 0 sccm) to 8% for the ones grown at a nitrogen flow rate of 50 sccm. The $ta-C:N_x$ films were characterized by an oxygen-rich sp^2 bonded layer. The sp^2 carbon content increases from 55.4 % (no nitrogen) to 70 % ($ta-C:N_{50}$).

Raman spectra revealed an increase in disorder as more nitrogen gets incorporated in the $ta-C:N_x$ films. A broad asymmetric peak was observed centered around 1530 cm^{-1} , which becomes more asymmetric with increasing nitrogen incorporation in the film. Furthermore, Raman spectra exhibit a decrease in the FWHM of G band with increasing nitrogen content in the films. A significant increase in the intensity of D band relative to the G band indicates a significant

restructuring of the carbon matrix that led to an increase in the disordered sp^2 carbon phase due to nitrogen incorporation.

The EELS spectra reveal an increase in sp^2/sp^3 carbon from 0.18 for no nitrogen to 0.35 for $ta-C:N_{50}$ film. EELS has been a standalone technique to quantify the sp^2/sp^3 content [41–46] in amorphous carbon films. It generates a signature spectrum for π^* and σ^* excitation states. The area under the π^* and σ^* energy window give sp^2/sp^3 . This technique is based on the assumption that the nature of hybridization (sp^2 or sp^3 -bonding) of carbon atom in $ta-C:N$ is same as that in graphite and diamond. Based on measured spectra from these “standard” materials, a relative concentration of sp^2/sp^3 can be calculated. However, it should be noted that the p orbital in sp^2 hybrid can have some s character [47], which can affect the estimation of sp^2/sp^3 ratio. Furthermore, the high-resolution EELS spectra of $ta-C:N$ films exhibit some additional resonance near the π^* excitation peak, implying that the π bonding could be different in $ta-C:N$ than in graphite [38,48]. However, the reason for this difference is still unclear. Therefore, although EELS presents a powerful tool to study carbon materials, it is not without its limitations.

We note that the ratio of sp^2/sp^3 carbon varies in a wide range depending on the technique used. XPS data give 1.56 to 3.39 for sp^2/sp^3 carbon on the surface. Raman data reveal I_D/I_G ratio varying 0.31 to 1.39 for no nitrogen to $ta-C:N_{50}$. EELS spectra provide sp^2/sp^3 ratio from 0.18 to 0.35 for no nitrogen and $ta-C:N_{50}$, respectively. We found higher sp^2 carbon on the surface while the bulk has higher fraction of sp^3 carbon. $ta-C:N$ films are known to have fractional sp^3 carbon content in the range of 40 to 60 %, depending on the level of nitrogen incorporated in the film [17,49]. It should be noted that the sp^2/sp^3 is an estimate, and the true value can depend on contributions from heteroatom (nitrogen in this case), which can affect the sp^2/sp^3 ratio significantly as C-N and N-N modes are also present in the probed spectral regions. However,

Raman and EELS spectra were interpreted without discriminating the contributions from heterocyclic microstructures of C-N and N-N modes.

HRTEM images show sp^2 - and sp^3 -carbon rich phases separated by ripple-like microstructures for which the interlayer spacing lies between that of graphite and diamond. Some short-range ordered domains were observed. Overall, films are amorphous with some minimal crystalline domains on the nanometer scale. HRTEM images show significant structural heterogeneity at the sub-nanometer scale. We did not find any correlation or pattern between the relative strength of these features/domains and the nitrogen content. HRTEM images taken from spots far apart (on the scale of μm) on the films further capture the structural heterogeneity of the films.

Cyclic voltammograms are featureless, indicative of clean electrodes and dry RTILs. The current density vs. potential (j-E) response has a characteristic rectangular shape principally ascribed to the non-faradaic charging currents. The background current increases linearly with the scan rate at all potentials. The capacitance of $ta-C:N_0$ is $\sim 8.7 \mu F cm^{-2}$ (closer to that of BDD in [HMIM][PF₆]), whereas $ta-C:N_{50}$ shows $\sim 12.24 \mu F cm^{-2}$ in the same room temperature ionic liquid ([HMIM][PF₆] – closer to that of GC).

The trends of potential-dependent capacitance reveal that the $ta-C:N_0$ film exhibits characteristics of a p-type semi-conductor, as demonstrated by a sharp increase in the capacitance at positive potentials above 0 V vs. Ag QRE. As more nitrogen gets incorporated in the films, the density of states (DOS) increases, and C-E trends indicate semi-metallic behavior. Further increase in the nitrogen content does not change the shape of C-E trends. However, the magnitude of capacitance increases owing to more DOS available to support the charge carriers. It can be

concluded that 30 sccm film possesses enough electrical conductivity ideal to be used as an electrode. Higher levels of nitrogen do not necessarily increase the double-layer capacitance. The C-E trends for $ta\text{-C:N}_{30}$ and $ta\text{-C:N}_{50}$ films are qualitatively similar to those shown by BDD in the same RTIL, [HMIM][PF₆]. The minimum capacitance lies close to -0.5 V vs. Ag QRE as it is on BDD films.

5.5 Conclusions

Nitrogen-incorporated $ta\text{-C}$ amorphous films were grown using cathodic arc vacuum deposition method. Our results show that the nitrogen doping can be achieved even with low levels of nitrogen concentration in the gas mixture during the deposition of films. We have shown that XPS, Visible-Raman, EELS, can be used to derive structural information about the localized bonding in $ta\text{-C:N}_x$ films. The nitrogen gets incorporated both on the surface as well as in the bulk. We learned that the differences in physical, chemical, and electrochemical properties are a consequence of different atomic ordering (graphite vs. diamond) and the content of nitrogen incorporated in the film.

- (i) We identified a sp^2 carbon-rich layer on the surface using XPS. The surface reacts readily with the atmosphere and water to form carbon-oxygen functional groups to satisfy the dangling exposed sites on the surface.
- (ii) Raman data suggest that nitrogen incorporation increases the disorder sp^2 carbon phase in the film. The flow rate of nitrogen more than 30 sccm does not result in a further increase in the disordered sp^2 carbon content.

- (iii) EELS data reveal an overall higher fraction of sp^3 carbon in the bulk. However, the sp^2/sp^3 fraction in the bulk increases with the nitrogen content. EELS data also indicate strong heterogeneity of films. With an increased understanding of complexity of π^* and σ^* excitation states, it is being assumed that the local chemical hybridization might be more complex than sp^2 and sp^3 .
- (iv) The C-E trends suggest that the ta-C film with no nitrogen shows strong p-type characteristics. However, as nitrogen content increases, it compensates for the p-type properties in the disordered carbon matrix.
- (v) ta-C:N_x films are found to be structurally complex and exhibit substantial heterogeneity as evidenced by graphitic and diamond phases distributed widely throughout the film.

This study highlights the significant role of dopant (nitrogen) incorporation on physical, chemical, electrical and electrochemical properties. The dopant (nitrogen) amount plays a significant role in the growth of amorphous taC:N_x films and it can be used to tune the sp^2 to sp^3 carbon content. XPS, EELS and Raman analyses provide an estimate of sp^2/sp^3 hybridization in ta-C:N_x films. We provided insights on bulk and surface configurations along with some guidance regarding the differences in sp^2/sp^3 estimates using different characterization techniques. The physical, chemical and electrochemical properties need to be monitored at both the macroscopic and nanoscale. Further in-depth analysis is required to build a comprehensive understanding of the electrochemical heterogeneity and their origins in these novel electrode materials.

REFERENCES

REFERENCES

- [1] P. Chen, M.A. Fryling, R.L. McCreery, Electron Transfer Kinetics at Modified Carbon Surfaces, 67 (1995) 3115–3122.
- [2] R.J. Rice, N.M. Pontikos, R.L. McCreery, Quantitative Correlations of Heterogeneous Electron-Transfer Kinetics with Surface Properties of Glassy Carbon Electrodes, J. Am. Chem. Soc. 112 (1990) 4617–4622. doi:10.1021/ja00168a001.
- [3] J. Robertson, Diamond-like amorphous carbon, Mater. Sci. Eng. R Reports. 37 (2002) 129–281. doi:10.1016/S0927-796X(02)00005-0.
- [4] L. Radovic, Surface Chemistry of Activated Carbon Materials, (2010). doi:10.1201/9780824746681.pt3.
- [5] X. Yang, L. Haubold, G. Devivo, G.M. Swain, Electroanalytical performance of nitrogen-containing tetrahedral amorphous carbon thin-film electrodes, Anal. Chem. 84 (2012) 6240–6248. doi:10.1021/ac301124r.
- [6] R. Jarošová, P.M. De Sousa Bezerra, C. Munson, G.M. Swain, Assessment of heterogeneous electron-transfer rate constants for soluble redox analytes at tetrahedral amorphous carbon, boron-doped diamond, and glassy carbon electrodes, Phys. Status Solidi Appl. Mater. Sci. 213 (2016) 2087–2098. doi:10.1002/pssa.201600339.
- [7] H.J. Scheibe, B. Schultrich, D. Drescher, Laser-induced vacuum arc (Laser Arc) and its application for deposition of hard amorphous carbon films, Surf. Coatings Technol. 74–75 (1995) 813–818. doi:10.1016/0257-8972(95)08280-8.
- [8] H.J. Scheibe, B. Schultrich, DLC film deposition by Laser-Arc and study of properties, Thin Solid Films. 246 (1994) 92–102. doi:10.1016/0040-6090(94)90737-4.
- [9] D. Drescher, J. Koskinen, H.J. Scheibe, A. Mensch, A model for particle growth in arc deposited amorphous carbon films, Diam. Relat. Mater. 7 (1998) 1375–1380. doi:10.1016/S0925-9635(98)00211-8.
- [10] B.L.M. Veerasamy, V. S., Yuan J., Amaratunga A. A. J., Milne W. I., Gilkes K. W. R., Weiler M., Nitrogen Doping of Highly Tetrahedral Amorphous Carbon, Phys. Rev. B. 48 (1993) 954–959.
- [11] L. Valentini, J.M. Kenny, R.M. Montereali, L. Lozzi, S. Santucci, Influence of nitrogen and temperature on the plasma deposition of fluorinated amorphous carbon films, J. Vac. Sci. Technol. A Vacuum, Surfaces, Film. 20 (2002) 1210–1215. doi:10.1116/1.1479359.

- [12] W.I. Rodil, S.E., Morrison, N. A., Robertson, J., Milne, Nitrogen incorporation into tetrahedral hydrogenated amorphous carbon, *Phys. Status Solidi Appl. Res.* 174 (1999) 25–37. doi:10.1002/(SICI)1521-396X(199907)174:1<25::AID-PSSA25>3.0.CO;2-3.
- [13] J. Ristein, Diamond surfaces: Familiar and amazing, *Appl. Phys. A Mater. Sci. Process.* 82 (2006) 377–384. doi:10.1007/s00339-005-3363-5.
- [14] A. Tafel, M. Wu, E. Spiecker, P. Hommelhoff, J. Ristein, Fabrication and structural characterization of diamond-coated tungsten tips, (2019). <http://arxiv.org/abs/1902.01369>.
- [15] N. Wächter, C. Munson, R. Jarošová, I. Berkun, T. Hogan, R.C. Rocha-Filho, G.M. Swain, Structure, Electronic Properties, and Electrochemical Behavior of a Boron-Doped Diamond/Quartz Optically Transparent Electrode, *ACS Appl. Mater. Interfaces.* (2016) A-M. doi:10.1021/acsami.6b02467.
- [16] N. Elgrishi, K.J. Rountree, B.D. McCarthy, E.S. Rountree, T.T. Eisenhart, J.L. Dempsey, A Practical Beginner's Guide to Cyclic Voltammetry, *J. Chem. Educ.* 95 (2018) 197–206. doi:10.1021/acs.jchemed.7b00361.
- [17] S. Waidmann, M. Knupfer, J. Fink, B. Kleinsorge, J. Robertson, Electronic structure studies of undoped and nitrogen-doped tetrahedral amorphous carbon using high-resolution electron energy-loss spectroscopy, *J. Appl. Phys.* 89 (2001) 3783–3792. doi:10.1063/1.1350999.
- [18] M.C. Granger, M. Witek, J. Xu, J. Wang, M. Hupert, A. Hanks, M.D. Koppang, J.E. Butler, G. Lucazeau, M. Mermoux, J.W. Strojek, G.M. Swain, Standard electrochemical behavior of high-quality, boron-doped polycrystalline diamond thin-film electrodes, *Anal. Chem.* 72 (2000) 3793–3804. doi:10.1021/ac0000675.
- [19] J. Wallauer, M. Balabajew, B. Roling, Impedance Spectroscopy on Electrode | Ionic Liquid Interfaces, 2017. doi:10.1002/9783527682706.ch11.
- [20] A. Proctor, P.M.A. Sherwood, X-ray photoelectron spectroscopic studies of carbon fibre surfaces. I. carbon fibre spectra and the effects of heat treatment, *J. Electron Spectros. Relat. Phenomena.* 27 (1982) 39–56. doi:10.1016/0368-2048(82)85051-2.
- [21] J. Moulder, J.E., Chastain, Handbook of x-ray photoelectron spectroscopy: A reference book of standard spectra for identification and interpretation of XPS data, 1992. doi:10.1016/S0015-0282(16)36193-3.
- [22] P.W. May, W.J. Ludlow, M. Hannaway, P.J. Heard, J.A. Smith, K.N. Rosser, Raman and conductivity studies of boron-doped microcrystalline diamond, faceted nanocrystalline diamond and cauliflower diamond films, *Diam. Relat. Mater.* 17 (2008) 105–117. doi:10.1016/j.diamond.2007.11.005.
- [23] P. Szirmai, T. Pichler, O.A. Williams, S. Mandal, C. Bäuerle, F. Simon, A detailed analysis

- of the Raman spectra in superconducting boron doped nanocrystalline diamond, *Phys. Status Solidi Basic Res.* 249 (2012) 2656–2659. doi:10.1002/pssb.201200461.
- [24] E. Bourgeois, E. Bustarret, P. Achatz, F. Omnès, X. Blase, Impurity dimers in superconducting B-doped diamond: Experiment and first-principles calculations, *Phys. Rev. B - Condens. Matter Mater. Phys.* 74 (2006) 1–8. doi:10.1103/PhysRevB.74.094509.
 - [25] J.P. Goss, P.R. Briddon, Theory of boron aggregates in diamond: First-principles calculations, *Phys. Rev. B - Condens. Matter Mater. Phys.* 73 (2006) 1–8. doi:10.1103/PhysRevB.73.085204.
 - [26] A.C. Ferrari, J. Robertson, Origin of the 1150 cm⁻¹ Raman mode in nanocrystalline diamond, *Phys. Rev. B - Condens. Matter Mater. Phys.* 63 (2001) 2–5. doi:10.1103/PhysRevB.63.121405.
 - [27] F. Tuinstra, J.L. Koenig, Raman Spectrum of Graphite, *J. Chem. Phys.* 53 (1970) 1126–1130. doi:10.1063/1.1674108.
 - [28] M.A. Pimenta, G. Dresselhaus, M.S. Dresselhaus, L.G. Cançado, A. Jorio, R. Saito, Studying disorder in graphite-based systems by Raman spectroscopy, *Phys. Chem. Chem. Phys.* 9 (2007) 1276–1291. doi:10.1039/b613962k.
 - [29] K. Jurkiewicz, M. Pawlyta, D. Zygadło, D. Chrobak, S. Duber, R. Wrzalik, A. Ratuszna, A. Burian, Evolution of glassy carbon under heat treatment: Correlation structure–mechanical properties, *J. Mater. Sci.* 53 (2018) 3509–3523. doi:10.1007/s10853-017-1753-7.
 - [30] S.A. Wada, N. Solin, Raman efficiency measurements of graphite, *J. Non. Cryst. Solids.* 105B (1981) 353–356. doi:10.1016/0378-4363(81)90274-6.
 - [31] F. Breu, S. Guggenbichler, J. Wollmann, “Diamond-like” 3-fold coordinated amorphous carbon, *J. Non. Cryst. Solids.* 36 (1980) 543–548. <http://medcontent.metapress.com/index/A65RM03P4874243N.pdf>.
 - [32] M. Drüscler, B. Huber, B. Roling, On capacitive processes at the interface between 1-Ethyl-3-methylimidazolium tris(pentafluoroethyl)trifluorophosphate and Au(111), *J. Phys. Chem. C.* 115 (2011) 6802–6808. doi:10.1021/jp200395j.
 - [33] B. Roling, M. Drüscler, B. Huber, Slow and fast capacitive process taking place at the ionic liquid/electrode interface, *Faraday Discuss.* 154 (2012) 303–311. doi:10.1039/c1fd00088h.
 - [34] T. Jansch, J. Wallauer, B. Roling, Influence of Electrode Roughness on Double Layer Formation in Ionic Liquids, *J. Phys. Chem. C.* 119 (2015) 4620–4626. doi:10.1021/jp512617j.
 - [35] J.I.B. Wilson, J.S. Walton, G. Beamson, Analysis of chemical vapour deposited diamond

- films by X-ray photoelectron spectroscopy, *J. Electron Spectros. Relat. Phenomena.* 121 (2001) 183–201. doi:10.1016/S0368-2048(01)00334-6.
- [36] J. Díaz, G. Paolicelli, S. Ferrer, F. Comin, Separation of sp³ and sp² components in the C1s photoemission spectra of amorphous carbon films, *Phys. Rev. B.* 54 (1996) 8064–8069. doi:10.1103/PhysRevB.54.8064.
- [37] P. Mérel, M. Tabbal, M. Chaker, S. Moisa, J. Margot, Direct evaluation of the sp³ content in diamond-like-carbon films by XPS, *Appl. Surf. Sci.* 136 (1998) 105–110. doi:10.1016/S0169-4332(98)00319-5.
- [38] R. Lossy, D.L. Pappas, R.A. Roy, J.P. Doyle, J.J. Cuomo, J. Bruley, Properties of amorphous diamond films prepared by a filtered cathodic arc, *J. Appl. Phys.* 77 (1995) 4750–4756. doi:10.1063/1.359411.
- [39] P.K. Chu, L. Li, Characterization of amorphous and nanocrystalline carbon films, *Mater. Chem. Phys.* 96 (2006) 253–277. doi:10.1016/j.matchemphys.2005.07.048.
- [40] J. Ferrari, A.C., Robertson, Raman spectroscopy of amorphous, nanostructured, diamond-like carbon, and nanodiamond, *Green Planet Blues Crit. Perspect. Glob. Environ. Polit.* 362 (2004) 2477–2512. doi:10.4324/9780429493744.
- [41] Z.L. Zhang, R. Brydson, Z. Aslam, S. Reddy, A. Brown, A. Westwood, B. Rand, Investigating the structure of non-graphitising carbons using electron energy loss spectroscopy in the transmission electron microscope, *Carbon N. Y.* 49 (2011) 5049–5063. doi:10.1016/j.carbon.2011.07.023.
- [42] B.E. Mironov, H.M. Freeman, A.P. Brown, F.S. Hage, A.J. Scott, A.V.K. Westwood, J.P. Da Costa, P. Weisbecker, R.M.D. Brydson, Electron irradiation of nuclear graphite studied by transmission electron microscopy and electron energy loss spectroscopy, *Carbon N. Y.* 83 (2015) 106–117. doi:10.1016/j.carbon.2014.11.019.
- [43] A.L. Hamon, J. Verbeeck, D. Schryvers, J. Benedikt, R.M.C.M.V.D. Sanden, ELNES study of carbon K-edge spectra of plasma deposited carbon films, *J. Mater. Chem.* 14 (2004) 2030–2035. doi:10.1039/b406468m.
- [44] B. Jouffrey, P. Schattschneider, C. Hébert, The magic angle: A solved mystery, *Ultramicroscopy.* 102 (2004) 61–66. doi:10.1016/j.ultramic.2004.08.006.
- [45] R. Arenal, M. Kociak, N.J. Zaluzec, High-angular-resolution electron energy loss spectroscopy of hexagonal boron nitride, *Appl. Phys. Lett.* 90 (2007). doi:10.1063/1.2740185.
- [46] K. Suenaga, M. Koshino, Atom-by-atom spectroscopy at graphene edge, *Nature.* 468 (2010) 1088–1090. doi:10.1038/nature09664.

- [47] C. Gao, Y.Y. Wang, A.L. Ritter, J.R. Dennison, Nature of Carbon-Carbon Bonding in Evaporated and Ion-Sputtered (Diamondlike) Amorphous Carbon from (e, 2e) Spectroscopy, *Phys. Rev. Lett.* 62 (1989) 945–948.
- [48] D.L. Pappas, K.L. Saenger, J.J. Cuomo, R.W. Dreyfus, Characterization of laser vaporization plasmas generated for the deposition of diamond-like carbon, *J. Appl. Phys.* 72 (1992) 3966–3970. doi:10.1063/1.352249.
- [49] C. Arena, B. Kleinsorge, J. Robertson, W.I. Milne, M.E. Welland, Electronic properties of tetrahedral amorphous carbon investigated by scanning tunneling microscopy, *J. Appl. Phys.* 85 (1999) 1609. doi:10.1063/1.369293.

Chapter 6

Conclusions and Future Outlook

The principal focus of the research presented in this dissertation was to learn how room temperature ionic liquids (RTILs) form interfaces with nanostructured carbon electrodes and how these interfacial organizations depend on electrode microstructure (sp^2 , sp^3 , and sp^2/sp^3), surface chemistry (H- vs. O-termination), and RTIL size. The interfacial organization was studied as capacitance-potential (C-E) trends obtained using cyclic voltammetry, broadband electrochemical impedance spectroscopy (EIS), and single-frequency impedance measurements.

In chapter 3, we validated that the bell-shape C-E trend as predicted by the theoretical models can be obtained on a metal electrode (Au) while boron-doped diamond (BDD) electrode exhibits an opposite, U-shape trend in the same RTIL, under similar experimental conditions and using similar measurement method. Further research is needed to understand the differences in how RTIL ions interact with metal vs. carbon electrodes. Unlike metals with an infinite density of states (DOS), carbon electrodes have doping level-dependent DOS to support the charge carriers at the surface. So, the contribution of the electronic phase within the solid electrode must be understood. It would be reasonable to expect that some potential drop takes place within the bulk phase of the BDD electrode. The C-E trends predicted by theoretical models cannot be directly compared with the experimental trends due to the inherent limitations of models such as the exclusion of complex interactions between RTIL ions and electrode surfaces. Many research groups have reported on strong interactions between tightly bound RTIL ions and electrode surfaces observed using in-situ AFM and STM measurements [1]. Some electrode surfaces, such

as single crystal Au, is known to undergo surface reconstruction and development of mirror charges at the interface [2] [3]. These disparities between theoretical and experimental C-E trends are an inspiration to understand the supposedly complex behavior of RTIL media in response to electrode polarization.

The arrangement of ions in the innermost layer next to the BDD electrode make major contribution to the overall capacitance. This shows that the C-E trends are dictated not only by the electrode material but also by the inherent properties of RTILs (size of ions, viscosity, dielectric constants, concentrations, etc.). To better understand the interactions between the electrode surface and RTIL ions, we employed chemically modified BDD electrodes with varying type (H *vs.* O) and surface coverage of functional groups. The results from this investigation are described in Chapter 4. We learnt that any subtle change in the surface chemistry significantly affects the potential-dependent capacitance, which increases with the surface wettability. Since there is no dielectric spacer (*i.e.* solvent molecules) to separate the interactions between the BDD surface and RTIL ions, short-range interactions dominate, hydrophobic counterpart of RTIL ions ‘wets’ the hydrophobic hydrogen-terminated BDD more, and thus leads to an increase in capacitance.

In Chapter 5, we focused on the effect of nitrogen content in tetrahedral amorphous ($ta\text{-C:N}_x$) films on physical, chemical and electrochemical behavior of electrodes in RTILs. We showed that the chemical hybridization (sp^2/sp^3) can be controllably tuned by varying the nitrogen content during the film deposition. The capacitance increases with the sp^2 carbon content in the films due to more nitrogen incorporation. $ta\text{-C:N}_x$ films are known to be electrically and electrochemically heterogeneous. Some sp^2 carbon-rich domains are expected to be present on the surface separated by sp^3 carbon-rich domains. The electrochemical behavior of these domains can be understood using spatial mapping techniques.

Fundamental understanding of these interfaces is critical. To fully understand the system, the time scales and lateral length scale of organizations of ions need to be investigated as this knowledge can be manifested in applications of RTILs in transient electrochemical techniques. *In-situ* or operando techniques can be used in tandem to correlate the structural aspects (the lateral length scale of the organization of ions) and the dynamic aspects (*i.e.*, the time constants) of these interfacial processes are two important missing pieces of the puzzle to better understand the interfacial phenomena in RTILs.